Abstract

MCLAWHORN, STEVEN LEE. Secondary Electron Emission Yields from Fast Fluorine Ions on Copper and Amorphous Solid Water Foils. (Under the direction of Dr. Larry H. Toburen.)

The biological outcomes from charged particle radiation exposure are heavily influenced by the spatial patterns of energy distributed within the biological system. Monte Carlo track structure codes can be used to model these patterns of energy deposition event-by-event provided that cross sections for interactions are accurately known. Interaction cross sections in condensed phase materials cannot be directly measured and are therefore often estimated from theory. In order to test the accuracy of Monte Carlo electron transport codes double-differential electron emission yields $\gamma(\varepsilon,\theta)$, differential in energy ε and emission angle θ, have been measured from condensed phase targets following impact by fast Fluorine ions. Secondary electron emission spectra were measured using electron time-of-flight energy analysis for emission angles from 15° to 155° with respect to the incident beam. Copper foil targets were studied independently and later used as a substrate for amorphous solid water targets which best simulate the liquid water medium commonly used in track structure codes. The electron emission yields collected will serve in the future as a benchmark for comparison with simulated yields from Monte Carlo transport codes to assess the modeling accuracy of the production and transport of secondary electrons in condensed phase materials.

This work is supported by the National Institutes of Health, National Cancer Institute Grant No. 2R01CA093351.

Secondary Electron Emission Yields from Fast Fluorine Ions on Copper and Amorphous Solid Water Foils

A Dissertation

Presented to

the faculty of the Department of Physics

East Carolina University

In Partial Fulfillment

of the Requirements for the Degree

Doctor of Philosophy in Biomedical Physics

Steven L. McLawhorn

April, 2011

Secondary Electron Emission Yields from Fast Fluorine Ions on Copper and Amorphous Solid Water Foils

by

Steven L. McLawhorn

APPROVED BY:

DIRECTOR OF DISSERTATION:

_____
Larry H. Toburen

COMMITTEE MEMBER:_____
Jefferson L. Shinpaugh

COMMITTEE MEMBER:_____
Michael Dingfelder

COMMITTEE MEMBER:_____
Edson L. B. Justiniano

COMMITTEE MEMBER:_____
David W. Pravica

CHAIRMAN OF THE DEPARTMENT OF PHYSICS:

_____
John C. Sutherland

DEAN OF THE GRADUATE SCHOOL:

_____
Paul Gemperline

Acknowledgements

I would like to sincerely thank my dissertation advisor Dr. Larry Toburen. Dr. Toburen has had a tremendous influence on my life since I was an undergraduate physics student and has truly taught me almost everything I know. He has been tireless in his efforts to instruct and guide me in this work, and I cannot thank him enough for all he has done.

I would also like to express my sincere gratitude to the other members of my dissertation committee: Dr. Jeff Shinpaugh, Dr. Michael Dingfelder, Dr. Edson Justiniano, and Dr. David Pravica. This work has only been possible with their continued insight and support. Over the years I have come to view this group as my extended family, and I will never forget all that they have done for me.

Finally, I would like to thank my friends at the James R. Macdonald Laboratory at Kansas State University. I am forever indebted to Dr. Kevin Carnes, Bob Krause, and Mike Wells for their assistance while these experiments were being performed.

Table of Contents

List of Figures

Chapter 1: Introduction

The biological effectiveness resulting from charged particle radiation is heavily influenced by the spatial distribution of secondary electrons produced by interactions of the incident particles passing through the biological medium. This is because damage that occurs at the sub-cellular level, such as single and double strand DNA breaks, is directly related to the spatial distribution of the ionization events produced by the primary charged particle and resulting secondary electrons. Therefore, to predict the outcome of a biological system exposed to charged particle radiation detailed information on the spatial patterns of ionization events is needed.

Monte Carlo track structure models are increasingly being used in radiation physics and biology to model the production and transport of charged particles in condensed phase biological materials. These codes track the production and transport of primary particles and resulting secondary electrons from their initial energies down to sub-excitation energies [1-12]. Monte Carlo models require elastic and inelastic interaction cross-sections to determine the path of charged particles as they travel through the transport medium. Since it is extremely difficult and in many cases infeasible to directly measure these interaction cross-sections in condensed phase materials [13], Monte Carlo track structure models rely on theoretically determined interaction cross-sections for ions and electrons in condensed phase [14-17]. Given that the cellular environment is composed primarily of water most Monte Carlo transport models use liquid water as the transport medium. Therefore interaction cross-sections for the charged particles with water are required. The theoretical models used to estimate cross sections have greater uncertainties for electrons with energies equivalent to the energies of bound

electrons, less than a few hundred electron volts. Therefore, experimental validation of these models and the interaction cross-sections upon which they rely is important to their application in radiation physics and biology. The current work provides benchmark data for assessing low energy electron transport in condensed water.

The yield of electrons ejected from condensed phase targets as a result of heavy charged particle impact can provide information on the production and transport of secondary electrons within the target material. Secondary electrons are liberated through projectile-target ionization interactions. The liberated electrons resulting from these interactions are transported through the target material through a complex series of interactions and are capable of causing further ionization events, thus liberating additional electrons as they travel through the target material. Once the liberated electrons reach the surface of the target they escape the target material if there is sufficient energy to overcome the surface potential barrier of the target. The resulting spectrum of electrons is a convolution of secondary electrons produced by primary interactions of the incident projectile and target material and electrons liberated through further interactions of the secondary electrons, and provides information on both scattering in the medium and the potentials present at the surface [18].

In this study low energy electron transport is studied by measuring double-differential electron emission yields $\gamma(\varepsilon,\theta)$, differential with respect energy ε and emission angle θ, of the emitted electrons. These measurements describe the resulting spectrum of electrons on a per incident ion basis. This information is useful in understanding material properties and charged particle interactions within condensed phase materials as described above. These studies seek to provide data sets of double-

differential electron emission yields $\gamma(\varepsilon,\theta)$ for direct comparison with Monte Carlo charged particle tracks structure codes used in radiation physics and biology.

For that purpose we have measured absolute double-differential electron emission yields $\gamma(\varepsilon,\theta)$ as a result of heavy ion impact on condensed phase targets. While earlier work has focused on measurements of double-differential electron emission yields from protons [19], this work focuses on 19 MeV Fluorine ions (1 MeV/u). These measurements were performed using electron time-of-flight (TOF) energy analysis to focus on accurately measuring the low-energy portion of the emission spectra, the region where the majority of the secondary electrons are expected to be emitted and where the theoretically determined interaction cross sections are expected to be the least accurate. The Fluorine ions have sufficient velocity such that their interactions can be accurately described within the framework of the first Born approximation [15,20]. Measurements were made from 15°-155° to measure the full spectrum of electron emission. The targets studied consisted of thin, 1-μm thick, sputter cleaned Cu foils and amorphous solid water condensed and frozen on Cu foil substrates. These foils were sufficiently thin for the impinging ions to lose only a small fraction of their incident energy [21-24]. Conversely, the foils are thick relatively to the mean free path of the secondary electrons. Electrons with energies as high as 1 keV have a mean free path of approximately 3nm or less [25]. The thickness of frozen water foils used in this study were on the order of 35 to 40 nm thus ensuring that the observed spectra were representative of the water foil and not the copper substrate.

The studies of electron emission from the Cu foil in this work were designed to serve two purposes. The first was to provide a data set of electron emission spectra from

a pure homogeneous target from which comparisons with theoretical and computational models could be made. The second was to characterize the substrate used for the amorphous solid water studies and aid in the data analysis for this target. By freezing water under appropriate conditions a layer of amorphous solid water can be deposited that does not exhibit the crystal structure of ice but rather a random orientation of molecules more representative of water in liquid form. Incident projectiles of 19 MeV (1 MeV/u) fluorine ions were used in this work and comparisons with 6 MeV proton data were made to assess differences in electron emission yields as a function of incident projectile.

The remainder of this thesis is presented as follows. In chapter 2 background material on total, single-, and double-differential electron emission yields as a result of heavy ion impact on solids is presented. A general description of the secondary electron production and transport process is presented. This general description is intended to provide the reader with the background necessary to understand the presented work. A general review of the literature is presented. This overview is not intended to be a complete literature review but is intended to again provide the information needed to understand and interpret the data presented in this work.

In chapter 3 the materials and methods used in this work are presented. A description of the accelerator system and experimental beam-line at the J.R. MacDonald Atomic Physics Laboratory (JRM) at Kansas State University (KSU) is given in section 3.2. While many of the techniques, systems components, and preliminary data presented in this work were developed in the Atomic Physics Laboratory at East Carolina University (ECU), a description of the system at ECU is not provided since the data

presented in this work was not collected there. For a detailed description of the system at ECU the reader should refer to the work of R.A. McLawhorn [19]. The experimental target chamber, target, detectors, and data acquisition system are described in section 3.3. These are presented in detail since their operation is crucial to measuring the emission of low-energy electrons. Finally, data analysis techniques are presented in section 3.4.

In chapter 4 the results and discussion is presented for 19 MeV Fluorine ions incident on thin 1-μm Cu foils and amorphous solid water on Cu foil substrates. The 19 MeV Fluorine on Cu data is presented in section 4.2. This data is compared to 6 MeV proton data taken during the same period using the same experimental system [19]. Section 4.3 presents data from 19 MeV Fluorine ions incident on amorphous solid water condensed on Cu foil substrates as a function of amorphous solid water thickness. Double- and single-differential electron emission yields from amorphous solid water on Cu foils substrates is presented in section 4.4.Finally, in chapter 5 a summary of the work is presented along with suggestions for future research.

Chapter 2: Electron Emission from Solids Induced by Heavy Ions

2.1: Background

Studies of electron emission from condensed phase materials as a result of heavy ion impact can yield information on the properties of the target material as well as the interactions of the incident and secondary particles within the material. This information has numerous applications in materials science, physics, and radiation biology. Recent interest in these studies has been driven by an increasing need to understand the effects of heavy ion impact and its associated electron production on biological systems. Understanding these effects requires detailed knowledge of both the energy and angular distributions of secondary electrons within the biological system of interest since the secondary electrons liberated in these events and their subsequent interactions are generally credited for the majority of the biologically damaging effects of charged particle radiation.

Measurements of the internal spectra of secondary electrons in condensed phase materials are not possible. Therefore, studies have focused on measurement of the external electron emission spectra. While the external emission spectra is composed of electrons produced by interaction with the incident projectile and electrons produced by interactions with secondary electrons, much information on the material properties and individual interactions can still be obtained. Reviews of electron emission from condensed phase targets are available in the literature [26-28].

As a heavy ion passes through a condensed phase target it exerts forces on atomic electrons through electromagnetic interactions. These interactions transfer energy to atomic electrons causing excitations and ionizations along the track of the heavy charged

particle. Due to the large difference in the mass of the heavy ion and the atomic electrons the heavy ion imparts only a small fraction of its energy in a single interaction resulting in very little deviation in its trajectory. Electrons previously bound to the atoms in the target material that are liberated through ionization might have sufficient energy to cause further excitation and ionization events as they travel through the target material. These secondary electrons also interact with the atomic electrons through electromagnetic forces. However, since the interactions are between particles with the same mass, a larger range of energies can be transferred between the particles. The secondary electrons, therefore, have a more tortuous path as they travel through the target material.

The series of energy loss events will continue until the heavy ion and all secondary electrons have deposited their energy in the target material or escaped the surface of the target. To escape from the target material the particle must overcome the surface potential barrier of the target. The barrier is dependent on the target material and typically ranges from zero to several electron volts. Only particles with sufficient energy to overcome the surface barrier will escape the target. The surface conditions of the target material greatly influence the surface barrier and the resulting electron emission yield. The resulting external electron emission spectra will be composed of both secondary electrons produced by interactions with the incident projectile and electrons produced by interaction with other secondary electrons.

2.2: Electron Emission Yields

As previously mentioned, it is not possible to directly measure the internal spectrum of electrons within the target material. Experiments have therefore focused on measurement of the external emission spectra. Many of these studies have focused on

measurements of total electron emission yields, denoted by γ and defined as the total number of electrons emitted from the target per incident ion. Traditionally, measurements have been made of single-differential electron emission yields; either the yield of electrons emitted as a function of angle $\gamma(\theta)$ or the yield of electrons emitted as a function of energy $\gamma(\varepsilon)$. The most detailed information on electron emission comes from measurements of doubly-differential electron emission yields $\gamma(\varepsilon,\theta)$ which give the yield of electron emitted from the surface of the target as a function of emission energy and angle as a result of heavy ion impact.

Measurements of double differential electron emission yields, differential with respect to electron emission energy ε and angle θ, are available in the literature although the measurements are more limited than measurements of total and single-differential yields [29,30]. In many of these measurements the data is either limited in range of angular measurements or the range of the energy distribution measured. Most of the measurements of the energy distributions are made by electrostatic energy analysis [29,30]. While this method is useful for accurate measurements of electrons emitted with energies above 50 eV it can be problematic in lower energy measurements where the electric field produced by the analyzer might alter the energy measurements. Information from this low-energy range is important since it is in this range that the majority of secondary electrons are emitted as a result of the passage of heavy ions through the target material, being the major contributor to biological damage. It is also at low-energies where the material dependence is most evident and surface contaminants have the greatest effect on the electron emission spectra. Therefore, to study these material and surface properties of electron emission from condensed phase targets accurate

measurements of the low-energy portion on the emission spectra is essential. Time-of-flight energy analysis is one method to accurately measure low-energy emission spectra from condensed phase targets and there are a few studies which have measured double differential electron emission yields from condensed phase targets using time-of-flight energy analysis [13,19,20,22]. However, these studies are limited to fast proton impact and further data is needed to understand the differences for heavy ions.

While time-of-flight analysis is useful in low energy measurement the resolution of this method decreases significantly with increasing particle energy, and many spectral structures cannot be resolved by this method. To illustrate the type of information that can be obtained from measurements of doubly-differential electron emission yields and where the spectral range of this work fits in, a schematic of idealized electron emission spectra resulting from heavy ion impact taken from the work of Frischkorn *et al*. [31] are shown in Fig. 2.4. The emission spectra, plotted on a log scale, are shown as a function of electron velocity for two measurement angles θ_1 and θ_2, with $\theta_1=0°$ and $\theta_2>\theta_1$. Both emission angles show a large peak at low-energies. This result is expected since the majority of electrons ejected from the target atoms will have energies less than 20 eV and these electrons will undergo further energy degradation as they travel trough the target material before escaping the surface of the target. This region of "Secondary Electrons" is the most useful region for time-of-flight analysis. As the emission energy increases the yield of electrons emitted from the target rapidly decreases. The magnitude of the decrease is not as evident on this plot due to the log scaling of the intensity. A second peak is seen at $v_e = v_p$, where v_e and v_p are the emitted electron and incident projectile velocities, respectively. This small peak is a result of forward scattered and convoy

electrons. Material dependent peaks, such as the Auger peaks seen in both curves, can be used to identify the target material and in some cases identify target and surface contaminants that contribute to the emission spectra. Auger peaks originating from the incident heavy ion might also be seen in the emission spectra. The origin of these peaks will be evident since they will be Doppler energy shifted due to the velocity of the heavy ion. Binary encounter electrons, resulting from head on interactions with the incident particles, result in the broad peak center at $v_e = 2v_p$. These binary encounter electrons are therefore most easily seen on the θ=0° spectra.

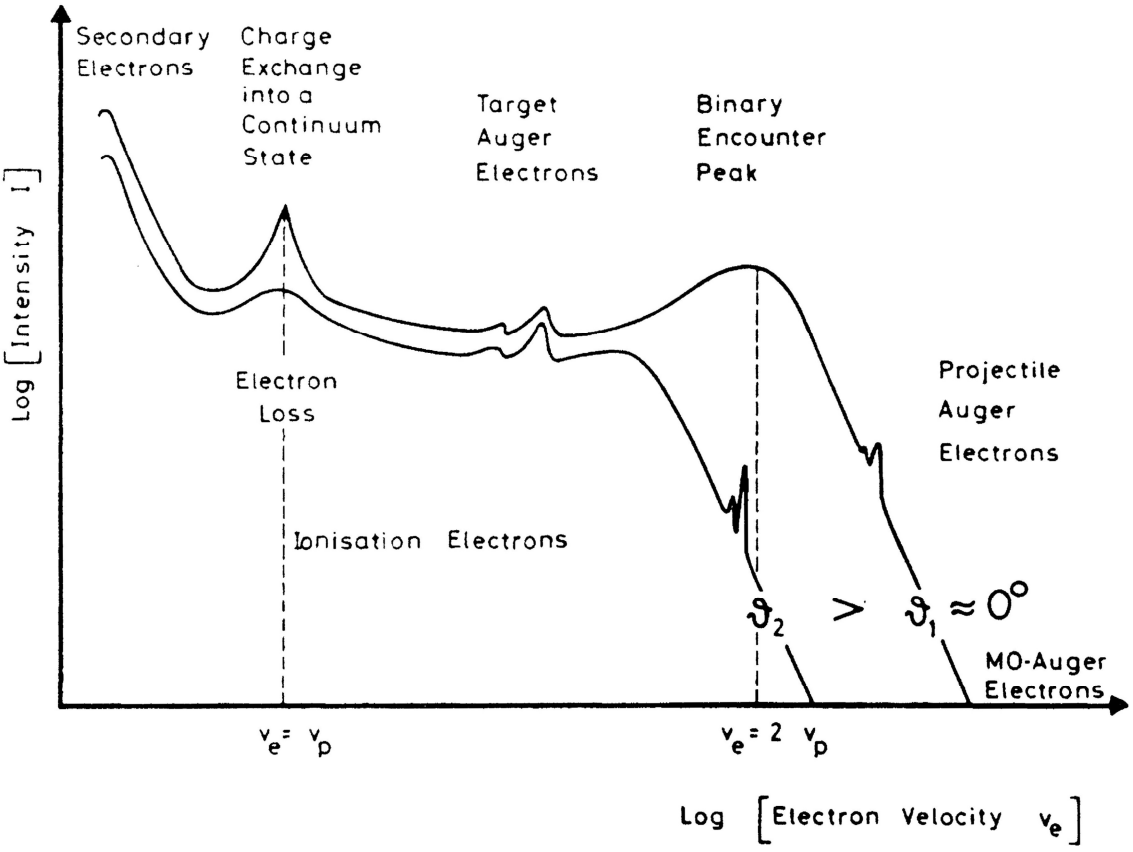

FIG. 2.1: Electron emission spectra from a condensed phase target as a result of heavy ion impact taken at two observation angles $\theta_1 = 0°$ and $\theta_2 > \theta_1$ Frischkorn et al. [31].

Surface conditions can significantly affect the electron emission spectra. Therefore samples must be atomically clean and measurements performed under ultra high vacuum (UHV) conditions, less than 10^{-8} Torr. Surface contamination is known to affect the shape of the emission spectra as well as overall yield of electrons [26-28,13,19,20,22, 32-36]. Surface contaminants most easily influence the low-energy portion of the emission spectra with changes in the emission spectra being seen with less than a monolayer of contamination [35,36]. The high-energy portion of the emission spectra is less affected by the surface barrier potential. However, surface contamination can result in characteristic peaks from the contaminants being seen in the emission spectra and as the thickness of the contamination on the target increases the emission spectra becomes more representative of the contaminant.

Examples in the literature of measurements of single differential electron emission yields as a result of heavy ion passage through condensed phase targets are more numerous than double differential electron emission yields. Although it is possible to measure $\gamma(\theta)$, the yield of electrons as a function of the emission angle, $\gamma(\varepsilon)$, the yield of electrons as a function of energy is more commonly measured. Both $\gamma(\varepsilon)$ and $\gamma(\theta)$ can be obtained from $\gamma(\varepsilon,\theta)$ by integration with respect to the appropriate variable.

Measurements of $\gamma(\varepsilon)$ show many of the same spectral features as seen in studies that measure $\gamma(\varepsilon,\theta)$. As with $\gamma(\varepsilon,\theta)$ there is a strong material dependence in the location and shape low-energy peak electron emission peak [37-42]. The location of this peak has been shown to be relatively insensitive to the incident projectile energy [34]. However, the shape and intensity of the peak increases with increasing energy [37-41]. The width of the low-energy peak increases with increasing projectile energy for heavy ion impact

[34], and as with double-differential electron emission yields, the yield of electrons quickly decreases with increasing energy [37-41]. Material and projectile dependent spectral features such as Auger peaks are also visible on the emission spectra [34,37,40]. The low-energy electron peak as well as the total yield of electrons is also heavily influenced by the surface conditions of the target in $\gamma(\varepsilon)$ studies [34]. This is the same effect seen in the double differential electron emission yields, and again reiterates the importance of target purity and UHV measurement conditions to accurately measure these emission spectra.

Total electron emission yield γ is defined as the total number of electrons emitted from the surface of a target per incident ion. The use of γ in the literature often refers to electron emission from one side of the target only; i.e. emission from the projectile entrance or exit side of the target. Other times γ might refer to electron emission from both the projectile entrance and exit side of the target. Other authors use γ_B and γ_F to designate the electron emission from the projectile entrance (backward) and exit (forward) side of the target respectively. Throughout this work γ is used to designate electron emission from both sides of the target and γ_B and γ_F represents electron emission from the entrance and exit side of the target, respectively.

Total electron emission yields are the most abundant type of electron emission studies and can be obtained from direct measurements or integration of either double- or single-differential electron emission yields with respect to the appropriate variables. The projectile energy dependence on the total yield of electrons has been studied extensively for proton impact. The total yield of electrons as a function of the projectile energy follows the same trends as the electronic stopping power for proton impact. This is shown

in Fig. 2.5 for total electron emission from Al, Cu, Ag, and Au targets taken from Hasselkamp et al [27]. The peak in the total electron emission yields occur at approximately the same projectile energy as the maximum in the stopping power.

For protons, a material dependent proportionality constant Λ, called the materials factor, can be obtained from the relation:

$$\gamma = \Lambda\left(\frac{dE}{dx}\right)_e . \tag{2.1}$$

where $(dE/dx)_e$ is the electronic stopping power of the proton in the material of interest. A plot of the ratio of the materials factor Λ to the electronic stopping power $(dE/dx)_e$ versus the incident proton energy is shown in Fig. 2.6, taken from the work of Hasselkamp et al. [27]. The ratio of the material constant to the electronic stopping power remains constant within 10% from the keV to MeV energy range [27]. This relationship remains valid as long as the energy of the incident proton remains approximately constant through the target material. For fast proton impact similar relationships are observed for γ_F and γ_B with the electronic stopping power $(dE/dX)_e$ through proportionality constants Λ_F and Λ_B, respectively [42,43].

Since γ_F and γ_B are related to the electronic stopping power through constants Λ_F and Λ_B the ratio R of γ_F to γ_B should also remain constant:

$$R = \frac{\gamma_F}{\gamma_B} = \frac{\Lambda_F \big/ (dE/dx)_e}{\Lambda_B \big/ (dE/dx)_e} = \frac{\Lambda_F}{\Lambda_B}. \tag{2.2}$$

This relationship has been found to be constant within the energy range from several keV to several MeV [44,45].

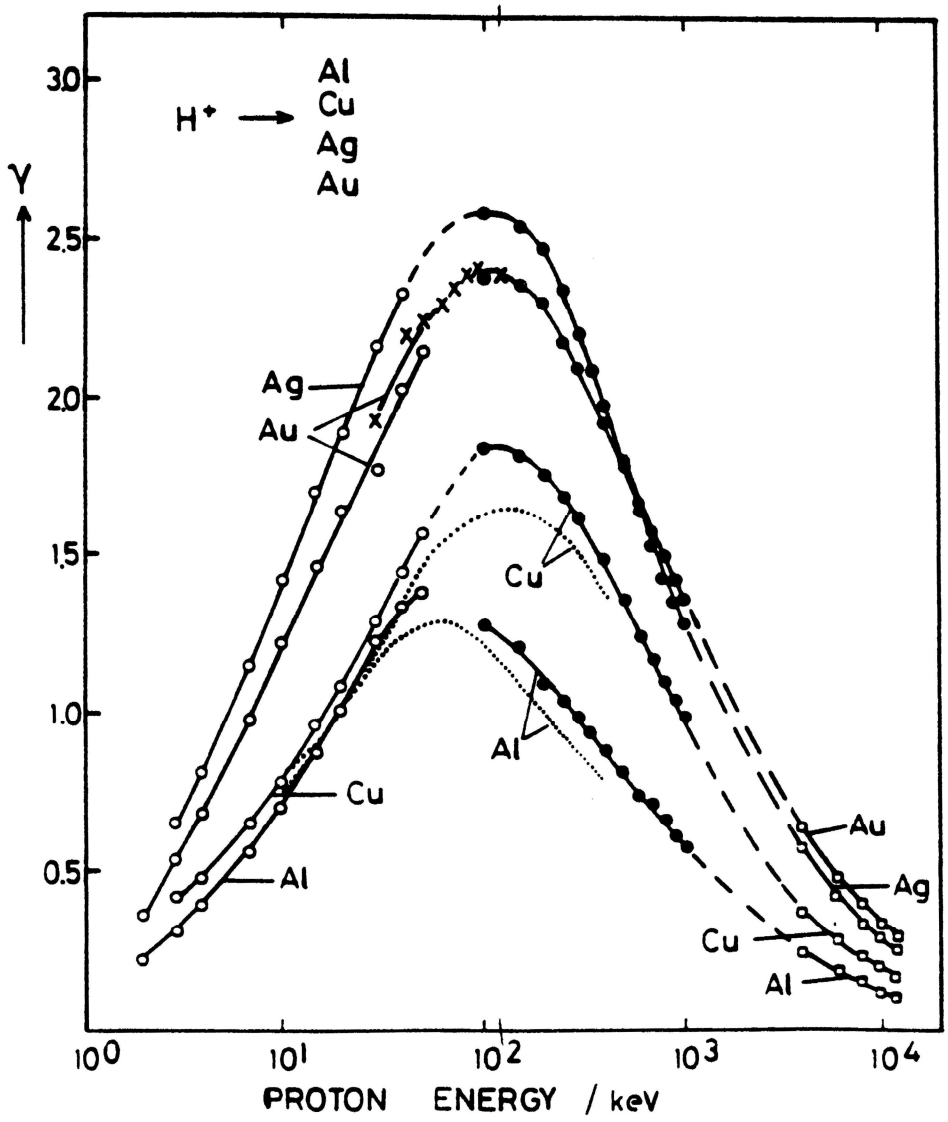

Fig. 2.2: Total electron emission yields as a function of energy for proton impact on Al, Cu, Ag, and Au targets taken from Hasselkamp et al. [27]. The peak in the yield of electrons corresponds to the peak in the stopping power of the incident particle in the target material.

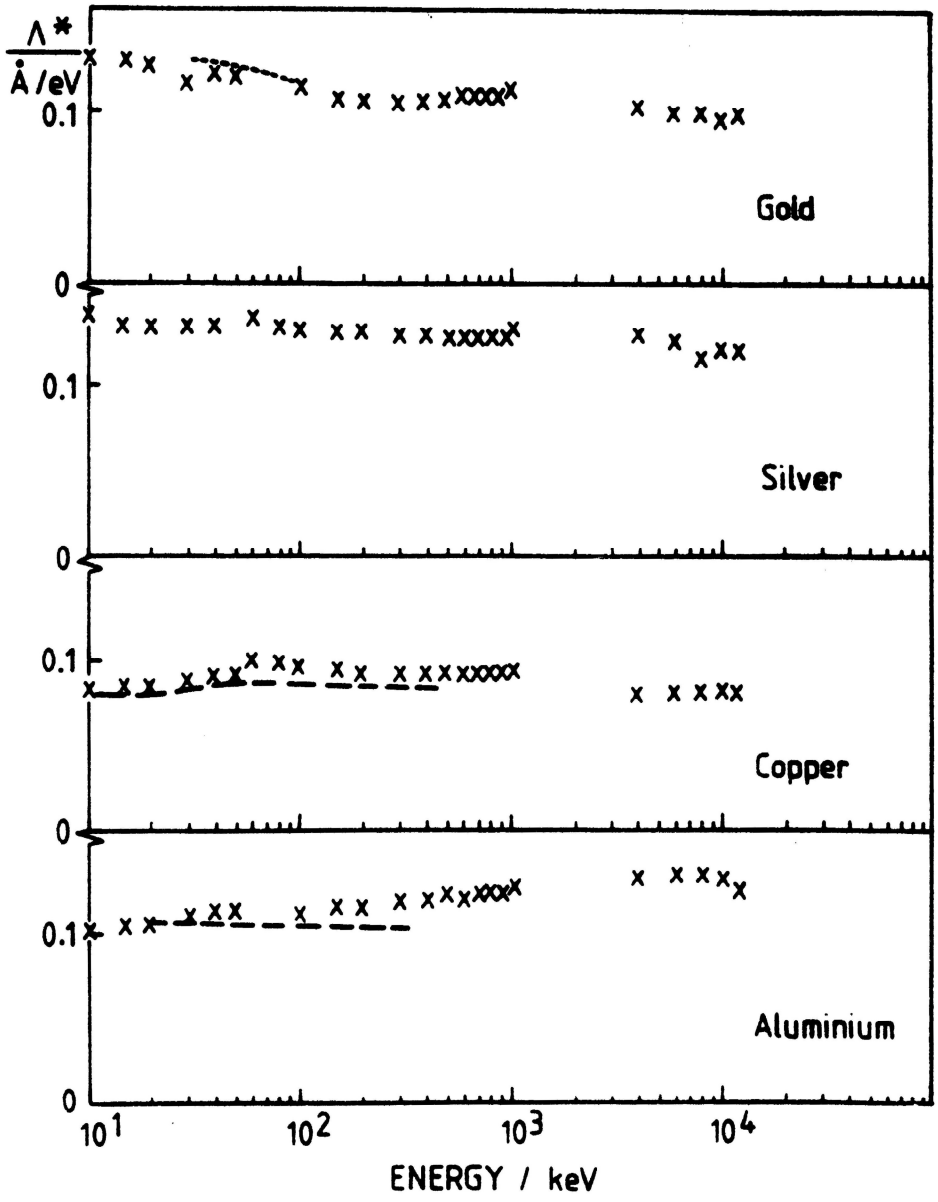

Fig. 2.3: Plot from Hasselkamp et al. [27] showing the ratio of the total electron emission yield γ to the electronic stopping power $(dE/dx)_e$ from several keV to MeV as a result of fast proton impact on Au, Ag, Cu, and Al targets.

For heavy-ion impact other than protons, the total electron emission yields do not follow the stopping power relationship given in Eq. 2.2 as closely [42, 45-49]. The yield of electrons increases with the atomic number Z of the incident particle due to an increase in the electronic stopping power $(dE/dx)_e$. However, the relationship is more complex than Eq. 2.2 and Λ increases as the Z of the incident particles increases [48,49]. Additionally, γ_F increases at a faster rate that γ_B and the ratio R increases with the atomic number Z of the particle [45,49,50]. These deviations might reflect the more complex interactions that the incident projectile undergoes as it travels through the target material. Changes in the stopping power of the incident particle as it travels through the target material might result in a difference in electron emission from the projectile entrance and exit surfaces of the target. The projectile charge state has also been observed to influence the yield of electrons [45]. The case that these deviations in R and its variables are a result of complex interactions is further advanced by the fact that these differences are less evident in experiments using fast He ions where the heavy ions are less complex and include fewer potential charge states [48,49].

Chapter 3: Experiment and Procedure

3.1: Introduction

This experiment designed to measure secondary electron production and transport was performed at the J.R. MacDonald Atomic Physics Laboratory (JRM) at Kansas State University (KSU). Many components of the experimental system including the time-of-flight (TOF) system were loaned to the East Carolina University (ECU) Department of Physics from Pacific Northwest National Laboratory (PNNL) where they were previously used for similar studies of secondary electron emission from Carbon foils and frozen gases [13,20]. Since being installed at East Carolina University the system has been used to study collisions of fast protons on condensed phase targets including amorphous solid water (ASW) [22]. In an effort to extend prior research the system was moved to JRM whose facilities could provide incident particles of higher energies and additional ion species. This allowed a more complete study of electron emission from 1μm thick copper foils by protons that provide absolute calibration of the system [22]. In addition, this provided the opportunity to measure electron emission yields, doubly differential in energy and angle, from higher energy 6 MeV protons and to explore the effects of track density from 19 MeV fluorine ions on 1 μm thick copper foils and amorphous solid water targets. Emission spectra were measured at angles ranging from 15° to 155° with respect to the incident beam by electron time-of-flight (TOF) energy analysis, and these spectra have been analyzed and converted to absolute yields based on the calibration from proton measurements.

Over the course of this work substantial improvements were made to the experimental system to increase confidence in measured spectra and to bolster the functionality of the system as a whole.

3.2: Overview of Accelerator and Associated Systems at JRM

The accelerator and associated components at JRM are shown schematically in Figure 3.1. It can be seen in the figure that there were two ion sources available at JRM. One was a cesium sputter source whose function has been described in detail by Middleton [51]. The second ion source was a diode source that produced ions from direct ionization of injected gas. Both sources had advantages for creating particular projectiles. In these experiments the diode source was used for negatively charged hydrogen ions and the sputter source was used to generate negatively charged fluorine ions. Ions produced from both sources were injected into a 60 kV acceleration region one meter in length. This acceleration region was followed by an inflection magnet that selected the desired particles by energy and momentum.

To use the TOF technique for measuring low energy electrons the beam needed to be divided into pulses with durations on the order of nanoseconds. Thus following the inflection magnet a deflector and buncher were used to pulse the resulting particle beam. The deflector employed multiple charged deflection plates that forced the beam to oscillate up and down allowing only short pulses of beam particles to pass through an exit aperture. The pulses from the deflector were on the order of 40 to 70 ns in duration and separated in time by 1.3 μs [52].

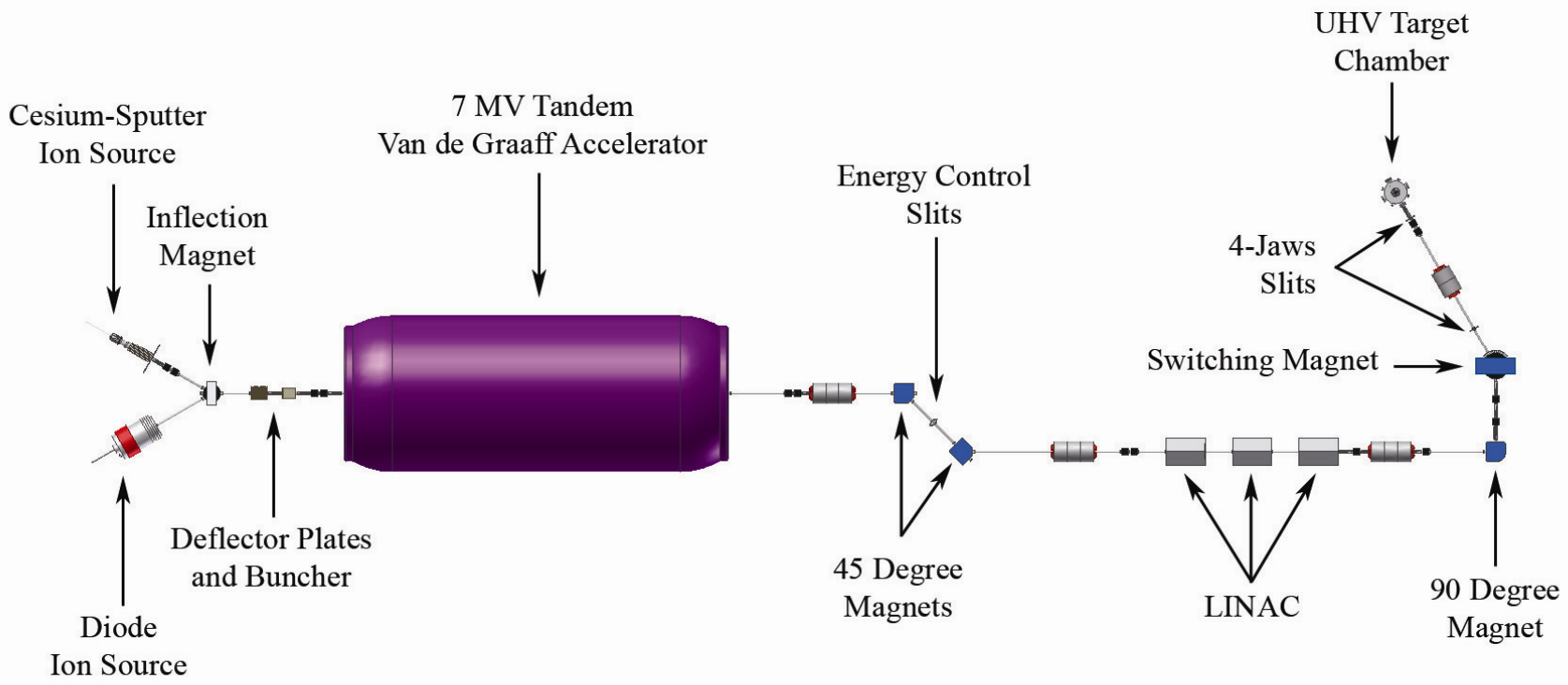

Figure 3.1. Schematic of the 7 MV Van de Graaff accelerator and associated components at Kansas State University.

The deflector alone was not capable of creating pulses of one nanosecond duration. Instead, the deflected beam pulses were compressed in length by the buncher. The buncher created a time dependent electric field along the path of the beam pulses. The potential of the generated electric field had a ramp shape along the particle path to slow the faster particles in the pulse while accelerating the slower particles. The net effect was to compress the beam pulses in length and thereby duration. Ideally the resulting beam pulses are of 1 ns duration and separated in time by 1.3 μs, although resolution diminishes variably with changing operating conditions. This parameter was monitored on a daily basis.

Following the bunching process the beam pulses were injected into the 7 MV Tandem Van de Graff accelerator [53]. In the accelerator the high energy terminal was held at a positive potential. The first stage of particle acceleration occurred as the negative ions injected from the buncher accelerated toward the positively charged terminal. Upon reaching the terminal the ions passed through a region of low density O_2 gas. The oxygen gas acted to strip electrons from the negative ions leaving a particle beam comprised of positive ions. It is at this point that the second acceleration stage occurred as the positively charged ions were repelled from the positively charged terminal and exited the accelerator with the desired energy.

Accelerated ions were then selected by mass and charge state using a pair of 45° magnets. A set of energy control slits followed the first 45° magnet to control beam energy. Following the last magnet the accelerator system contained a LINAC approximately 10 meters in length. The LINAC was not used in this experiment, and was an unavoidable feature of the facility that added extra length to the path of the incident

particles. Due to the long distance of travel along the beam tube several triplet quadrupole magnets were in place downstream of the LINAC to maintain beam focus, and a 90° magnet coupled with a switching magnet were used to direct the particle beam down the 30°-left beam tube toward the collision chamber.

The 30°-left experimental beamline was evacuated using two turbo-molecular pumps. These pumps were located at opposing ends of the beam tube, and reduced the pressure in the beam tube to 10^{-7} Torr. This pressure was sufficiently low that little change was observed in the chamber pressure when the collision chamber was open to the beam tube.

A set of 4-jaw slits were installed at both ends of the beam tube to reduce beam intensity and create a defined beam spot. Additional x-y steering magnets were placed along the final section of the beamline to assist in fine alignment of the incoming particle beam with the collimator at the entrance of the target chamber.

3.3: Experimental System

3.3.1: Target Chamber

The ultra-high vacuum (UHV) collision chamber used for these experiments is shown from the top view and side view in Figures 3.2 and 3.3 respectively. The chamber was constructed of non-magnetic stainless steel and all flanges were sealed with copper gaskets. The chamber lid was sealed using a Viton o-ring as this was found to overcome the effects of small surface defects on the sealing surfaces and improved the ultimate pressure of the chamber. Chamber vacuum was established with the use of both a turbo-molecular pump and a Titanium-sublimation pump. These pumps and seals enabled the

chamber to reach ultra-high vacuum pressures on the order of 10^{-9} to 10^{-10} Torr. Additionally, the chamber was heated to approximately 100° C for 24 hours prior to data collection in order to expel water vapor and gas contaminants from the inner surfaces.

Minimizing magnetic fields in the interaction region was necessary to accurately measure electron emissions as these fields can significantly influence the path of low-energy electrons. To attenuate stray magnetic fields in the interaction region the interior of the chamber was lined with double walled magnetic shielding made of high permeability μ-metal. Further reduction of magnetic fields was accomplished with the use of Helmholtz coils mounted above and below the chamber. The Helmholtz coils were tuned by placing a precision Gauss-meter at the target position and adjusting the coil current until a minimum was reached. The shielding alone reduced the magnetic field inside the chamber to less than 50 milligauss. The addition of the coils further reduced the magnetic field to less than 2 milligauss.

An aperture was in place at the entrance to the collision chamber to collimate the incoming beam and center it on the target area ensuring that all impinging particles shared the same trajectory. The aperture of the collimator was approximately 1 mm in diameter, and the assembly was grounded to prevent charging from impinging particles and secondary electrons.

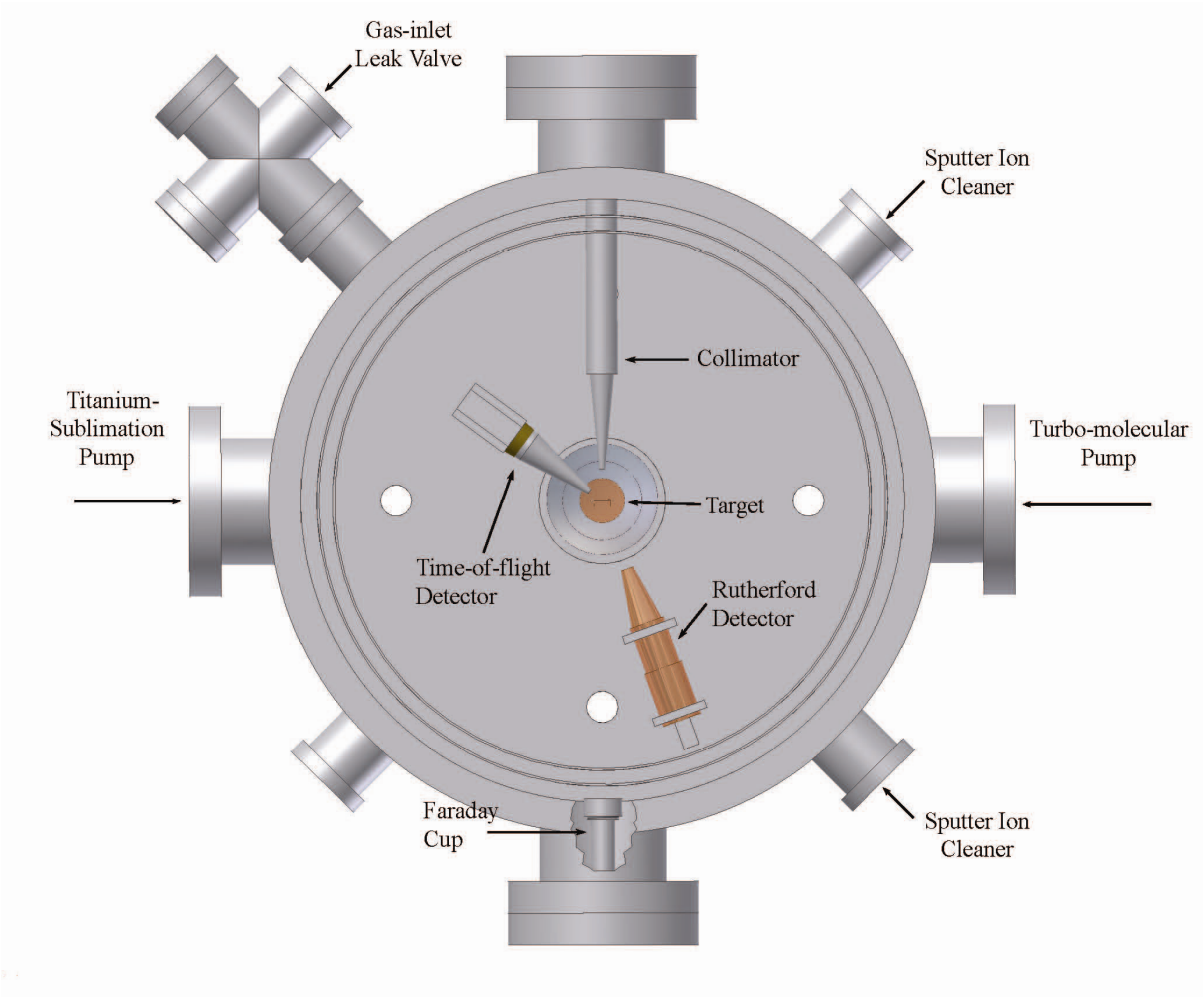

Figure 3.2. Top view of the UHV target chamber. Ports for vacuum pumps were located on either side of the chamber. The collimator was used to define the position of incoming particles on the target. The target was located in the center of the chamber and followed by a Faraday cup for measuring beam current. Ports for sputter cleaners were located at 45° and 135°. The gas inlet leak valve was positioned at 90° on a cross. The TOF detector was mounted on an x, y, z, θ manipulator capable of rotating from 0° to 160°. The Rutherford scattering detector was mounted at approximately 20° with respect to the incident beam.

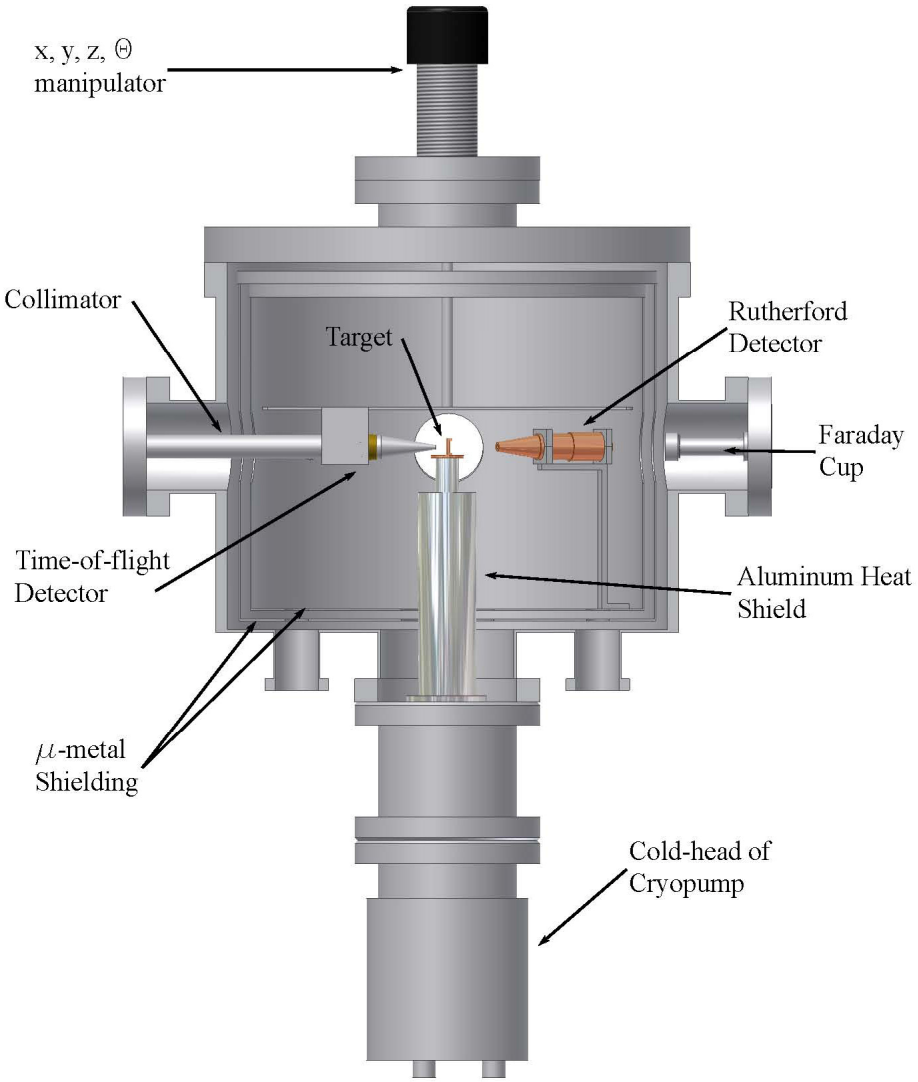

Figure 3.3. Side view of the UHV target chamber. The target was supported on a cold finger from the cryopump at the bottom of the chamber. The cold finger was enclosed in an aluminum heat shield to reduce radiative cooling and shield the target region from electrical potential. The TOF detector was mounted to an x, y, z, θ manipulator. The chamber included a double layer of μ metal shielding to reduce the magnetic field in the interaction region.

The chamber was also equipped with a Faraday cup positioned at the rear of the chamber opposite to the entrance collimator. The targets used in these experiments were thin compared to the range of the incident beam particles. As a result the Faraday cup could be used to collect beam current on the downstream side of the target. Under DC conditions where beam currents were large (1 to 10 nA) the current from the Faraday cup was used as a feedback to align the incoming beam with the collimator.

3.3.2: Target System

In these experiments commercially available high-purity, greater than 99.999% pure, copper foils were used both as a target and as a substrate for the deposition of frozen gases. These foils were obtained from Goodfellow Inc. The target assembly consisted of a copper support and base that aligned and supported the thin metal foil as shown in Figure 3.4. The connection of the target assembly with the other target system components is shown in Figure 3.5. To allow the pulsed beam to pass through the foil a 5 mm hole was drilled in the support with the edges beveled to 45°. This allowed all secondary electrons emitted at angles that intersect the acceptance cone of the detector to escape the target without material obstruction from the support.

The support and base were mounted on a copper tube supported by a hollow sapphire tube that acted to provide both thermal conduction and electrical isolation of the target assembly as shown in Figure 3.6. To accommodate frozen gas targets the target assembly and sapphire tube were attached to the cold finger of a cryogenic helium refrigerator. The helium refrigerator allowed compressed helium to expand in a cold head thus cooling the head to cryogenic temperatures. In operation the cold finger could be

cooled to a temperature of approximately 15 K at the cold head. Thermal conduction through the sapphire tube and target assembly allowed the target foil to reach temperatures of 30 K to 45 K. These temperatures were sufficiently low to allow injected water vapor to condensate on the foil substrate amorphously without the crystal structure typically associated with ice [54].

A set of ceramic flash heaters were installed around the copper tube that supported the target assembly. These heaters could be used to rapidly heat the target for the purposes of degassing and removing deposited material with little temperature increase noted on the other system components such as the cold finger. A set of thermocouples were placed approximately 0.5 cm from the heaters to monitor temperature changes while the heaters were in use. During degassing the target was flash heated to approximately 225º Celsius. To achieve this temperature the output level of the heaters and monitoring of the thermocouples was performed by a temperature controller unit.

An aluminum heat shield was used to surround the cold finger providing additional thermal insulation. The aluminum shield also acted to shield the interaction region from electric fields produced by the heaters, thermocouples, and associated wiring.

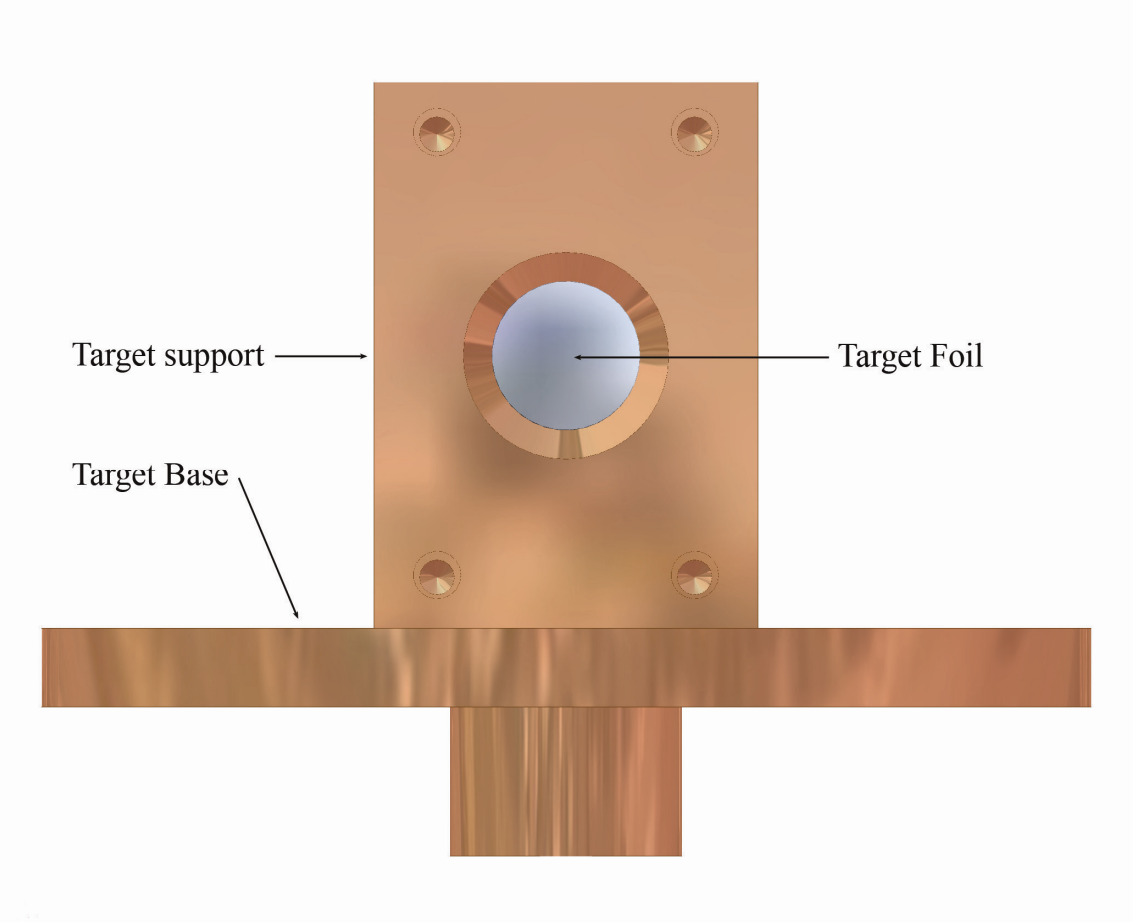

Figure 3.4. Drawing of the target assembly showing arrangement of the support, base, and target foil.

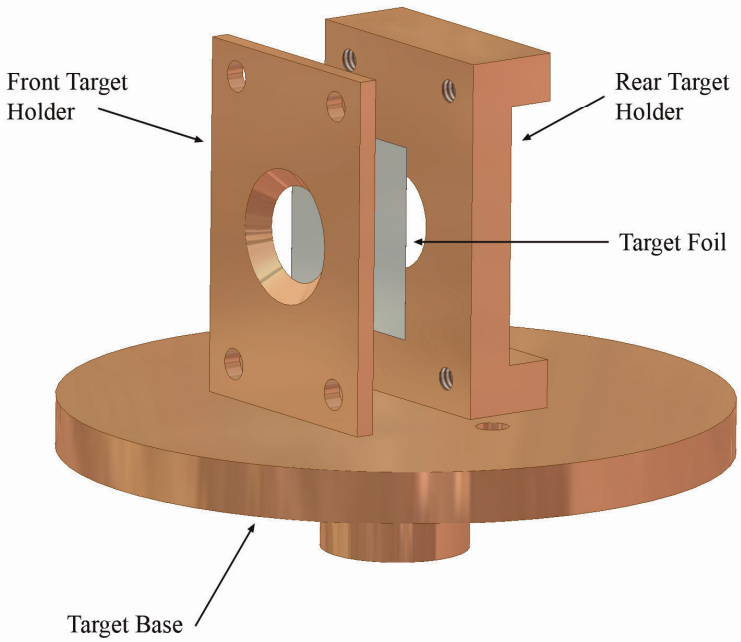

Figure 3.5. Cutaway view of the target foil, holder, and base.

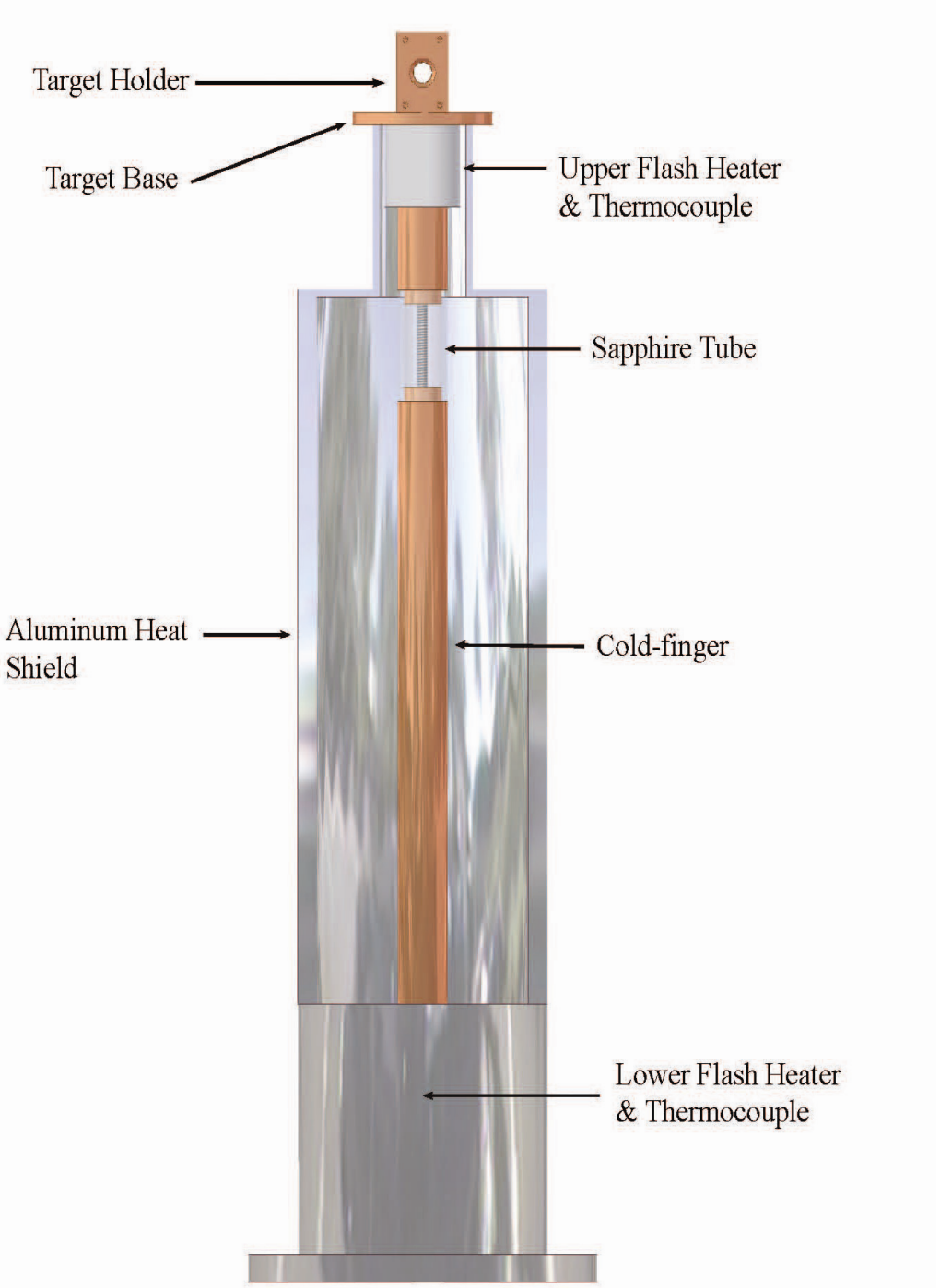

Figure 3.6. Illustration of the target assembly and cold finger. The cold finger was cooled by a cryogenic refrigerator. Flash heaters and thermocouples were installed near the target and near the cold head. An aluminum heat shield provided thermal insulation and shielding from electric fields. A sapphire tube insulated the target assembly electrically and provided thermal conduction from the cold finger.

3.3.3: Target Gas Injection and Auxiliary Components

A precision gas-inlet leak valve was used to inject high-purity water vapor into the chamber at low pressures (10^{-8} to 10^{-7} Torr). The leak valve was positioned at a 90° angle to the 45 ° port of the target chamber. This allowed for even background dosing of the target by preventing the injected gas from having a direct line of sight to the target, and thus preventing errors in target thickness estimation. The collision chamber was also equipped with a residual gas analyzer (RGA) that provided a measure of both the total chamber pressure and the partial pressures of constituent gases present in the chamber as water vapor was introduced. These measurements ensured the purity of the target gas deposited on the substrate and determined the concentrations of the remaining background gases.

Cryogenic cooling of the substrate prior to deposition took approximately 2 hours. During this time background gases present in the chamber condense and deposit on the surface of the copper foil used as the target substrate. Cleaning the copper foil before target deposition was required to remove these contaminants as they can have a significant effect on secondary electron emissions. Such contaminants present on the copper foil decrease the work function of the metal resulting in increased emission of low energy electrons that can be seen in the target spectrum. These contaminants also contribute secondary electrons to the observed spectra by interacting directly with impinging particles.

For the purposes of cleaning the copper foil after cooling and prior to gas target deposition the collision chamber included a pair of ion guns capable of producing 1 to 5 keV beams of neon ions for use in sputter cleaning. These noble gasses do not bond

easily and have a freezing point lower than the target temperature. The ion guns were mounted to the 45° and 135° ports and aligned with the center of the target foil from both the front and back sides. During these experiments the foils were cleaned with neon ions for approximately 20 minutes. Following the initial cleaning an emission spectrum from the bare foil was taken. The target foil was then cleaned for an additional 5 minutes and another spectrum was taken. Cleaning was considered complete when further cleaning no longer affected the emission spectra from the bare foil. Examples of typical emission spectra before and after sputter cleaning of the foil are shown in Figure 3.7. The effects of cleaning the foil are most apparent in the emission spectrum between 10 and 100eV where surface contaminants appear to decrease the yield of electrons.

The thickness of accumulated target gas frozen on the substrate was determined from the chamber pressure and the time over which the given pressure was maintained. A program written in LabView® was used to monitor this facet of the experiment. The program assigned thickness values using units of Langmuir (L), where 1 L is equal to the exposure to gas pressure of 1×10^{-6} Torr for 1 second [55], and an assumed sticking fraction of 1. Typical chamber pressures during the introduction of water vapor were on the order of 1×10^{-7} Torr. The program recorded the measured chamber pressure while

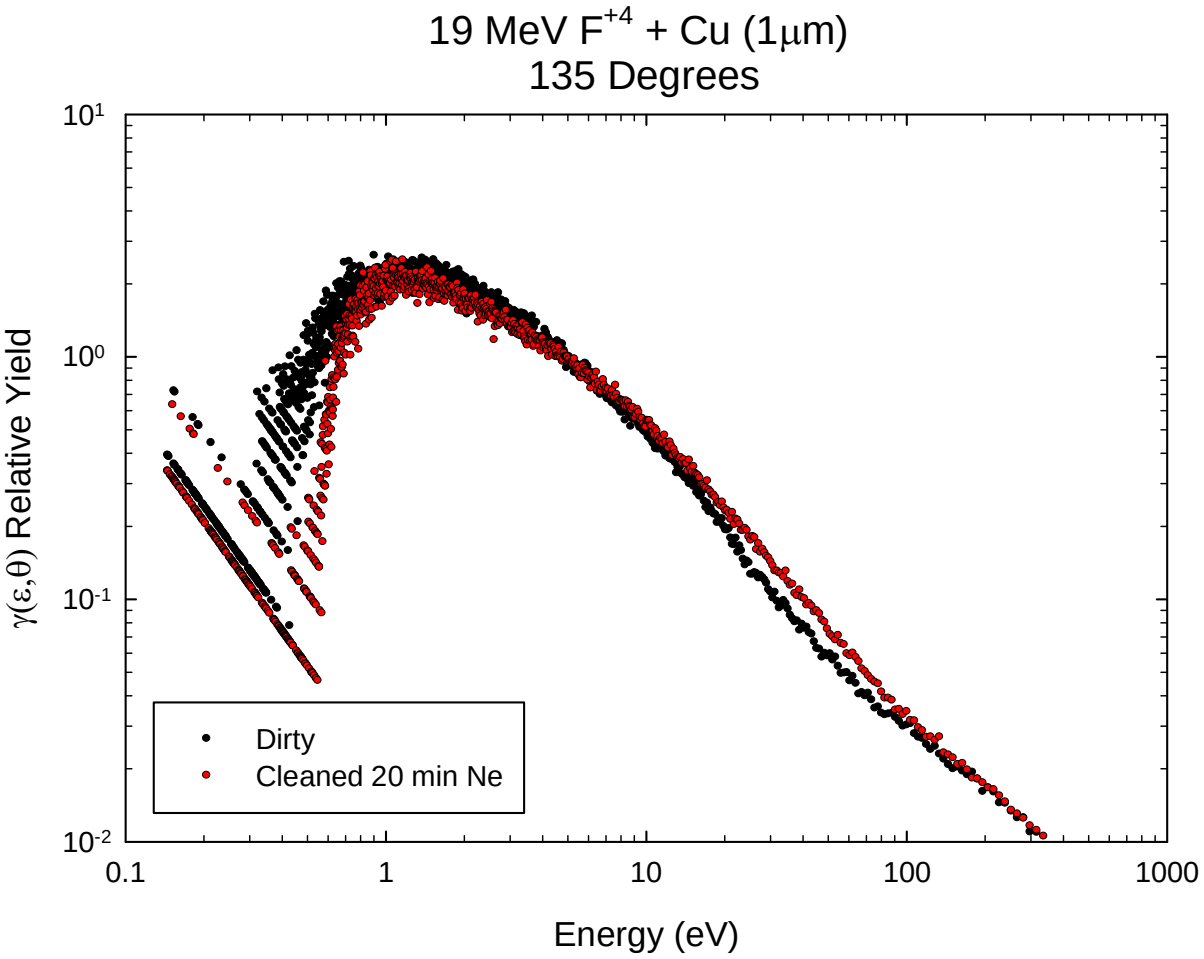

Figure 3.7. Relative yields from 1MeV/u fluorine on "dirty" and "clean" copper foil. The foil was sputter cleaned with neon for approximately 20 minutes.

gas was being injected and the accumulation time was determined from the program's internal clock. The number of layers deposited was then calculated and displayed in real time. The leak valve was manually closed when the desired number of layers was reached.

Water vapor injected as target gas under cryogenic temperatures (~45K) and UHV pressure conditions (10^{-9} to 10^{-10} Torr) will freeze as an amorphous solid rather than as a crystal [55]. In the deposition of amorphous solid water (ASW), doubly distilled water was sealed in an air tight vacuum bottle and atmospheric gases absorbed in the water were removed by the freeze-thaw method. The freeze thaw method involves freezing the water in a liquid nitrogen bath and rough pumping on the water over the course of 8 hours while it thaws under vacuum. This process was repeated three times. The effective removal of atmospheric gases from the water was confirmed using the residual gas analyzer during gas injection into the chamber. A typical RGA spectrum taken during the injection of water vapor is shown in Figure 3.8. For this example the total chamber pressure during the introduction of vapor was 8.4×10^{-8} Torr. Some gas concentrations (H_2, OH, and O) can be seen in the spectrum from water cracking. However nitrogen was a primary concern as it can imbed in deposited layers. Typically N_2 accounted for less than 3% of the total pressure.

3.3.4: Time-of-Flight Detector

The majority of electrons emitted from both the copper foil and the ASW targets have energies less than 50 eV. As a result, fringing electric fields from electrostatic energy analyzers will influence the path of electrons with such low energies. These effects can serve to introduce excessive error in yield measurements and poor low-energy

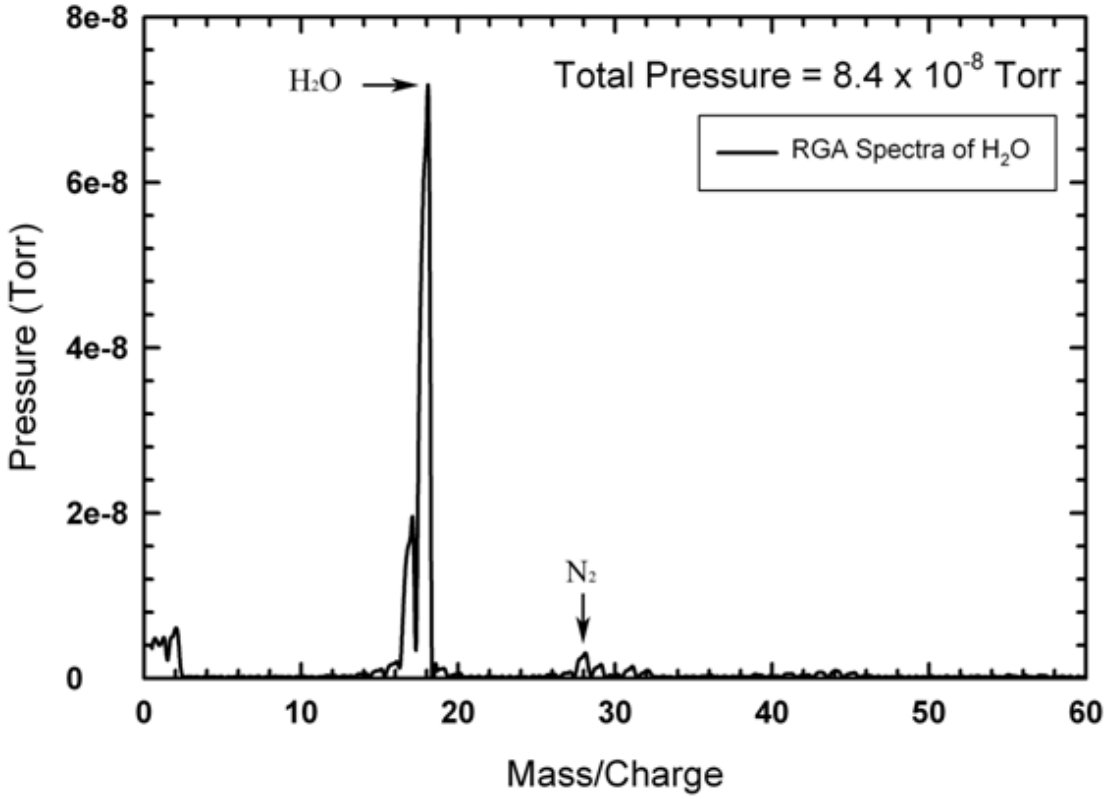

Figure 3.8. RGA spectra of H_2O (mass = 18) leaked into target chamber and frozen onto cryogenically cooled Cu substrate, producing an amorphous solid water target from which electron emission spectra was measured. From the spectrum it can be seen that water vapor including OH (mass = 17) was the primary gas in the chamber. The N_2 peak shown on the spectrum accounted for less than 3% of the total pressure.

resolution. For this reason, energy analysis by the time-of-flight (TOF) method was preferred for these experiments [56].

The TOF detector included a pair of microchannel plates (MCP) that collect charged particles incident on the plates and output a pulse series equal to the charge of particles collected. A thorough discussion of MCP operation has been presented by Wiza [57]. Figures 3.9 and 3.10 show the TOF detector in relation to the target and in a detailed exploded view. The entrance aperture of the TOF detector immediately downstream of the detector cone was 12.7 mm from the target. This was followed by two collimators, one with a second non-defining aperture 3.2 mm in diameter and a rectangular collimator with a slot 9mm x 3mm and defining a solid angle of 2.9×10^{-4} sr was in place just in front of two transmission grids to prevent scattered electrons from reaching the microchannel plates. All structures including the detector cone, collimators, and grids were held at ground potential. The total distance through this field free region was 89.4 mm. The front microchannel plate (FMCP) was separated from the second transmission grid by 2.1 mm. This yielded a total distance of travel from the target to the FMCP of 91.5 mm.

An illustration of the wiring for the TOF detector is shown in Figure 3.11. The optimal bias voltage for the TOF detector was determined by incrementing through many voltages to maximize the detector count rate. The count rate increases with increasing voltage until the bias reaches approximately 1750 V. At this voltage the count rate begins to reach a plateau where additional bias voltage yields no additional detector counts. A bias setting of 1900 V was used throughout the experimental work. This value was well

centered in the plateau region and did not risk damage to the microchannel plates from excessive bias voltage.

Detection efficiency for low energy electrons was increased by pre-accelerating incoming electrons to approximately 50 V. This was accomplished by holding the FMCP at a potential of 50 V relative to the last grid. The distance over which this voltage acted on the electrons was 2.1 mm which is small compared to the field free path of 89.4 mm. As such, the effect of the pre-acceleration voltage on the total electron time-of-flight was negligibly small accounting for approximately 2.5% or less of the total flight time for the 1eV electrons. The second microchannel plate (BMCP) was held at a potential of 1875 V. An insulating ring approximately 1 mm thick was used to separate the BMCP from the anode. The anode was held at a potential of 1900 V with the 25 V difference between the BMCP and the anode being used to extract electrons from the BMCP.

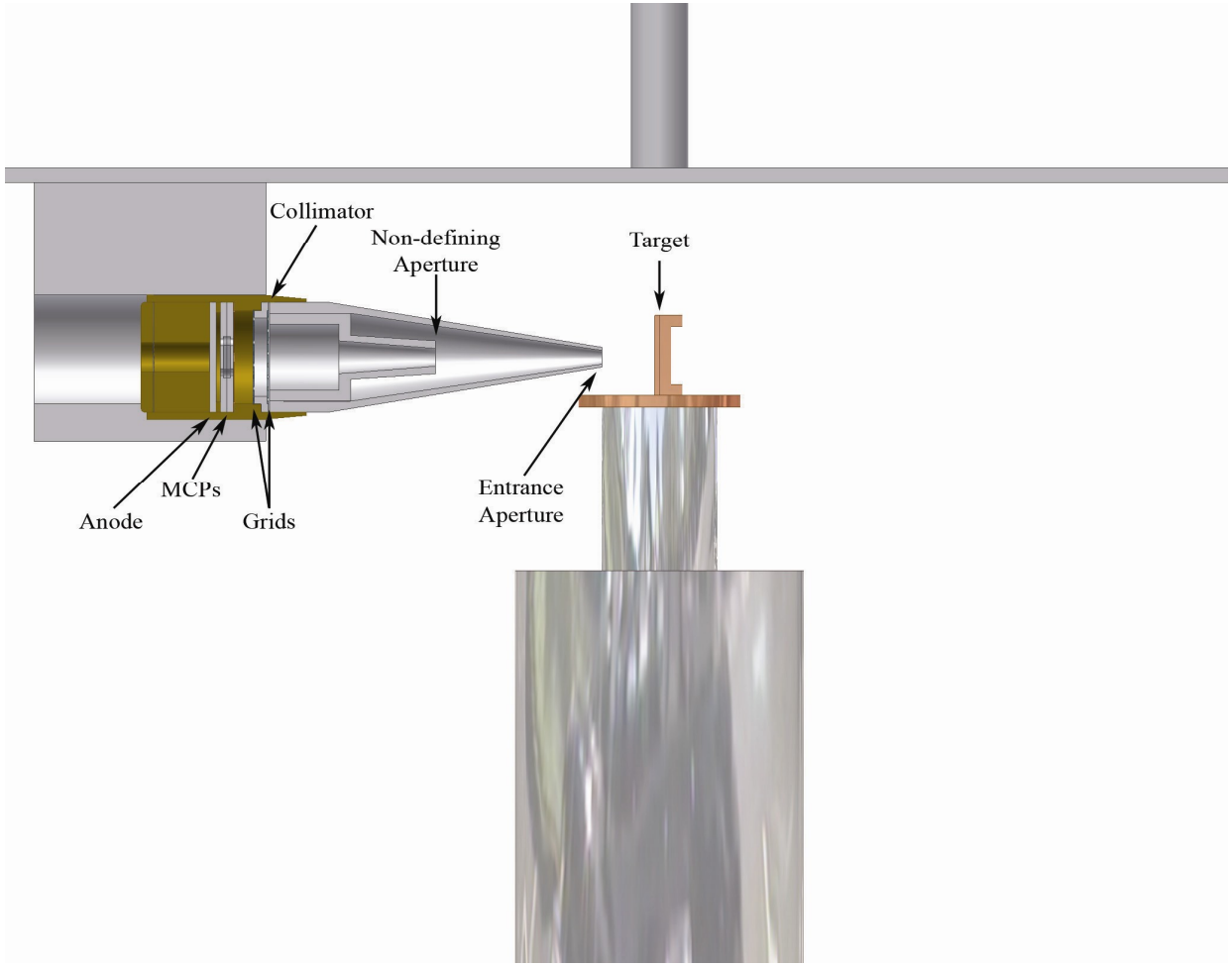

Figure 3.9. Cutaway view of the TOF detector in relation to the target.

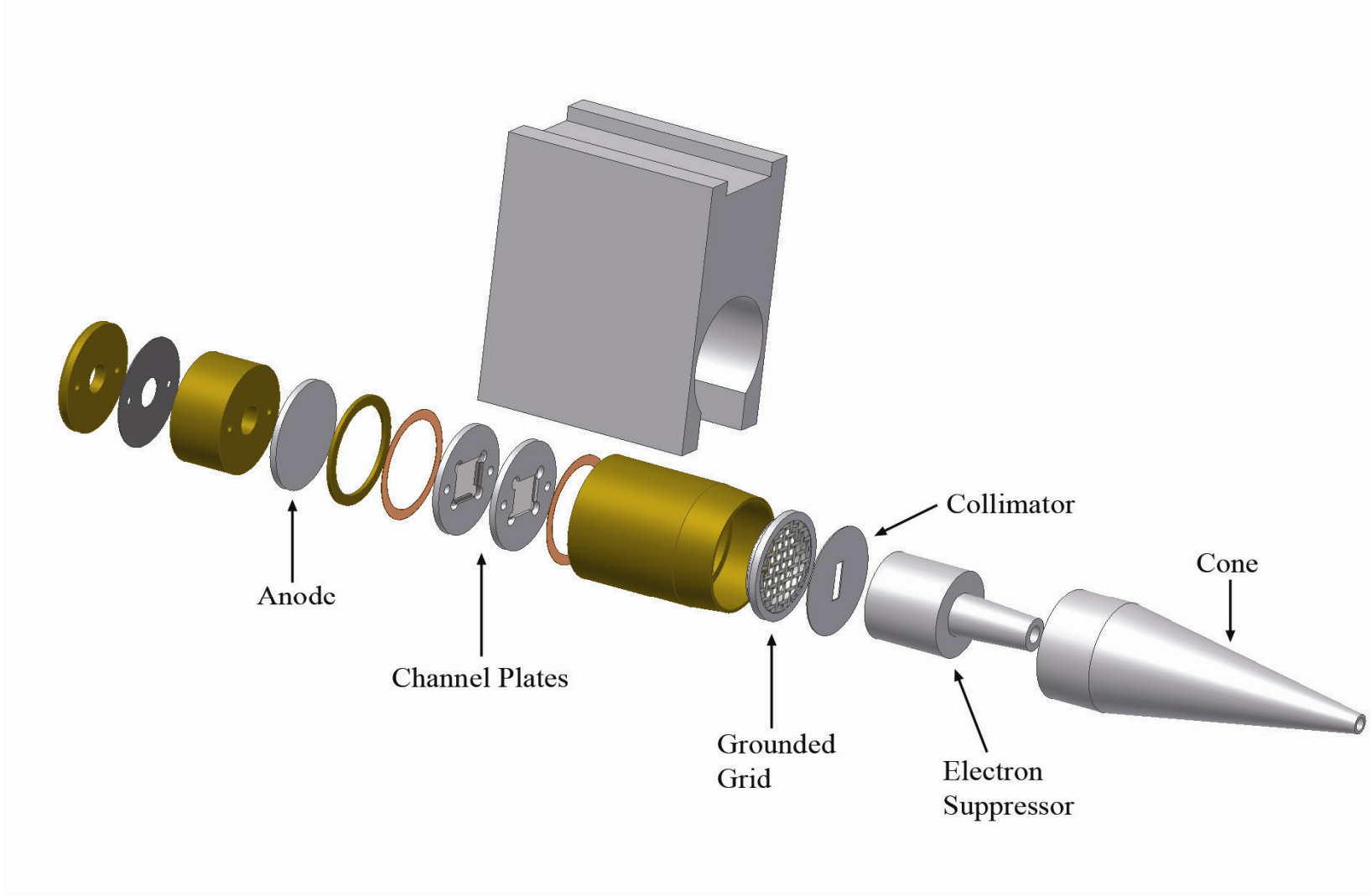

Figure 3.10. Exploded view of the TOF detector.

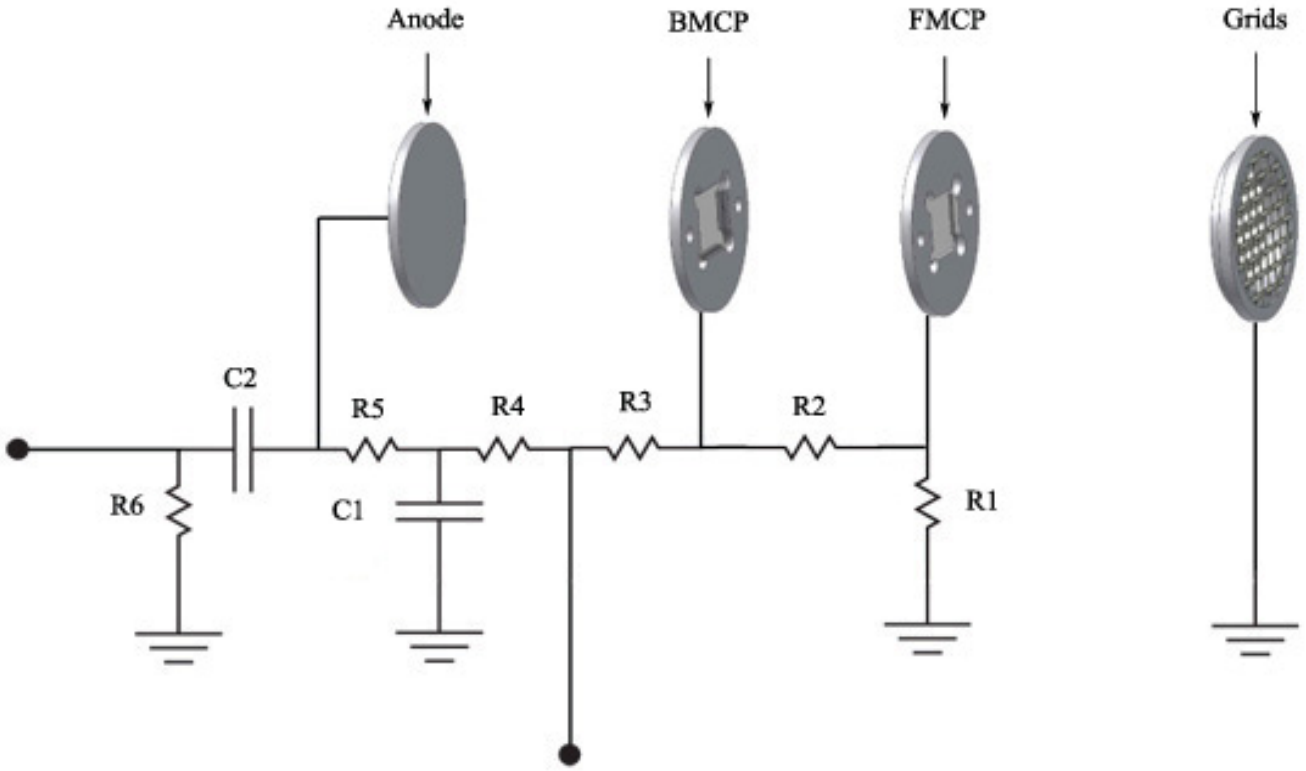

Figure 3.11. Circuit diagram for the TOF detector. The grids were held at ground potential. The FMCP was held at 50 V and the BMCP was held at 1875 V. The anode was held at a potential of 1900 V.

3.3.5: Rutherford Scattering Detector

Under typical pulsed beam conditions the beam current was too low to be measured by the Faraday cup. Throughout the experimental runs a second particle detector was used to count incident beam particles scattered into the detector by the process of Rutherford scattering. The Rutherford scattering data were used to provide a relative measure of the beam current for data normalization.

A schematic of the Rutherford scattering detector is shown if Figure 3.12. The detector consisted of a channel electron multiplier (CEM) encased in an electrically grounded copper housing. The copper housing acted to shield the target area from electric fields generated by the CEM. Inside the copper housing the CEM was mounted to an ceramic support made of alumina to provide electrical isolation between the CEM and the grounded housing. The entrance aperture had a diameter of 5 mm and inside the housing an 11 mm diameter collimator was placed at the entrance of the CEM cone. The whole assembly was positioned in the chamber approximately 75 mm from the target at an angle of approximately 20° with respect to the incident beam. This detector was used only for relative measurements, as such, specific knowledge of the detector efficiency and solid angle were not critical.

The electrical wiring of the CEM is shown schematically in Figure 3.13. A bias potential of -1800 V was placed at the entrance cone and a bias of 600 V was placed at the electron collector of the CEM. Together these potentials provide 2400 V across the

CEM from cone to collector, and this bias voltage was found to maximize the efficiency of the detector. Typical biasing of CEM detectors leaves the cone at ground and places all potential on the collector. The current arrangement, with a potential of -1800 V at the cone, had the advantage that it acted to repel most secondary electrons emitted from the target. Thereby, only scattered beam particles and high energy electrons were detected by the CEM. These higher energy particles were considerably less dependent on the surface conditions of the target. This allowed comparisons of different runs on the same target regardless of changing surface conditions.

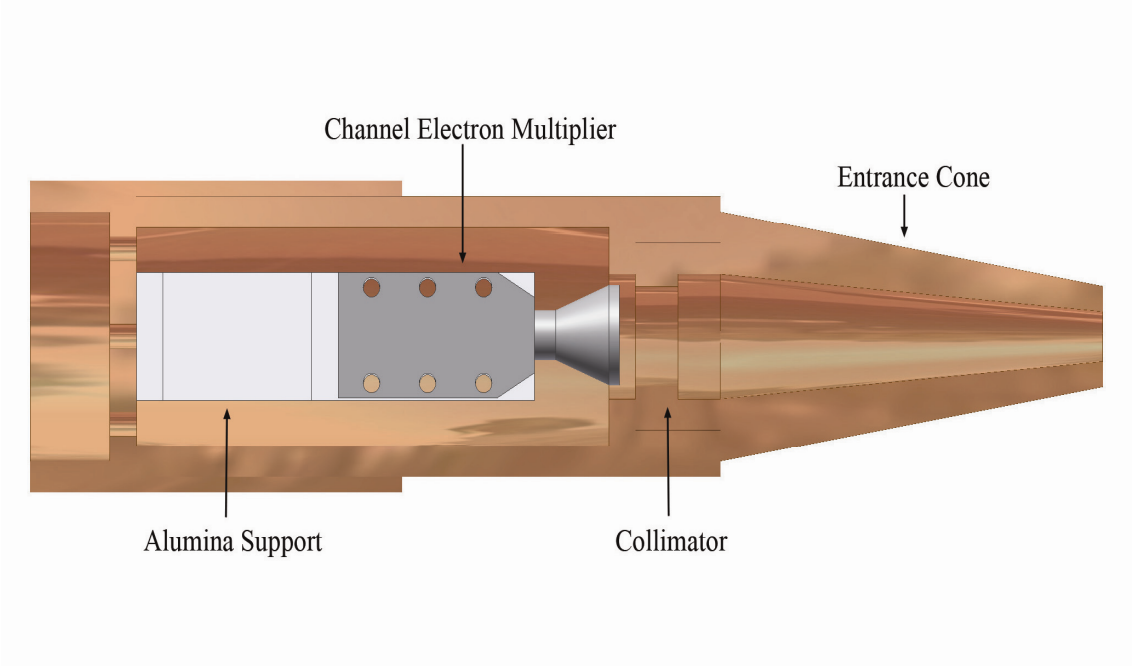

Figure 3.12. Cutaway view of the Rutherford detector.

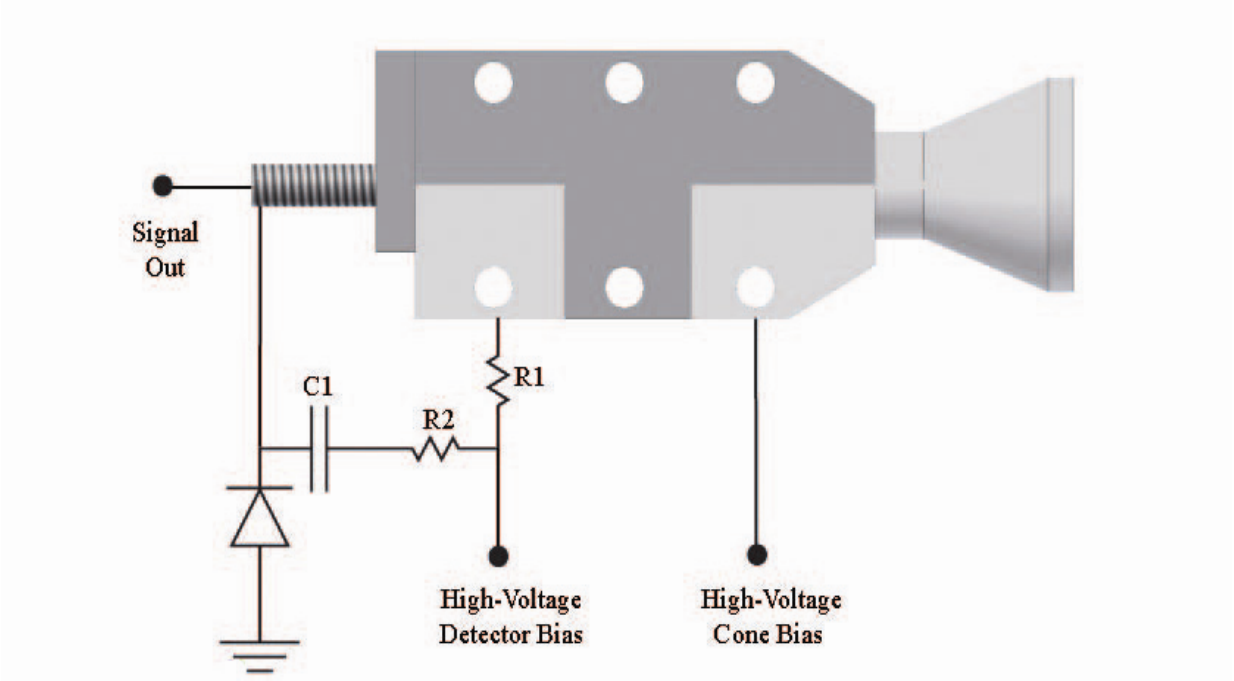

Figure 3.13. Wiring diagram for the CEM in the Rutherford detector.

3.3.6: Data Acquisition System

The data acquisition system used in experiments at KSU is shown schematically in Figure 3.14. The output signals from the TOF detector were amplified and input to a constant fraction discriminator (CFD). The CFD acted to eliminate low-voltage noise from the detector signal. The output of the CFD is a fast negative pulse. This pulse was used as the start signal for the time-to-amplitude converter (TAC). The stop signal for the TAC was a negative pulse originating from the buncher system. The pulse from the buncher was sent to a delay and then used as the stop signal. This was accomplished by sending the output signal from the buncher to another CFD. The output of this CFD was again a fast negative pulse. The pulse from this CFD was delayed by 100-150 ns and then sent to the TAC as the stop signal. The output signal from the TAC was a voltage whose value was proportional to the time difference between the start and stop signals. This signal was then sent to a multichannel analyzer (MCA) that was used to record the number of counts in each channel. The MCA could collect and distribute data from the detector over 2048 channels. The channel numbers were assigned by the pulse height of the TAC output.

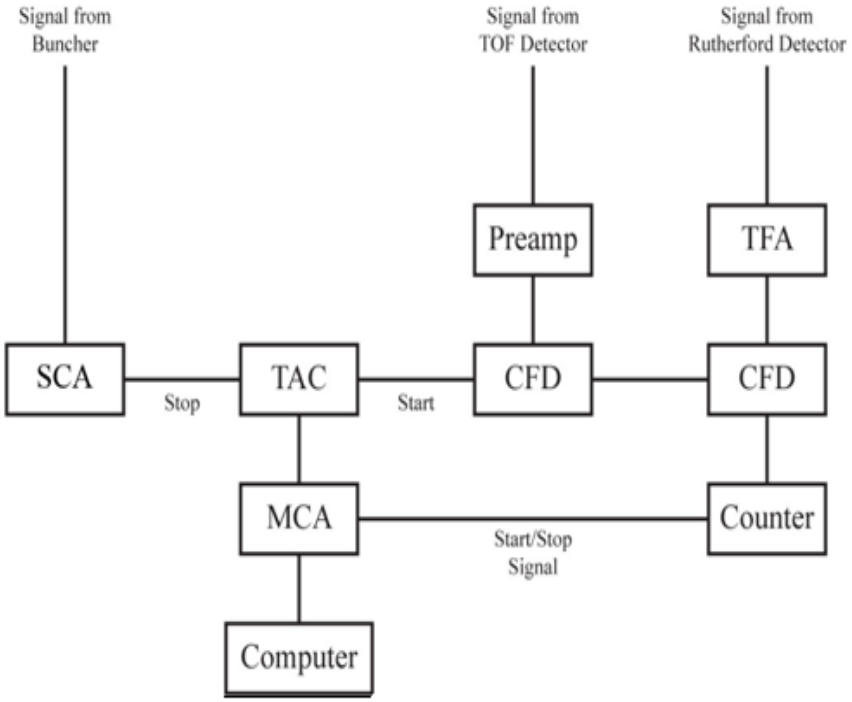

Figure. 3.14. Block diagram of data acquisition electronics used at KSU.

The number of counts from the Rutherford scattering detector was simultaneously recorded with the TOF measurements. The MCA produced start and stop signals for the counter used with the Rutherford scattering detector that coincided with the starting and stopping of the TOF measurements. The signal from the Rutherford detector CEM was sent to a timing-filter-amplifier (TFA) to shape and amplify the output signal. The signal from the TFA was sent to a CFD to discriminate against low-voltage noise. The fast negative output pulses from the CFD were recorded by the counter. The recorded scattered counts were used in data normalization.

3.4 Data Analysis

Doubly differential electron emission yields were obtained from the number of counts recorded in each channel of the MCA at each angle. To accomplish this task the channel numbers from the MCA have to be correlated to the electron time-of-flight. A time scale calibrator was used to generate start and stop signals that were fed to the TAC in place of the normal signals used during experiments. The signals from the calibrator occurred at precise intervals that were stated to be accurate to ±0.005% of the total period. The signals from the calibrator created defined spectral peaks with spacing between the peaks equivalent to the time period. When these pulses were recorded by the MCA they appeared as counts assigned to channels. With a known time period, the channels of the MCA can be correlated with the channel numbers. A number of measurements were made varying the time period between the pulses from the calibrator.

Figure 3.15 shows a typical time scale calibration spectrum where the time between peaks was set to be 40 ns. The number of channels between each peak was found to be 158 which yields a time scale calibration factor Δ_t of 3.95 channels/ns.

To complete the conversion of the MCA spectra to electron time-of-flight spectra it was necessary to determine the MCA channel that corresponded to the zero-time (t=0). The zero-time channel varied from day to day, but was stable over the time periods in which data was taken. As such, initial spectra were taken daily to identify the zero-time channel and retaken at the end of the day to confirm no drift had occurred. The zero-time channel was determined by taking a spectrum with the TOF detector positioned at 0° with respect to the incident beam. At 0° the spectrum takes the form of a sharp Gaussian peak. This peak is formed by both incident beam particles passing through the target and fast electrons liberated from the target through collision. The time required for the incident beam particles to travel from the target to the detector was determined from the known particle energy and target to detector distance. Using the time scale calibration factor, the flight time was calculated and converted to the corresponding MCA channel using the value of Δ_t previously determined. The number of channels corresponding to the incident particle flight time was then subtracted from the channel number containing the 0° peak. This yielded the zero-time channel. The time scale calibration factor was then used to convert the spectra from channel number to time-of-flight.

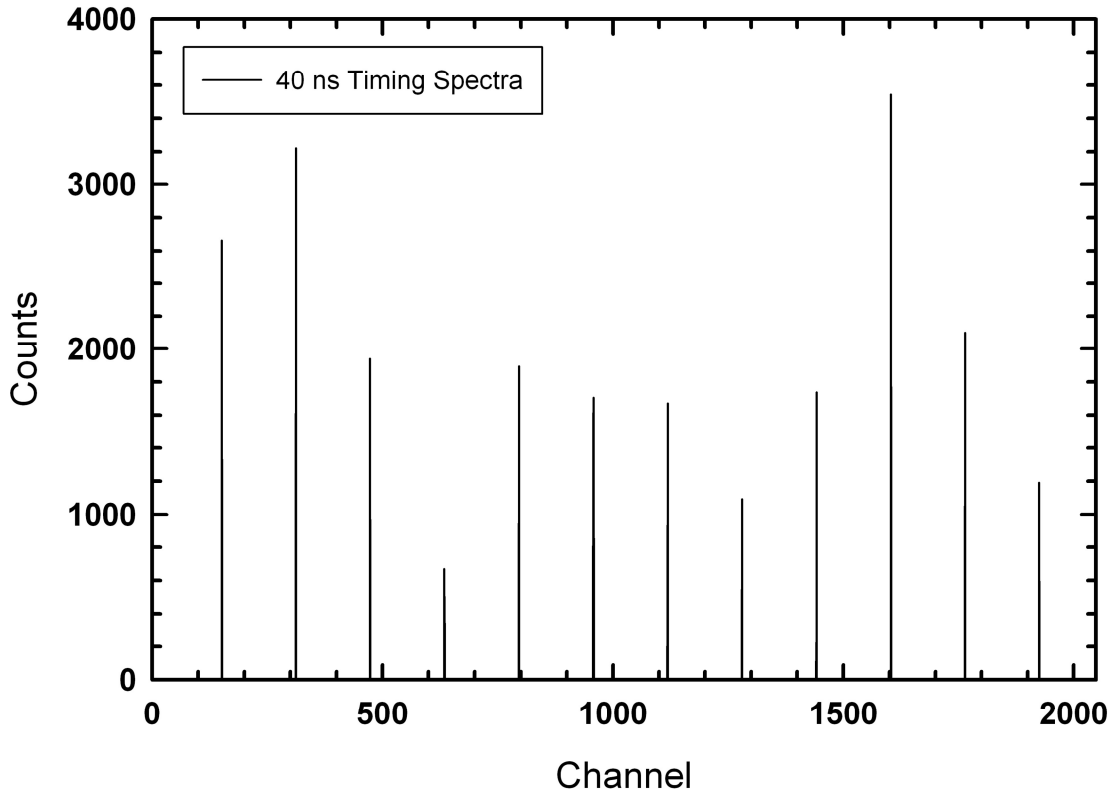

Figure 3.15. Typical spectra from time scale calibrator. The time scale calibrator was set to send a pulse every 40 ns. These pulses appear on the MCA 158 channels apart, giving a time scale calibration factor Δ_t of 3.95 channels/ns.

As an example, a typical zero degree timing spectrum for 2 MeV H^+ incident on a 1 μm Au foil taken during preliminary work at ECU is shown in Fig 3.16. In this example the zero-degree peak is located in channel 1788. The 2 MeV proton traversed the 88.2 mm distance from the target to the detector in 4.5 ns. The time-of-flight scale was obtained by the relation

$$t = \left| \frac{Ch_0 - Ch_t}{\Delta_t} \right|, \tag{3.1}$$

where Ch_t is the channel number from which the time is being determined, Ch_0 is the zero time channel, and Δ_t is again the time scale calibration. The zero time channel Ch_0 was determined from

$$Ch_0 = Ch_{proton} - (4.5ns)(\Delta_t), \tag{3.2}$$

where Ch_{proton} is the channel containing the 0° proton peak. The energy of the emitted electrons corresponds to their flight time using the relationship

$$E = \frac{1}{2}mv^2 = \frac{1}{2}m\left(\frac{d}{t}\right)^2, \tag{3.3}$$

where m is the mass of the electron, v is the velocity of the electron, d is the distance of the electron flight path, and t is the time for the electron to travel through distance d. Low energy electrons have long flight times while high energy electrons have short flight times. This same procedure was used to determine the time scale for 6 MeV protons and 19 MeV fluorine ions.

The 0° peak was also used to determine the timing resolution of the system using the width of the peak at half maximum. The timing resolution of the system during data collection was typically around 2.5ns for 6MeV protons and 4ns for fluorine ions depending on daily beam conditions. As an example a typical 0° spectrum for 2 MeV H^+ incident on a 1 μm Au foil is shown in figure 3.16. From figure 3.17 the width of the peak at half maximum is approximately 7.96 channels. Applying the time scale calibration factor obtained from the spectrum yields a timing resolution of approximately 2 ns.

With the time scale factor determined the energy of the electrons was then calculated by again applying equation 3.3. The electron time-of-flight distribution $\gamma(t,\theta)$is given by

$$\gamma(t,\theta) = \frac{N_e}{N_p \xi T \Omega \Delta_t}, \tag{3.4}$$

where N_e is the number of electrons recorded in each channel, N_p is the number of incident particles, ξ is the electron detection efficiency, T is the transmission coefficient of the detector grids, Ω is the solid angle subtended by the detector in steradians, and Δ_t is the MCA time scale calibration factor in seconds.

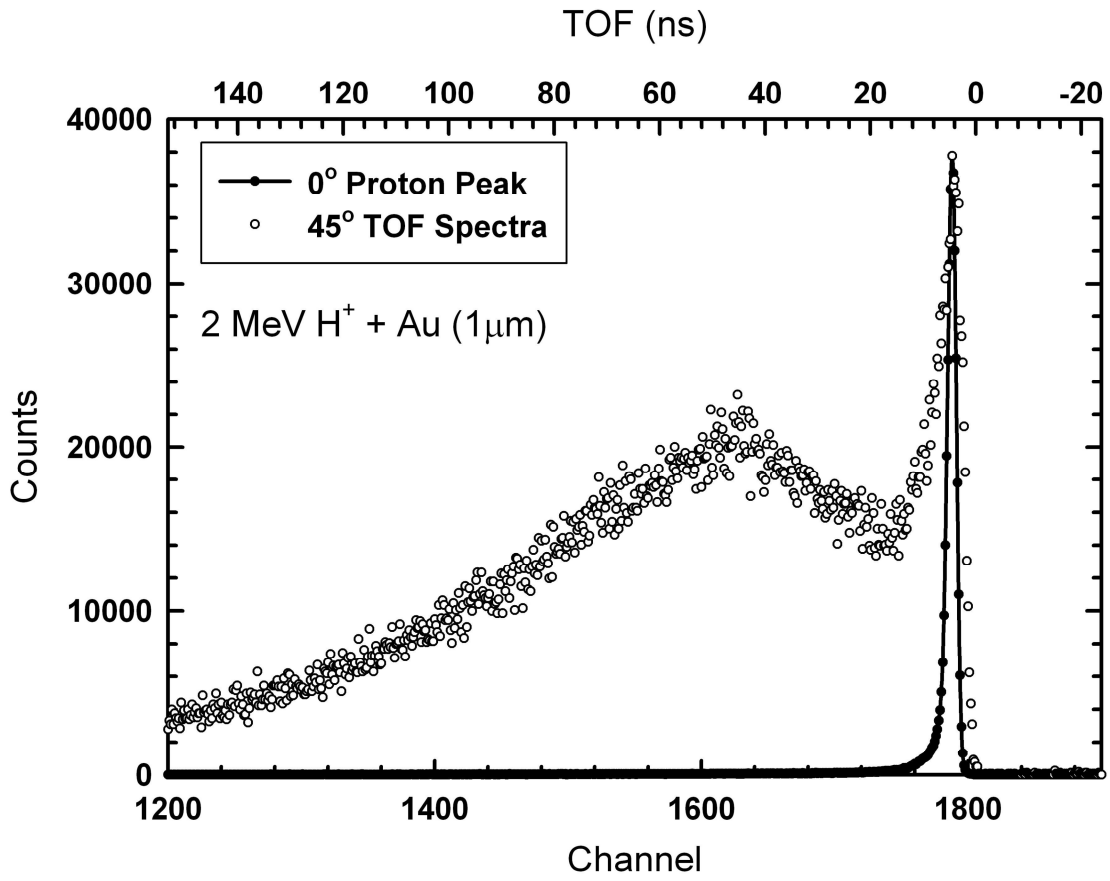

Figure 3.16. The 0° proton peak is shown in comparison to a 45° emission spectrum.

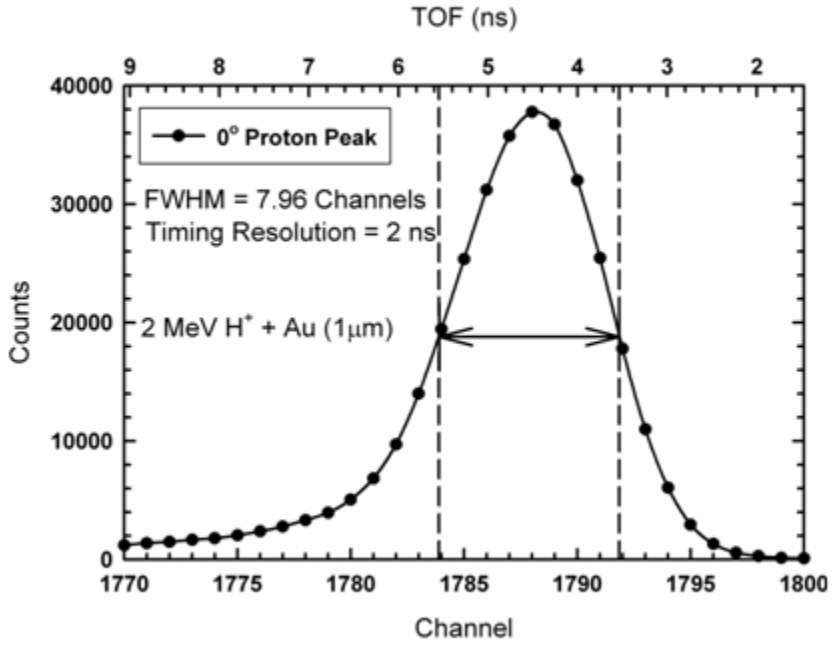

Figure 3.17. The timing resolution is determined from the 0° proton peak.. From the FWHM of the peak the timing resolution was determined to be approximately 2 ns.

The electron energy distribution $\gamma(\varepsilon,\theta)$ was obtained from the electron time-of-flight distribution by

$$\gamma(\varepsilon,\theta) = \left|\gamma(t,\theta)\left(\frac{dt}{d\varepsilon}\right)\right|, \tag{3.5}$$

where ε is the energy of the electron given by equation 3.3.

From equations 3.3 and 3.5 the electron energy distribution is given by

$$\gamma(\varepsilon,\theta) = \frac{N_e m d^2}{N_p \xi T \Omega \Delta_t t^3} \quad . \tag{3.6}$$

Due to the low beam currents used in these experiments the number of incident particles N_p could not be determined directly by use of the Faraday cup. Instead relative measurements were made by normalizing the number of counts in each channel of the MCA to the number of scattered counts detected by the Rutherford scattering detector. The relative measurements are given by

$$\gamma(\varepsilon,\theta)_{rel} = \frac{N_e m d^2}{N_{sp} \Delta_t t^3}, \tag{3.7}$$

where N_{sp} is the number of scattered counts detected by the Rutherford scattering detector.

A typical TOF spectrum and the resulting energy spectrum for 2 MeV H^+ incident on a 1 μm Au foil is shown in Fig. 3.18. The electron emission spectrum was measured at 45° with respect to the incident beam. The timing scale shown on the top axes in Fig.

3.18 (a) was determined using equation 3.1. The energy spectrum in Fig. 3.18 (b) was determined using equation 3.3 for the energy scale and equation 3.7 for the differential electron energy yield.

Absolute doubly differential electron emission yields were obtained by numerical integration of the relative yields over energy and angle and comparison to totals for published data. For copper targets the results were normalized to published values of the total electron emission yields for the same target and projectile [58]. For ASW targets where measurements of the total yield were unavailable, the emission spectra from the Cu foil used as a substrate was used for normalization.

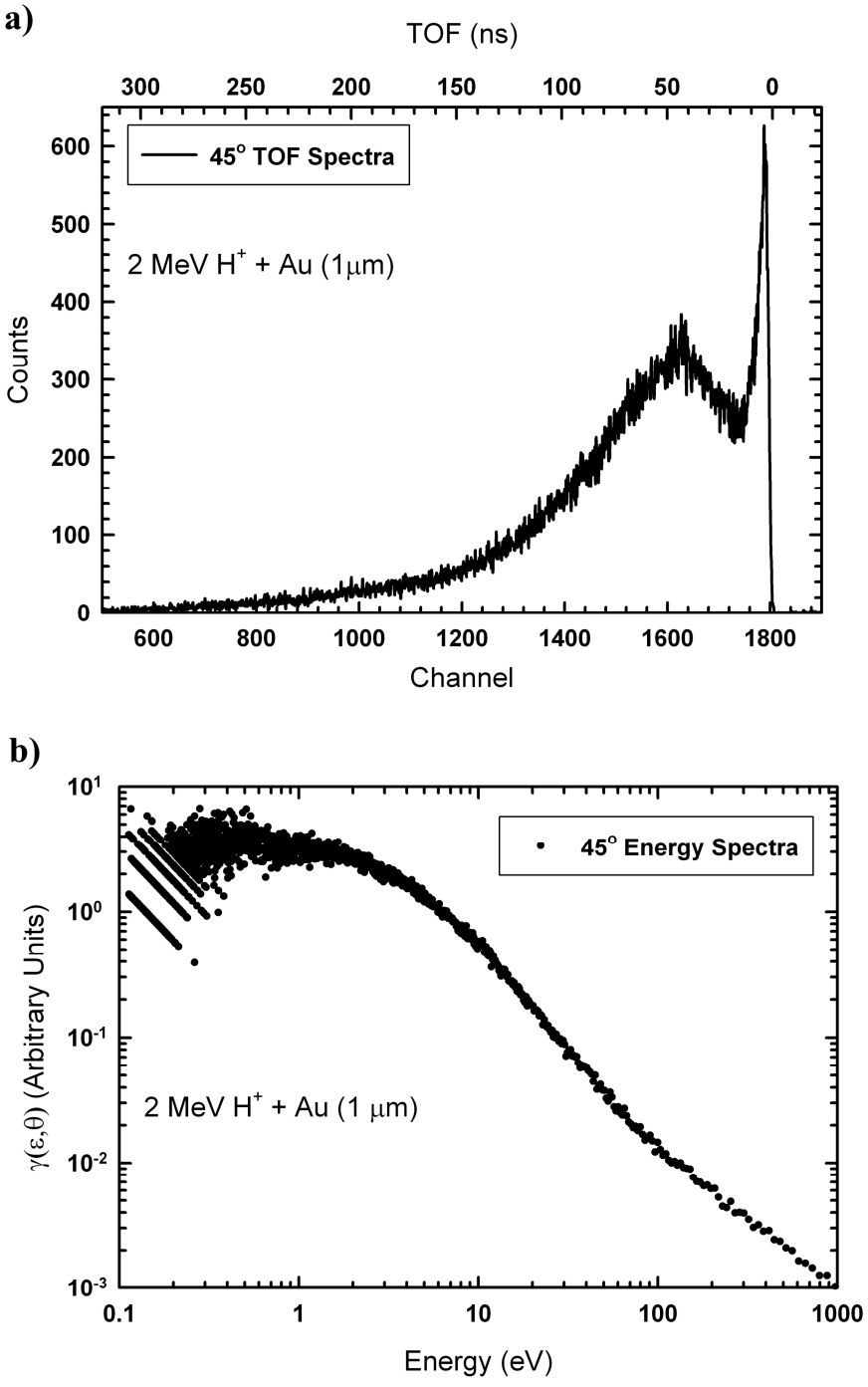

Figure 3.18. The TOF spectrum for 2 MeV H^+ + Au is shown in Fig. 3.14(a). The resulting electron energy distribution is shown in Figure 3.14(b).

Chapter 4: Results and Discussion

4.1: Introduction

Doubly differential electron emission yields $\gamma(\varepsilon,\theta)$, differential in energy ε and emission angle θ, as a result of impact by 19 MeV Fluorine ions equal to 1MeV/u on copper and amorphous solid water targets are presented. Collisions with thin foils (1μm) of copper were studied to provide a database of homogenous target emission from which future comparisons with theoretical and computational models can be made. Additionally, thin Cu foils served as the substrate for frozen amorphous solid water films making knowledge of the electron emission spectra from Cu important in interpretation of the frozen ASW data. Electron emission yields from amorphous solid water targets expand our understating of the production and transport of secondary electrons in molecular environments lending insight into elastic and inelastic scattering within the medium as well as the effects of target charging. These measurements of ASW targets provide a starting point for future studies of electron transport in macromolecules and complex heterogeneous targets, such as proteins, DNA, and tissue.

Doubly differential electron emission spectra from 19 MeV F^{+4} ions passing through 1μm Cu foils are presented in section 4.2. The spectra from the double-differential yields are discussed along with total electron emission yields γ, and comparisons are made with previous proton data.

The results from 19 MeV F^{+4} impact on amorphous solid water frozen on Cu foil substrates are presented in sections 4.3 and 4.4. The amorphous solid water targets provide a biologically relevant medium from which comparisons with computational models can be made in the future. The electron emission spectra as a function of water exposure are presented in section 4.3. These results are presented as an estimate of the electron emission yield dependence on target thickness. The double-differential electron emission spectra are presented and discussed in section 4.4 along with presentation of single and total emission yields.

4.2: Electron Emission Spectra from Copper Foils

The electron emission spectra for 19 MeV F^{+4} incident on a 1-μm Cu foil are shown in Figures 4.1 and 4.2. Figures 4.1 and 4.2 are results from the forward and backward angle sets respectively, and Figures 4.3 and 4.4 are the same data scaled to allow the spectra to be more clearly seen without overlap. Figures 4.5 and 4.6 are the forward and backward spectra for 6 MeV H^+ impact on a 1-μm Cu foil from the dissertation by R.A. McLawhorn [19], and measured with the same experimental system. The emission spectra from 6 MeV H^+ impact are presented here for comparison, and to provide background as the 19 MeV F^{+4} data was normalized by scaling the relative number of scattered particles using Rutherford scattering theory to the 6 MeV H^+ data. In turn, the 6 MeV H^+ electron emission spectra were normalized to the total electron emission yields of Koyama, Shikata, and Sakairi [58].

The electron emission spectra from 19 MeV F^{+4} in the forward direction (Figures 4.1 and 4.3) show a broad low-energy peak at approximately 0.7 eV on the 15° spectrum. This peak progressively shifts higher in energy with increasing emission angle until reaching approximately 1.1 eV on the 60° spectrum. The height of the low-energy peak decreases by approximately 50% from 15° to 60°. The low energy cutoff increases in these spectra with increasing emission angle. This increase in the cutoff energy results from the low energy electrons requiring a greater velocity component normal to the surface to escape the surface potential. The electron emission yield spectra at each angle follow the same general trend and the shape is independent of emission angle. The low energy peak dominates the emission spectrum and the yield of electrons rapidly decreases with increasing energy.

The spectra for electron emission in the backward direction as a result of 19 MeV F^{+4} impact on a 1-μm Cu foil are shown Figures 4.2 and 4.4. The low-energy peak is located at 0.75 eV on the 155° spectrum and shifts forward with decreasing emission angle until it reaches approximately 1.1 eV on the 115° spectrum. The height of the low-energy peak decreases by approximately 50% from the 155° spectrum to the 115° spectrum. Again, the yield of electrons quickly drops with increasing energy from 10 eV to 1000 eV, and the trends and shape of the electron emission spectra are each independent of emission angle.

In comparison with the 6 MeV H^+ data presented in Figures 4.5 and 4.6 there is little difference in the low energy portion of the spectra apart from the yield which is an order of magnitude higher for 19 MeV F^{+4} emission. The shapes of the spectra are similar and the effects of shifting peak energy and cutoff energy are comparable. The major difference however is in the spectra from 100 eV to 1000 eV. There is a slight enhancement in the fluorine yields owing to binary encounter electrons in the secondary electron production spectra. These enhancements are most evident at small emission angles as the binary encounter electrons have energies given by (2200eV x $\cos^2\Theta$) However, it is the additional emission from convoy electrons and electrons stripped from bound states of the ions as they traverse the target that creates the distinct bulge in the high energy portion of the 19 MeV F^{+4} data [59, 60]. These additions to the yield are electrons that follow in the wake potential of the incidents ions. In this case, these electrons have equivalent velocities to the impinging fluorine ions that are emitted with energies of approximately 545 eV. This peak is broadened greatly in the plots presented here due to the poor resolution of the TOF system in that energy range.

Finally, the data presented was integrated over angle and energy to determine total emission yields for 19 MeV F^{+4} on Cu. This value was determined to be $\gamma = 34 \pm 3$ electrons/ion [61].

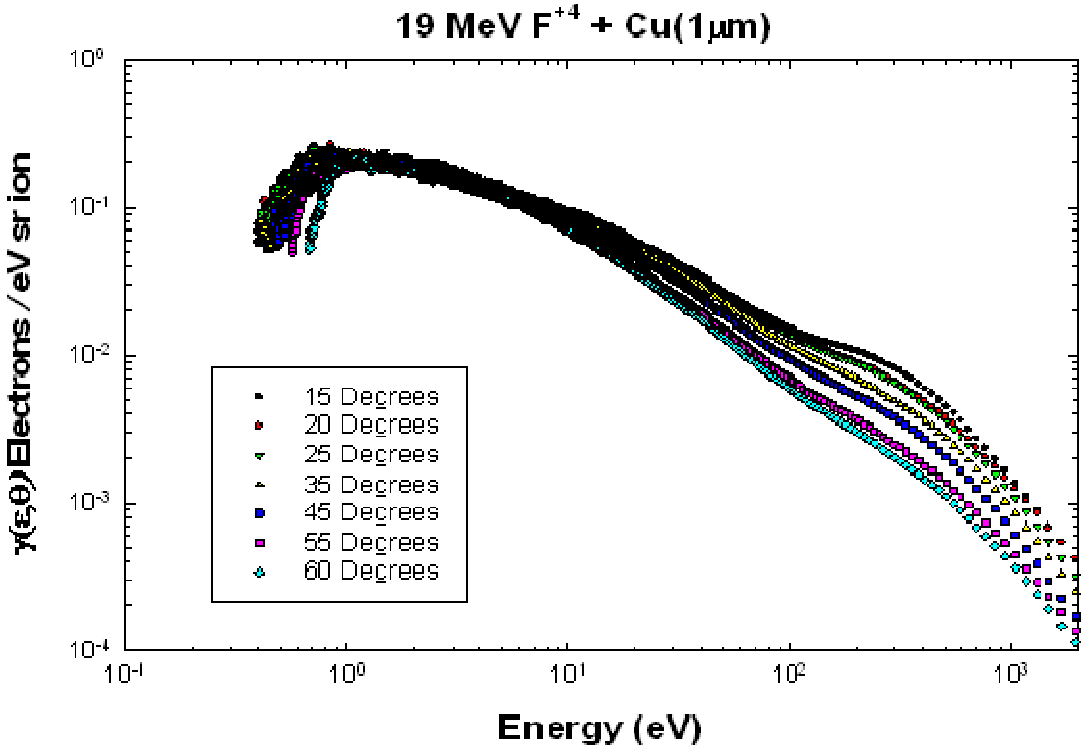

Figure 4.1. Electron emission yields for forward angles of 19 MeV F^{+4} on 1-μm thick copper foils.

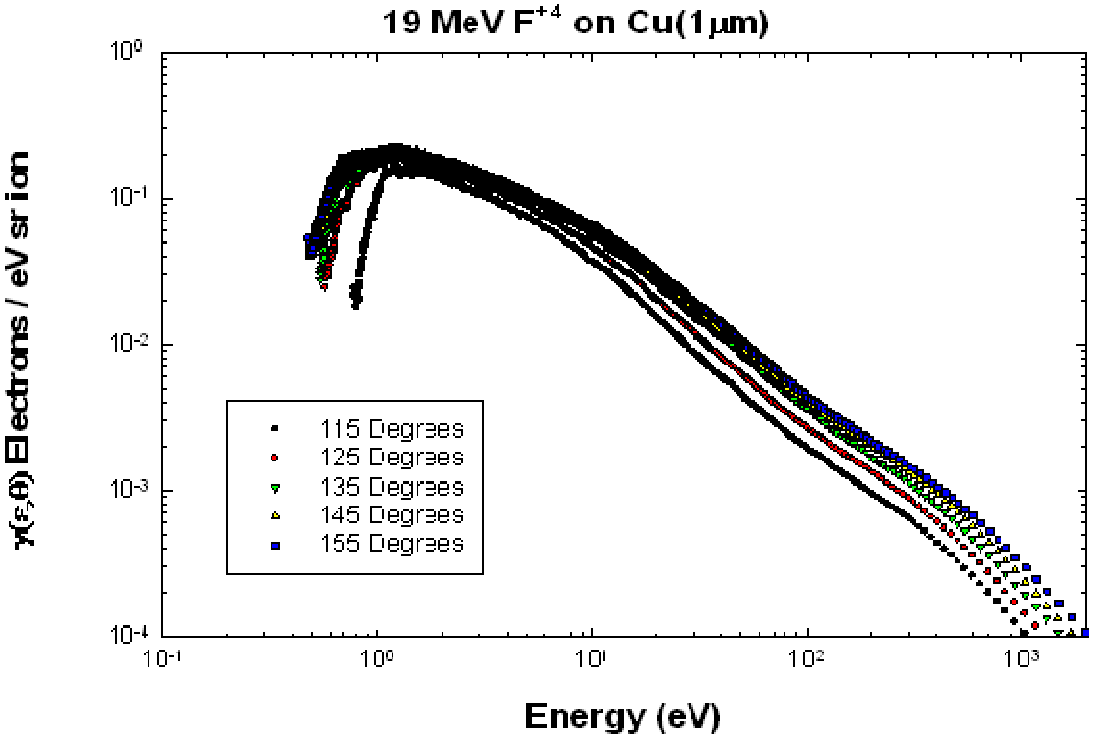

Figure 4.2. Electron emission yields for backward angles of 19 MeV F^{+4} on 1-μm thick copper foils.

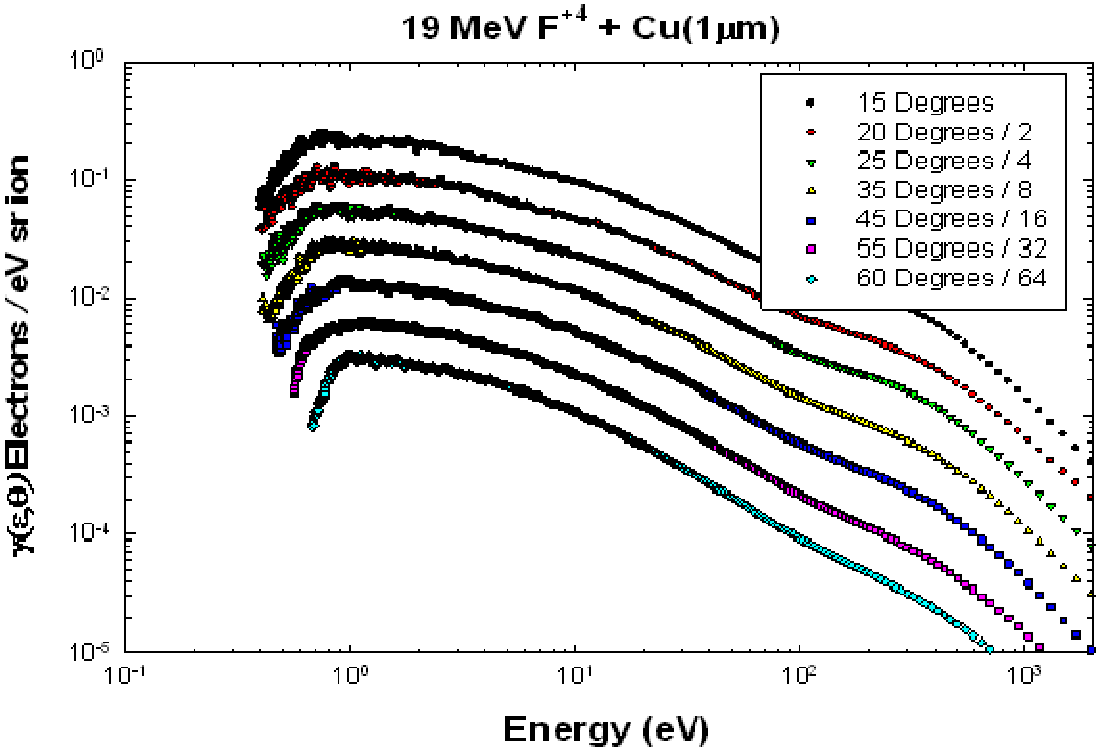

Figure 4.3. Electron emission yields for forward angles of 19 MeV F^{+4} on 1-μm thick copper foils scaled as stated to prevent overlap.

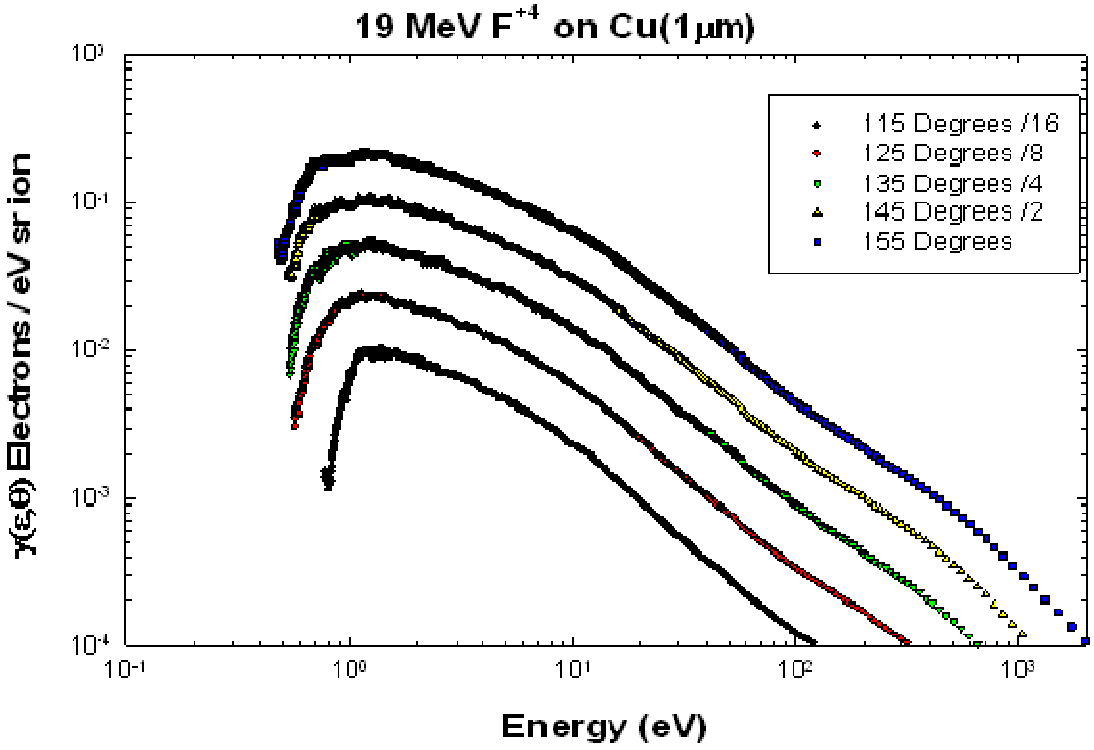

Figure 4.4. Electron emission yields for backward angles of 19 MeV F^{+4} on 1-μm thick copper foils scaled as stated to prevent overlap.

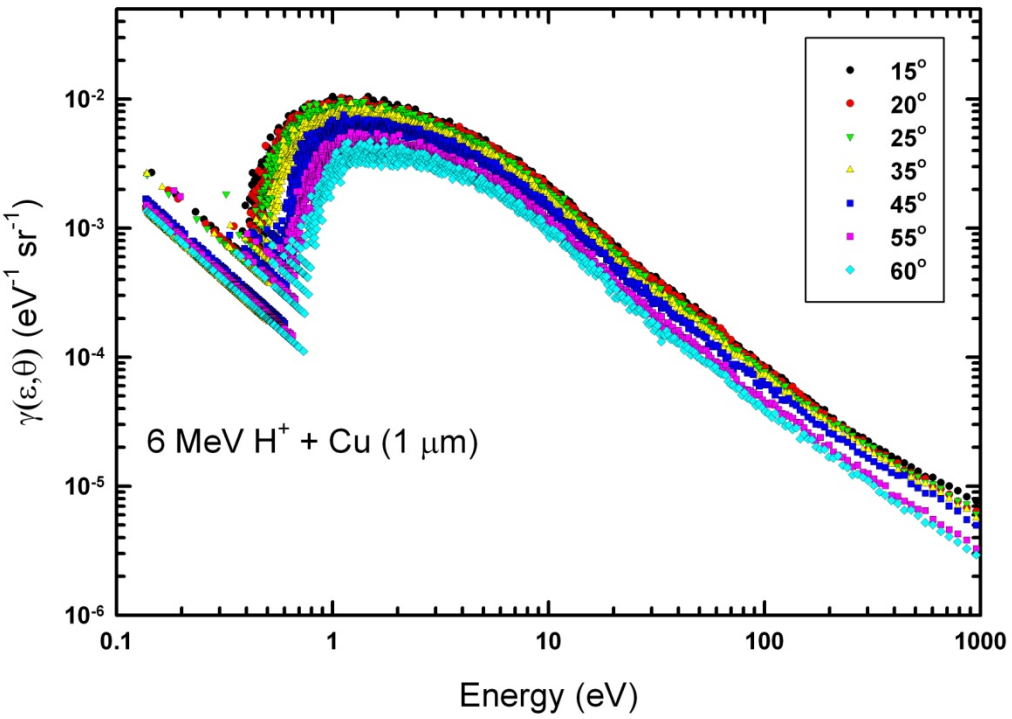

Figure 4.5. Electron emission yields for forward angles of 6 MeV H^+ on 1-μm thick copper foils.

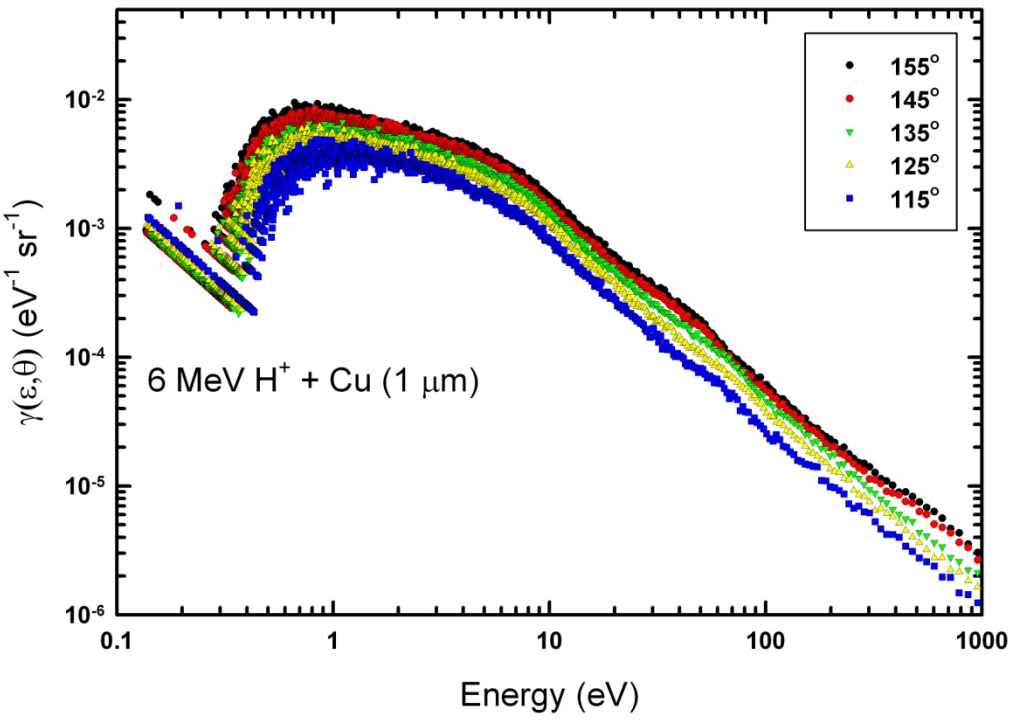

Figure 4.6. Electron emission yields for backward angles of 6 MeV H^+ on 1-μm thick copper foils.

4.3: Emission Spectra as a Function of ASW Thickness

Electron emission spectra as a function of exposure for 19 MeV F^{+4} impact on amorphous solid water frozen on a cryogenically cooled Cu substrate are shown in Figures 4.7 and 4.8. The measurements shown in the plots were taken at angles of 45° and 135º with respect to the incident beam for exposures between 0 L and 800 L in the forward direction and 0 L to 600 L in the backward direction. The figures show electron emission spectra for these exposure values with energies ranging from 0.8 eV to 1000 eV. Figures 4.9 and 4.10 show the exposure data scaled between 0.8 eV and 10 eV to emphasize the low-energy portion of the spectra. This energy range is where the systems energy resolution is optimal and the majority of emitted electrons are concentrated. The absolute scale of the ASW measurements were estimated by scaling the emission spectra from ASW films by the same amount as the Cu substrate. This approach is valid since no changes are made to the experimental system and the deposited water layer is thin. Finally, the data taken for the ASW target is estimated to have a statistical error of just under 20% based on deviations in yields from multiple measurements of the spectra.

The emission spectra are dominated by a low-energy peak ranging from approximately 1 to 10 eV. The intensity of this peak increases with increasing ASW film thickness until reaching approximately 600 L when it begins to decrease. The increase in the electron yield occurs more rapidly at lower exposure levels, the height of the low-energy peak from an exposure of 100L is 300% greater than the emission from bare Cu (0

L). As the exposure and thus thickness of ASW increases the rate of growth of the low-energy peak slows, growing by only approximately 10% between 100 L and 600 L. This effect can be seen clearly in the low energy yields shown in Figure 4.11. In the figure, yields are shown as a function of ASW thickness for a number of selected energies. It can be noted that at a thickness of approximately 200 L the yields become relatively independent with increasing ASW thickness. For this reason 200 L was chosen to be the exposure at which angular dependent yields would be measured as this represented a layer of amorphous solid water that is thick (40nm) in comparison to the range of secondary electrons ensuring that the observed electrons were emitted only from the ASW layer. Further, in choosing this thickness value it is important to recognize that as the exposure increases the cutoff energy shifts towards increasing emission energy. To minimize this effect the lowest thickness in the linear range, 200 L, was chosen. This shift towards higher cutoff energy can easily be seen in both the forward and backward spectra (Figures 4.9 and 4.10) where both the log scale and small energy range accentuate the change. Additionally, in both the forward and backward spectra a small but well defined peak can be observed that forms just beyond the threshold energy. While less intense and spread over a larger range in the forward direction the peak is very distinct in the 135º spectra. This peak is believed to be the result of target charging and increases in intensity with increasing exposure as would be expected with charging. What can be learned from these plots is that the spectral shapes of the measured data at low energies

are affected by target charging that is dependent on ASW thickness. These charging effects distort the measured data at 45º up to 2.0 eV for an ASW thickness of 800 L, and a minimum of approximately 0.85 eV for 200 L. Thus for an ASW thickness of 200 L electron yields are considered unreliable at or below the observed target charging structure. This means that at a thickness of 200 L in the forward direction there is a cutoff in reliable data between approximately 0.85 eV at 15º and 2.0 eV at 60º. Likewise, for the backward angles the cutoff spans from 1.75 eV at 115º to approximately 1.1 eV at 155º.

Finally, in attempting to understand the effect of target thickness on electron yields it must be pointed out that while Figure 4.11 indicates that electron yields are relatively stable for ASW thicknesses greater than approximately 100 L this does not necessarily mean that spectra of angular yields are identical. For example Figures 4.12 and 4.13 show electron emission yields for both 100 L and 200 L exposures at angles of 45º and 135º respectively. The spectra presented in Figures 4.12 and 4.13 are nearly identical as they are for most of the angles studied. However, at the most extreme angles such as 15º and 155º shown in Figures 4.14 and 4.15 below 2 eV the lowest energy portion of the spectra deviate from one another by a factor of approximately two. This is a factor that must be considered in any application of the presented results.

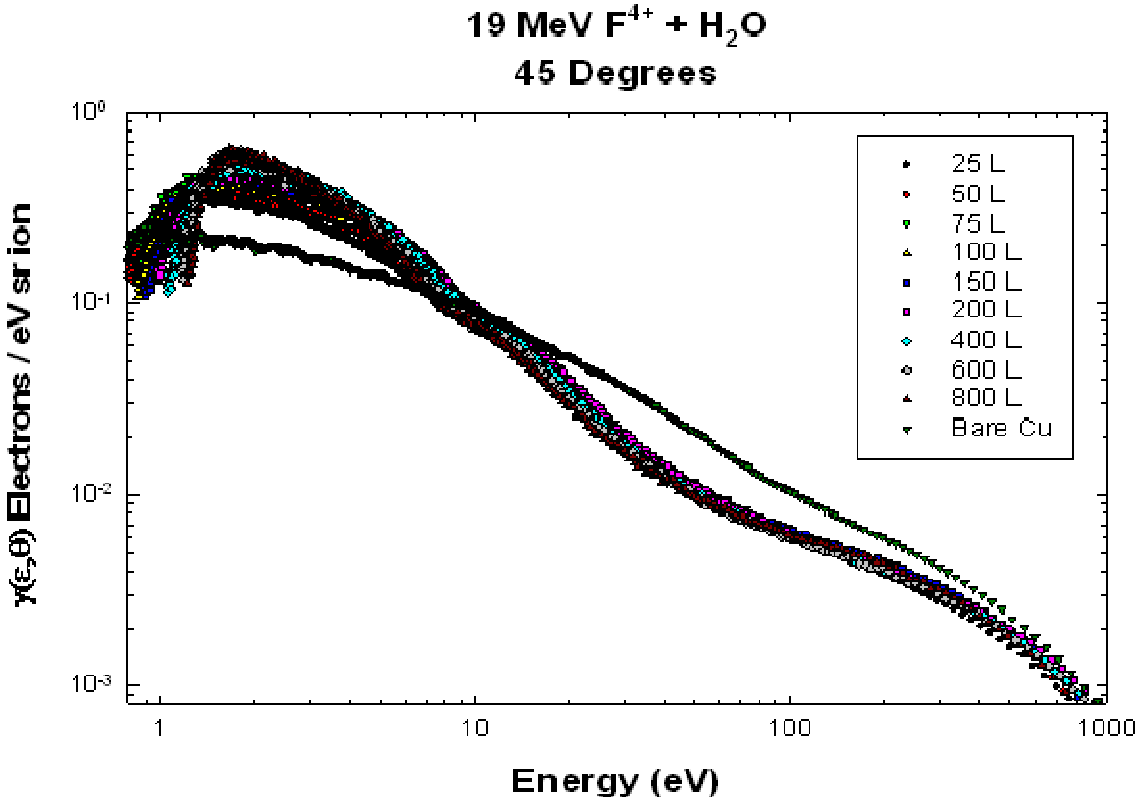

Figure 4.7. Electron emission yields at 45º for 19 MeV F^{+4} on ASW target with thickness between 0 L and 800 L.

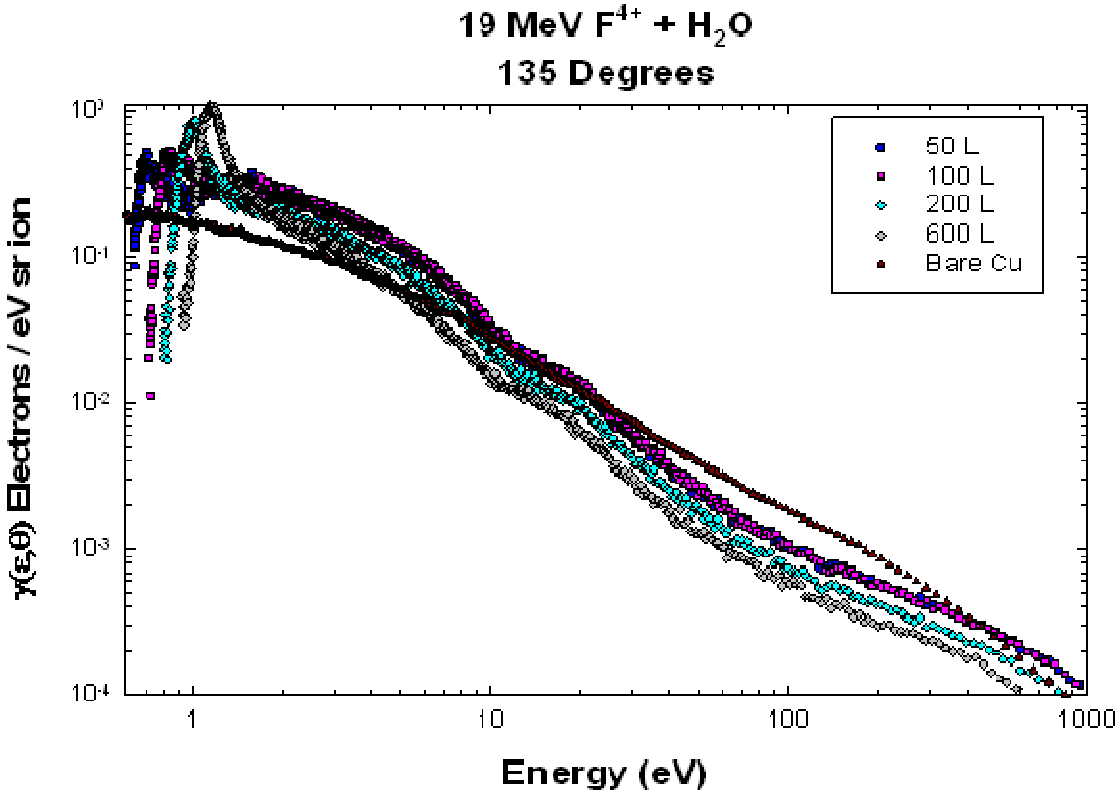

Figure 4.8. Electron emission yields at 135º for 19 MeV F^{+4} on ASW target with thickness between 0 L and 600 L.

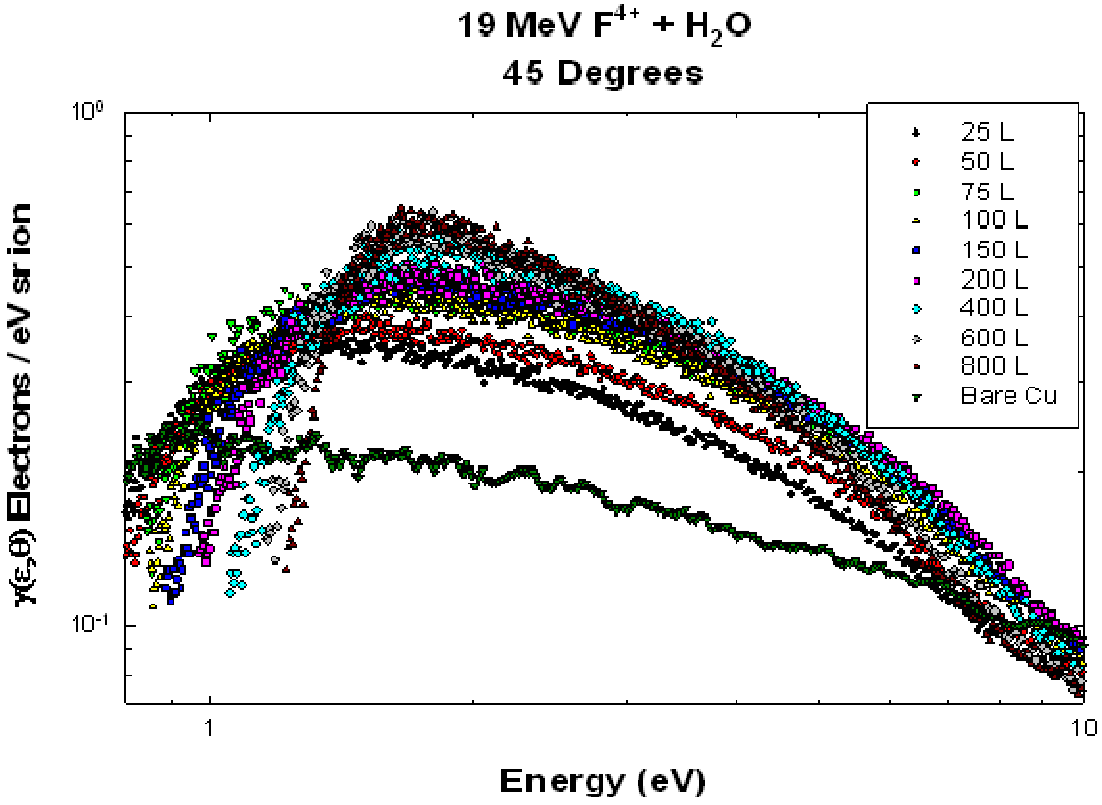

Figure 4.9. Electron emission yields at 45º for 19 MeV F^{+4} on ASW target with thickness between 0 L and 800 L. Plot is scaled to emphasize low energy region.

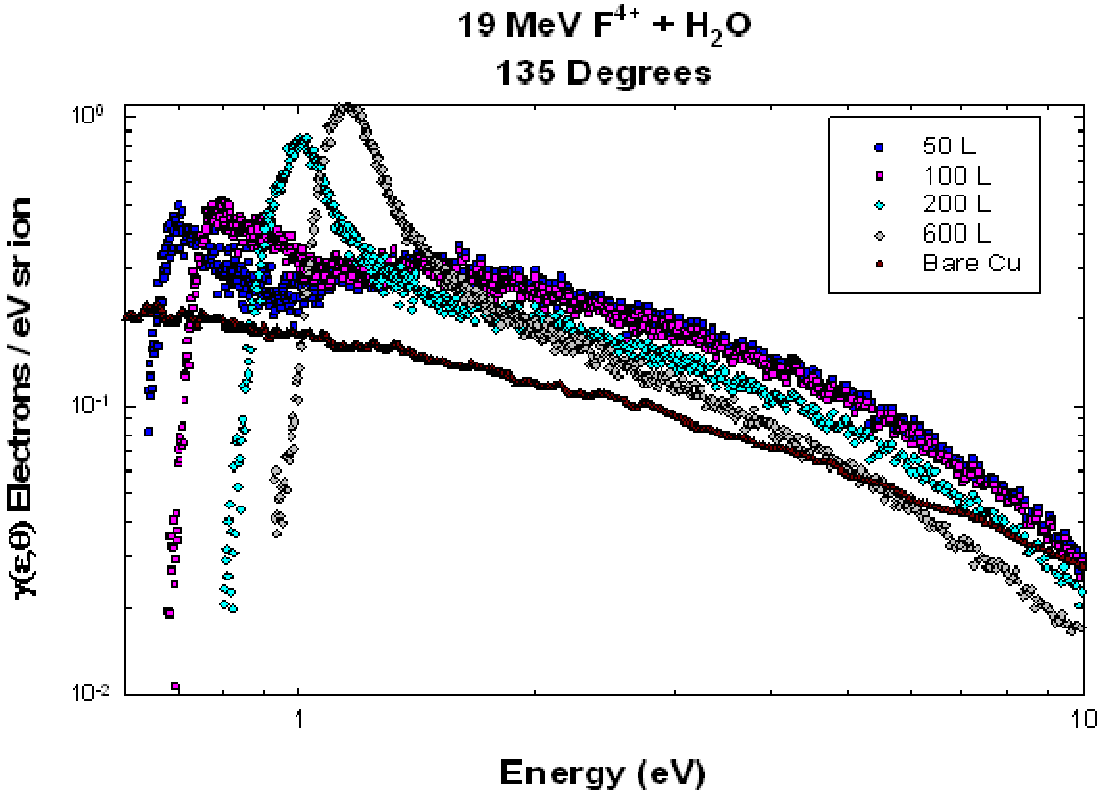

Figure 4.10. Electron emission yields at 135° for 19 MeV F^{+4} on ASW target with thickness between 0 L and 800 L. Plot is scaled to emphasize low energy region.

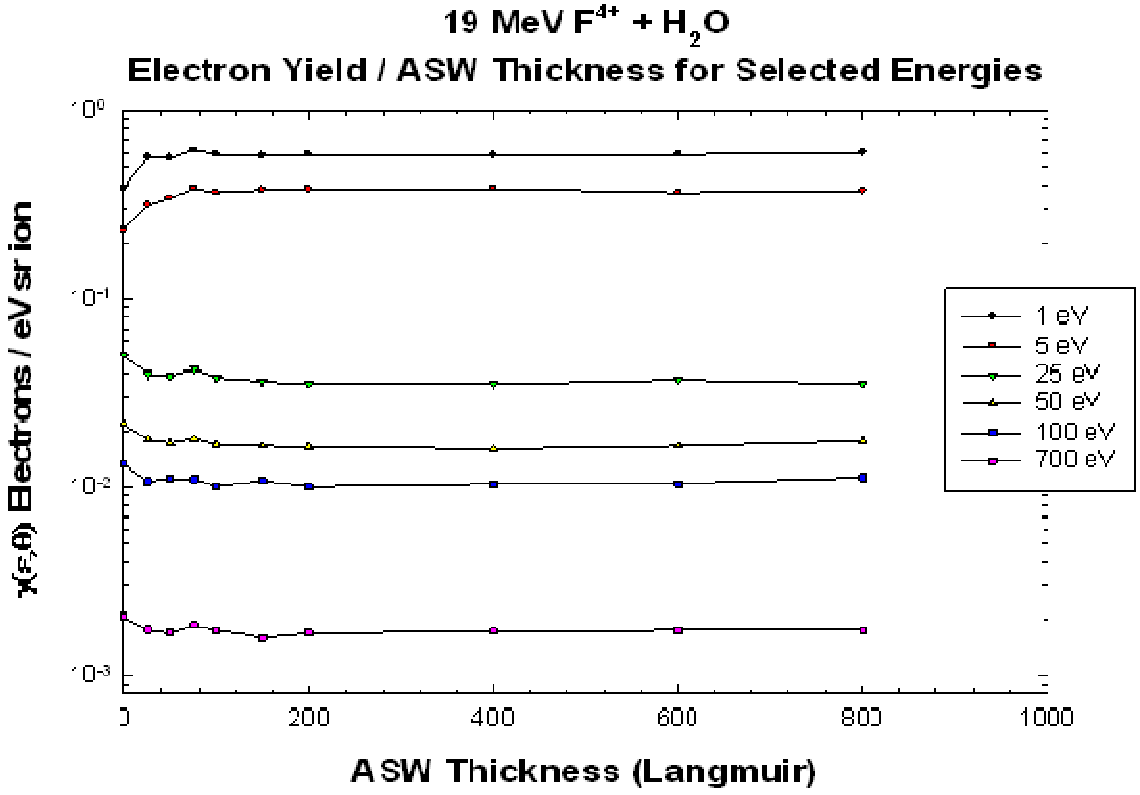

Figure 4.11. Electron emission yields versus amorphous solid water thickness for selected energies.

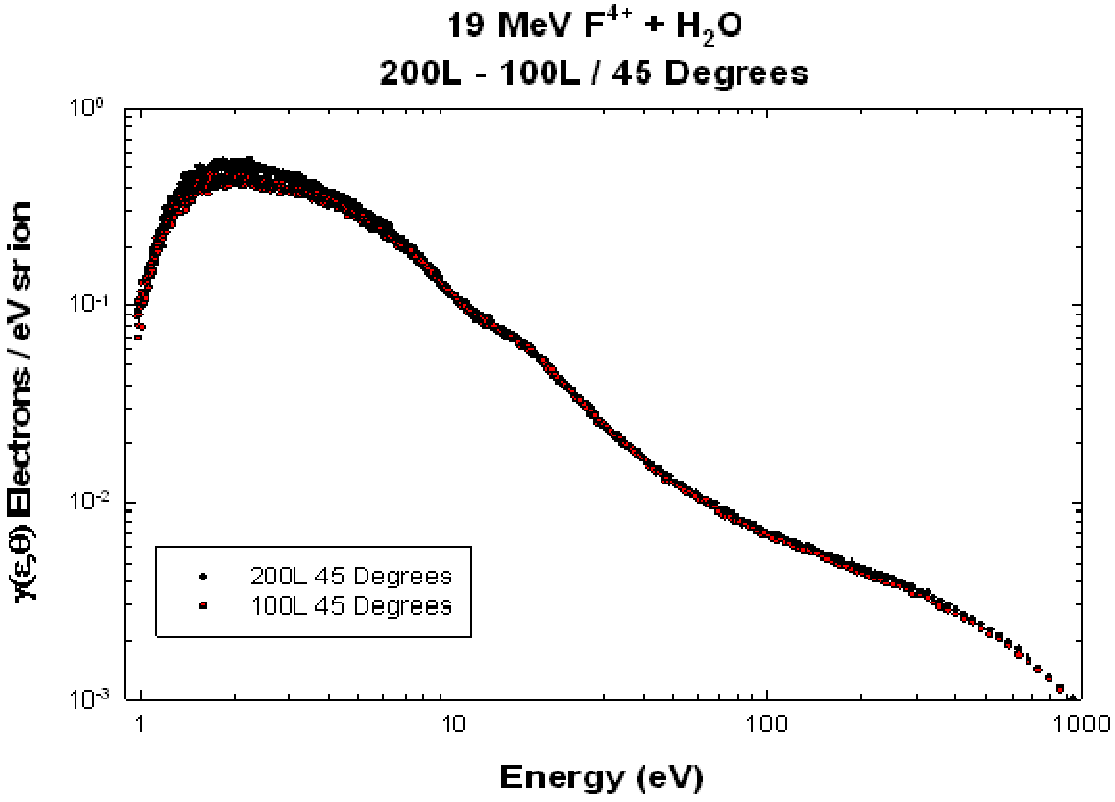

Figure 4.12. Electron emission yields at 45º for 19 MeV F^{+4} on ASW target with thickness of 100 L and 200 L. Note that at this angle, in the middle of the forward angular range, the two spectra are nearly identical.

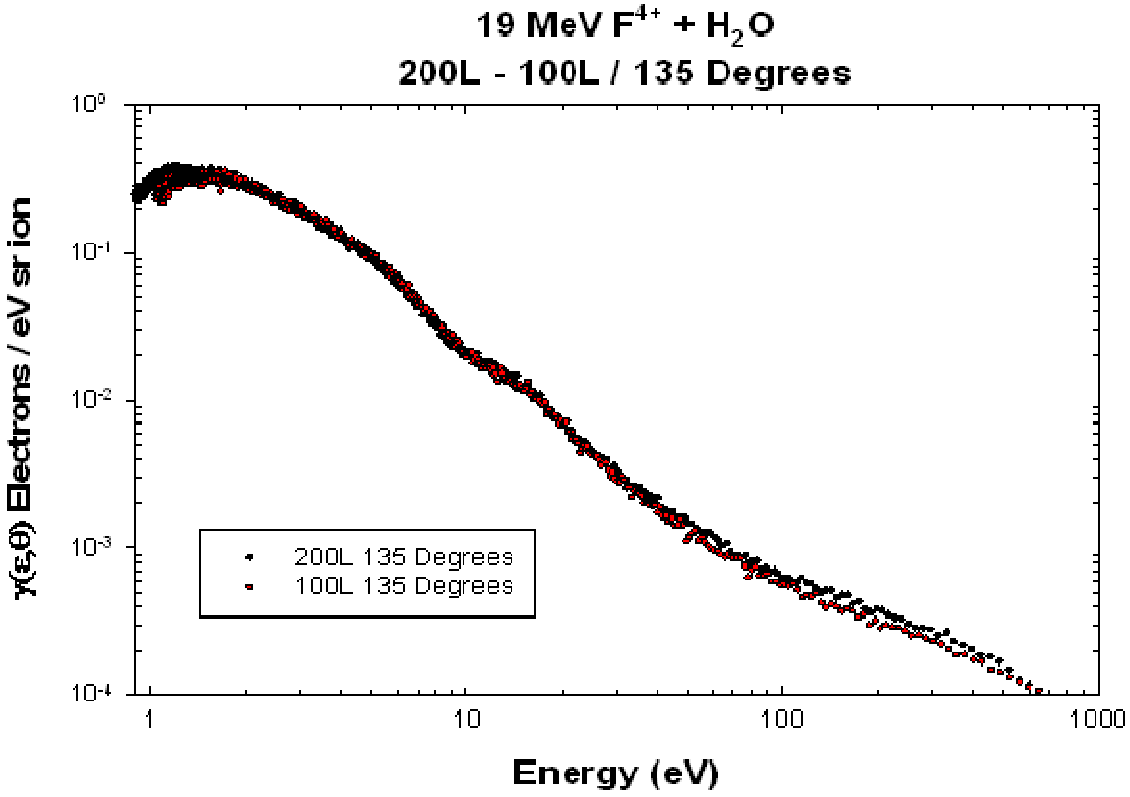

Figure 4.13. Electron emission yields at 135º for 19 MeV F^{+4} on ASW target with thickness of 100 L and 200 L. Note that at this angle, in the middle of the backward angular range, the two spectra are nearly identical.

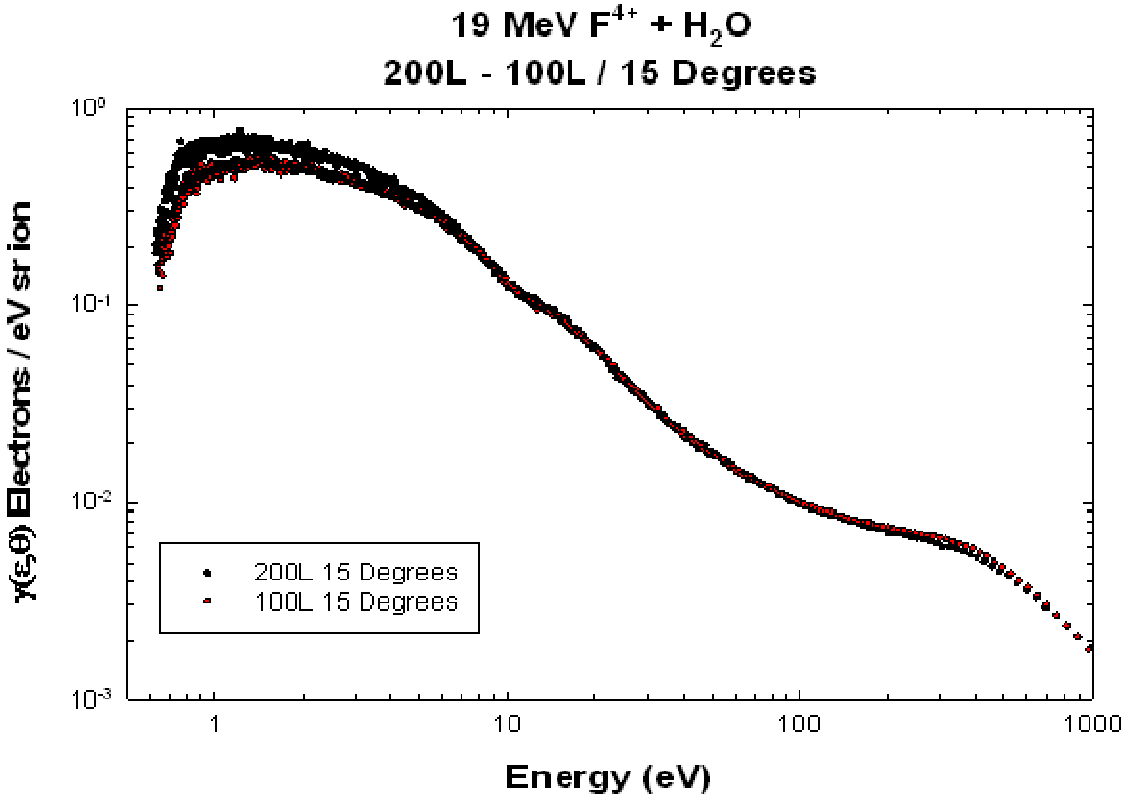

Figure 4.14. Electron emission yields at 15º for 19 MeV F^{+4} on ASW target with thickness of 100 L and 200 L. Note that at this angle, at the extreme of the forward angular range, the two spectra deviate by a factor of approximately 2 below 2 eV.

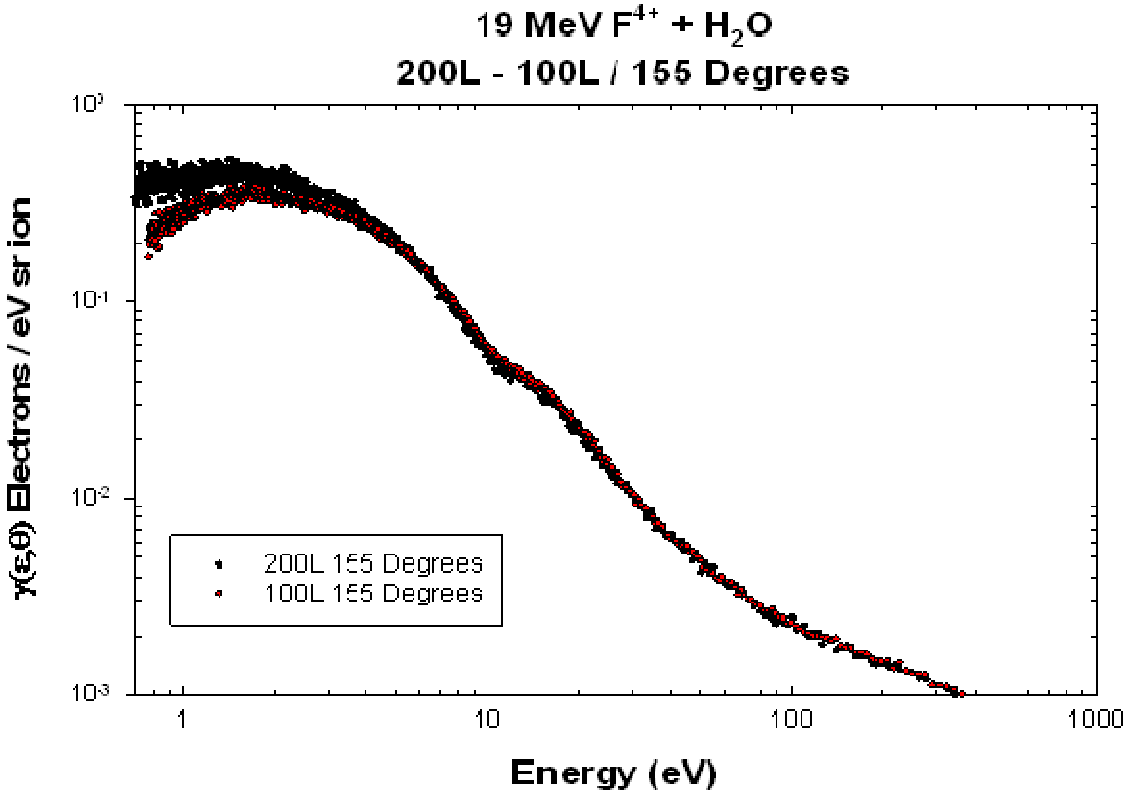

Figure 4.15. Electron emission yields at 155° for 19 MeV F^{+4} on ASW target with thickness of 100 L and 200 L. Note that at this angle, at the extreme of the bakcward angular range, the two spectra deviate by a factor of approximately 2 below 2 eV.

4.4: Electron Yields from Amorphous Solid Water

Double-differential electron emission yields for 19 MeV F^{+4} impact on amorphous solid water frozen on a cryogenically cooled 1-μm Cu foil are presented in Figures 4.16, 4.17, 4.19, and 4.20. Figure 4.16 shows electron emission yields for the forward angles, and Figure 4.17 shows the same yields scaled to allow better viewing by eliminating overlap of spectra. Figure 4.19 shows yields for the backward angles, and again Figure 4.20 shows the same data scaled for easier interpretation. As described in section 4.3 these data sets contained low energy artifacts from target charging that distorted the spectra at low energies making measured yields in those energy regions unreliable. This charging effect is angularly dependent and affects the forward data from 0.85 eV to 2.0 eV over the angular range of 15º to 60º, and affects the backward data from 1.75 eV to 1.1 eV over the range of 115º to 155º. For this reason the artifact has been removed and the data cutoff below these energies in the plots presented. In addition, caution should be used in the application of the 115º spectrum presented. Measurements taken at this angle did not reproduce well from run to run. This is believed to have been caused by interference from the placement of the target holder. However, one run did produce a spectrum with the shape and features expected, and this data is presented here for the purposes of completing illustration. Figures 4.18 and 4.21 show forward and backward electron emission yields for 6 MeV H^{+} impact on amorphous solid water frozen on a cryogenically cooled 1-μm Cu foil for the purposes of comparison. All of the

measurements were made on an ASW target with thickness equal to 200 L exposure. Again, this exposure was chosen because it is close to the maximum in the yield of electrons, and represents a thickness of ASW sufficient to exclude electrons emitted from the Cu foil. The absolute scale of the measurements was estimated as previously described in section 4.3 for the amorphous solid water thickness dependence measurements. In general, the spectra exhibit the same overall trends that are seen in the bare Cu foil data described in section 4.2. Finally, for the purposes of thorough exposition Figures 4.22 through 4.33 show each spectrum for ASW electron emission along with the bare Cu emission spectrum at the corresponding angle.

Figures 4.16 and 4.17 show the electron emission spectra for the ASW target in the forward direction. The dominating low-energy peak is located at approximately 0.9 - 1.0 eV on the 15° spectrum. Like the foil data in section 4.2, the position of the peak shifts to higher energies at larger emission angles. The peak is located at approximately 4 eV on the 60° emission spectrum. The height of the low-energy peak drops by approximately 75% between the 15° and 60° spectra. This trend is observed throughout the range of the spectra. The yield of electrons drops several orders of magnitude over the range of the plots. However, beyond 100 eV the bulge in the data that corresponds to the binary encounter peak and convoy electrons seen in the bare Cu spectra is evident here as well.

In comparison to the 6 MeV H^+ data in Figure 4.18 the spectra are very similar and share the same general shape. The yields from the 6 MeV H^+ data are nearly an order of magnitude lower than that of the 19 MeV F^{+4} spectra. Again, as was seen in the bare Cu data, beyond 100 eV the two sets differ in that the 6 MeV H^+ data does not contain the bulge in emission yield from the binary encounter and convoy electrons. However, what both data sets share is a peak in the emission spectra located at approximately 13 - 14 eV that was previously observed by R.A McLawhorn [19] in the 6 MeV H^+ data.

In the 19 MeV F^{+4} spectra at all emission angles there is a broad and poorly defined peak that begins around 10 eV and stretches to approximately 16 eV and seems to be centered around 13-14 eV. This peak is not well defined most likely due to a relative increase in outer shell electrons from ionization obscuring the structure. This increase in outer shell ionization is expected for fluorine ions as they are highly charged and moving more slowly than the 6MeV protons thus increasing the probability of ionization. Although poorly defined the presence of this structure in the 19 MeV F^{+4} data verifies that the structure is most likely the auto-ionization peak from H_2O reported by Wilson [5]. This structure can now be shown to appear independent of both emission angle and now projectile species.

The electron emission spectra in the backward direction are shown in Figures 4.19 and 4.20. The spectra show the same trends and features as the spectra in the forward direction. The low-energy peak is located at approximately 1 eV on the 155° spectrum,

closely matching that of the 15° spectrum. The yield of electrons decreases with increasing emission angle. This decrease is more pronounced on the 125° and 115° spectra. Again, these trends are also seen for 6 MeV H^+ data in the backward direction in Figure 4.21 In the backward data sets for both ions the peak on the emission spectra at approximately 13 - 14 eV that is believed to be the result of auto-ionization by H_2O is again seen at all emission angles.

Figures 4.22 through 4.33 show each angular emission spectrum from ASW in comparison with the corresponding bare Cu spectrum. In each plot it can be noted that the emission spectrum from 19 MeV F^{+4} are much greater than the copper target for energies less than 10 eV. Beyond 10 eV the yields from 19 MeV F^{+4} emission dip below that of bare copper.

The angular distributions of electrons $\gamma(\theta)$ emitted from ASW foils are shown in Figure 4.34. The angular distributions were studied to determine the general trend of the spatial distribution of electrons emitted from the surface of the target. These single-differential electron emission yields $\gamma(\theta)$ were obtained by numerical integration of the double-differential electron emission yields $\gamma(\varepsilon,\theta)$ over the electron energy ε and are plotted as a function of the $\cos(\theta)$. Although not perfect, the trend-lines used to guide the eye indicate that the data are primarily linear with deviations attributed mainly to low energy electrons that are strongly influenced by surface properties such as charging phenomena [62,63].

Figure 4.35 shows the single-differential electron yields for ASW that were obtained by integrating the double-differential yields by emission angle. The broad low-energy peak is still evident along with the emission bulge centered around the equal velocity criteria at 545 eV. Figure 4.36 shows the same single-differential yields plotted linearly as is common in surface science articles. These data were then integrated again to obtain Total Yields in both the forward and backward directions. The Total Yields were determined to be $\gamma_f = 21 \pm 4$ and $\gamma_b = 8 \pm 2$ electrons/ion.

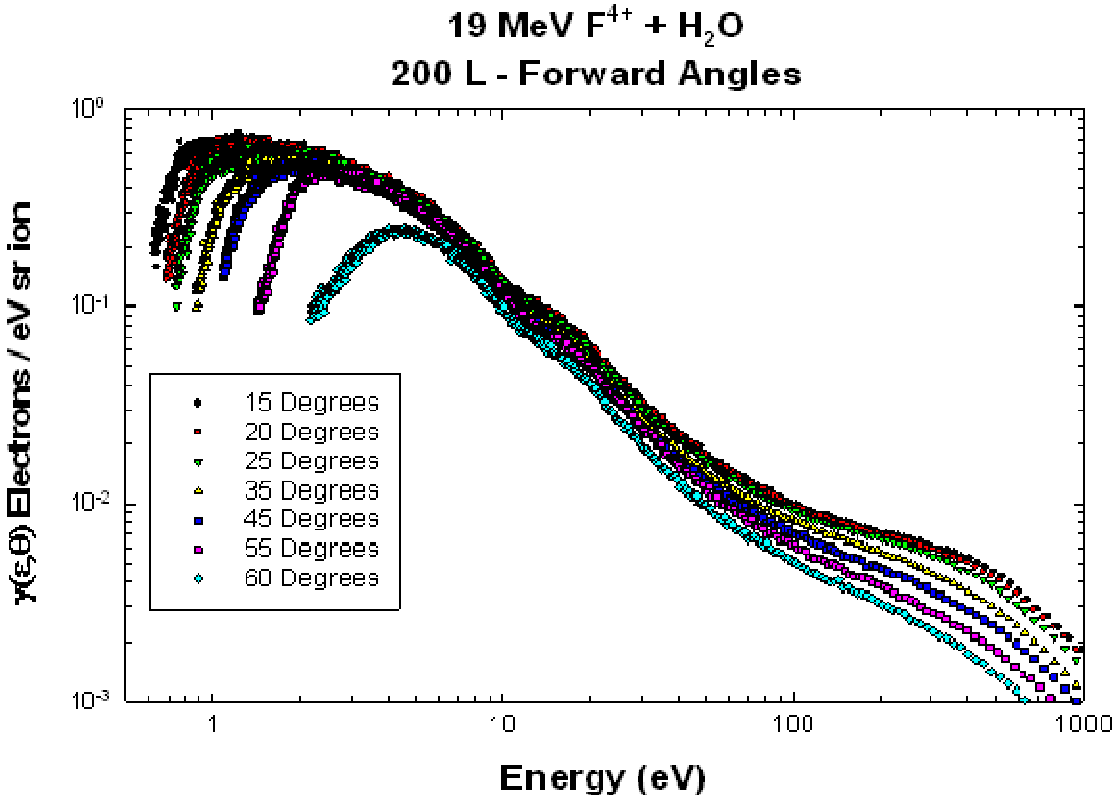

Figure 4.16. Electron emission yields for forward angles of 19 MeV F^{+4} on 200 L thick ASW target.

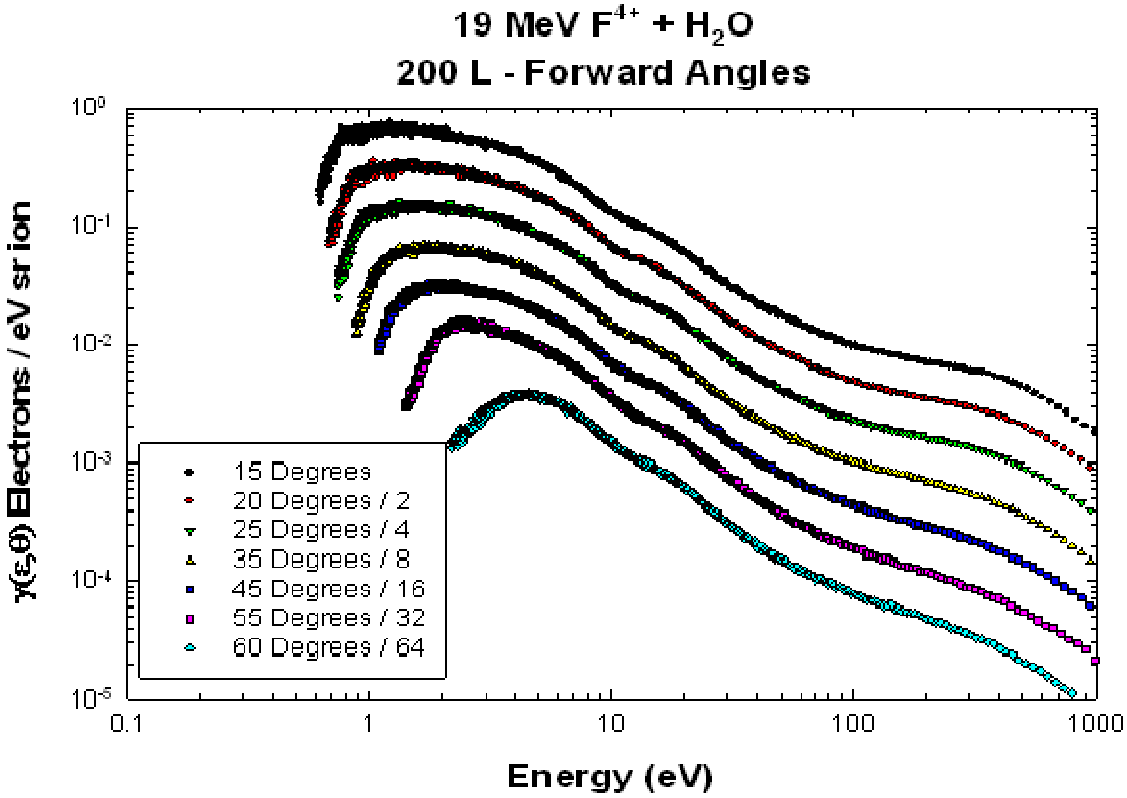

Figure 4.17. Electron emission yields for forward angles of 19 MeV F^{+4} on 200 L thick ASW target with spectra scaled as indicated to avoid overlap.

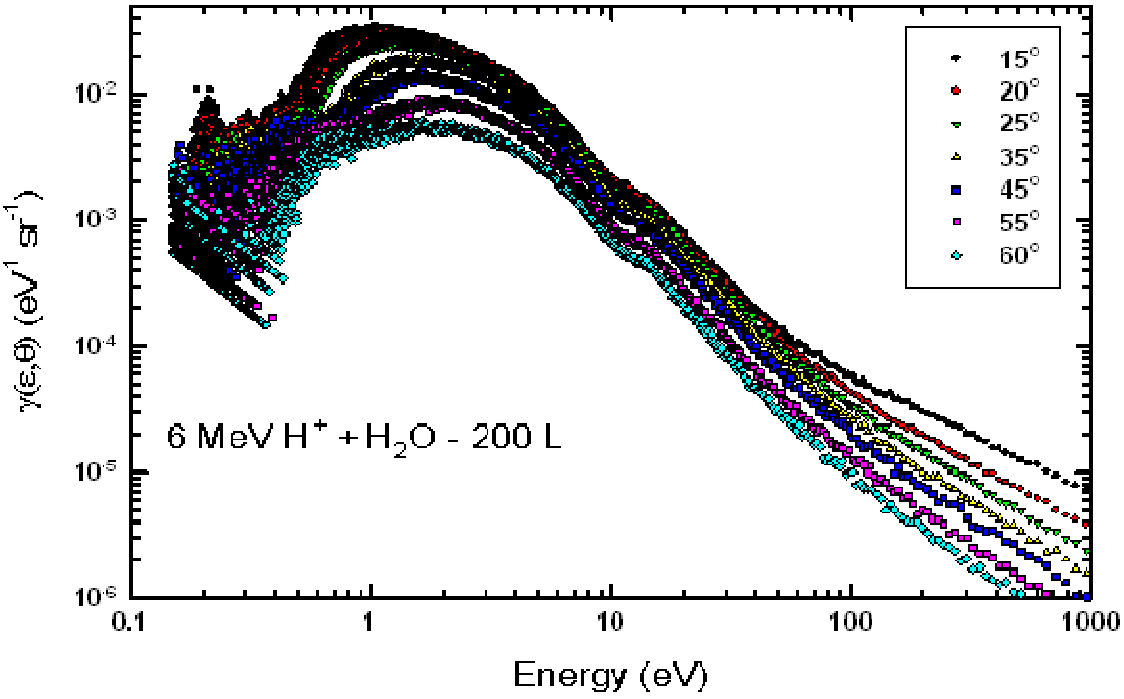

Figure 4.18. Electron emission yields for forward angles of 6 MeV H^+ on 200 L thick ASW target.

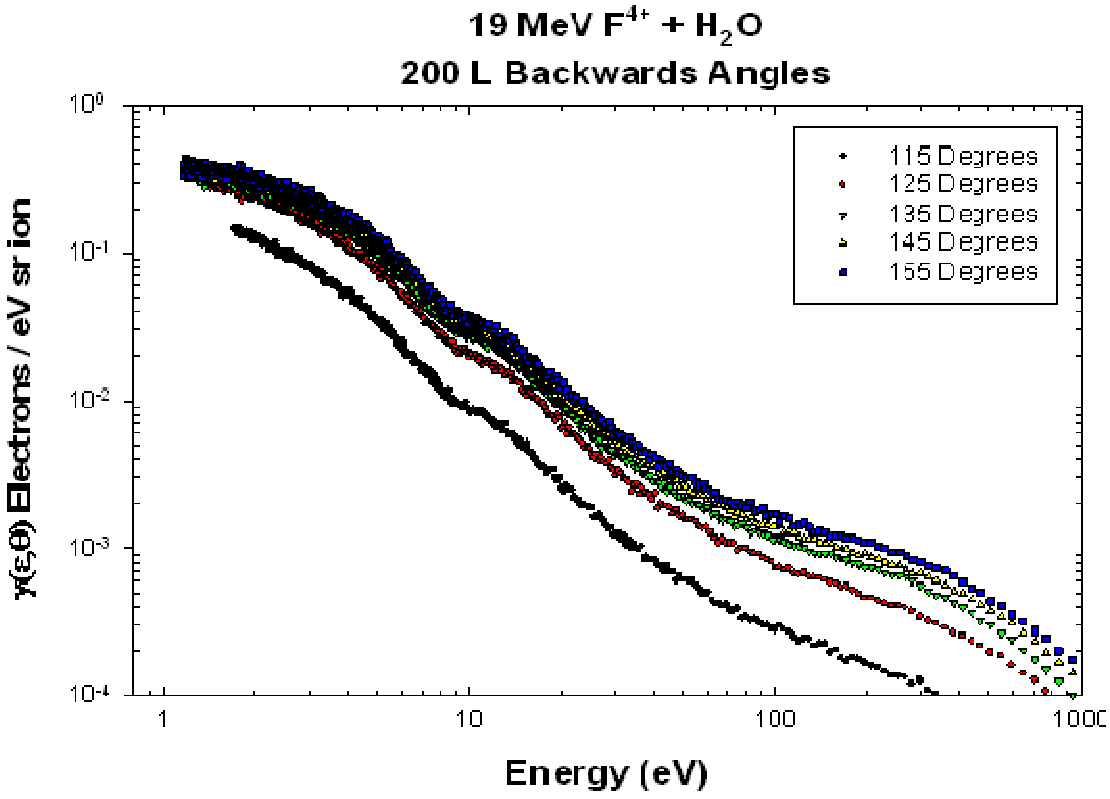

Figure 4.19. Electron emission yields for backward angles of 19 MeV F^{+4} on 200 L thick ASW target.

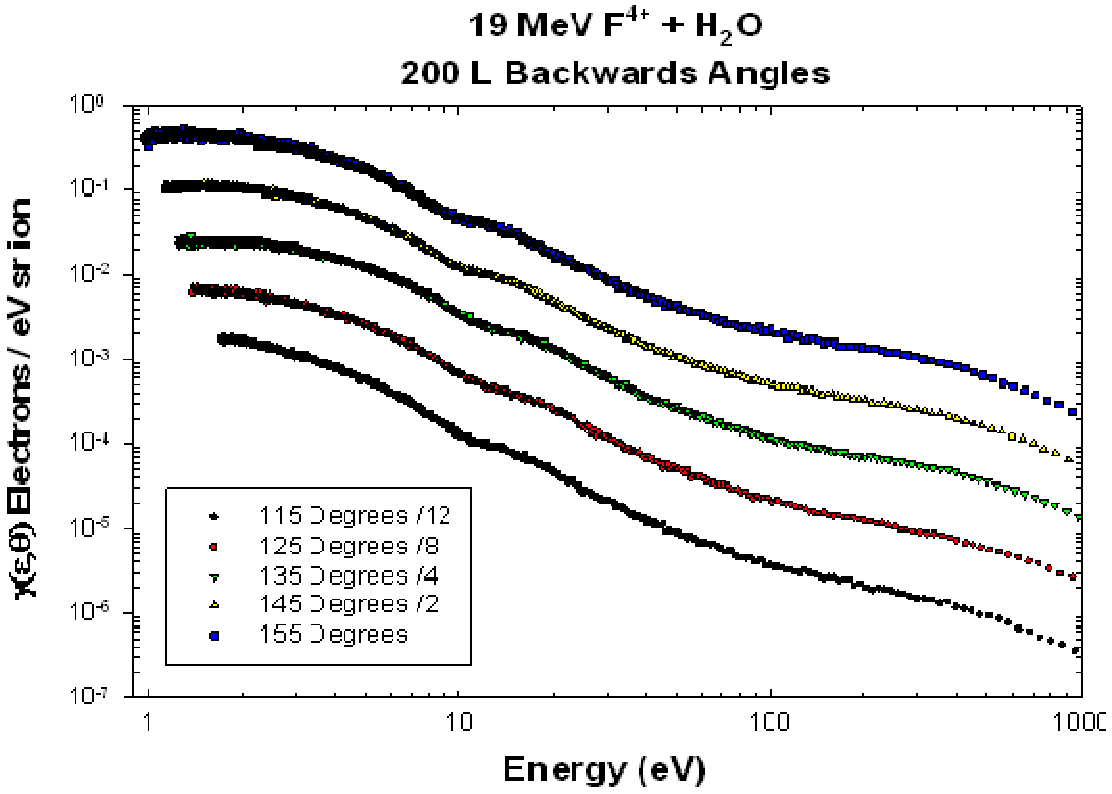

Figure 4.20. Electron emission yields for backward angles of 19 MeV F^{+4} on 200 L thick ASW target with spectra scaled as indicated to avoid overlap.

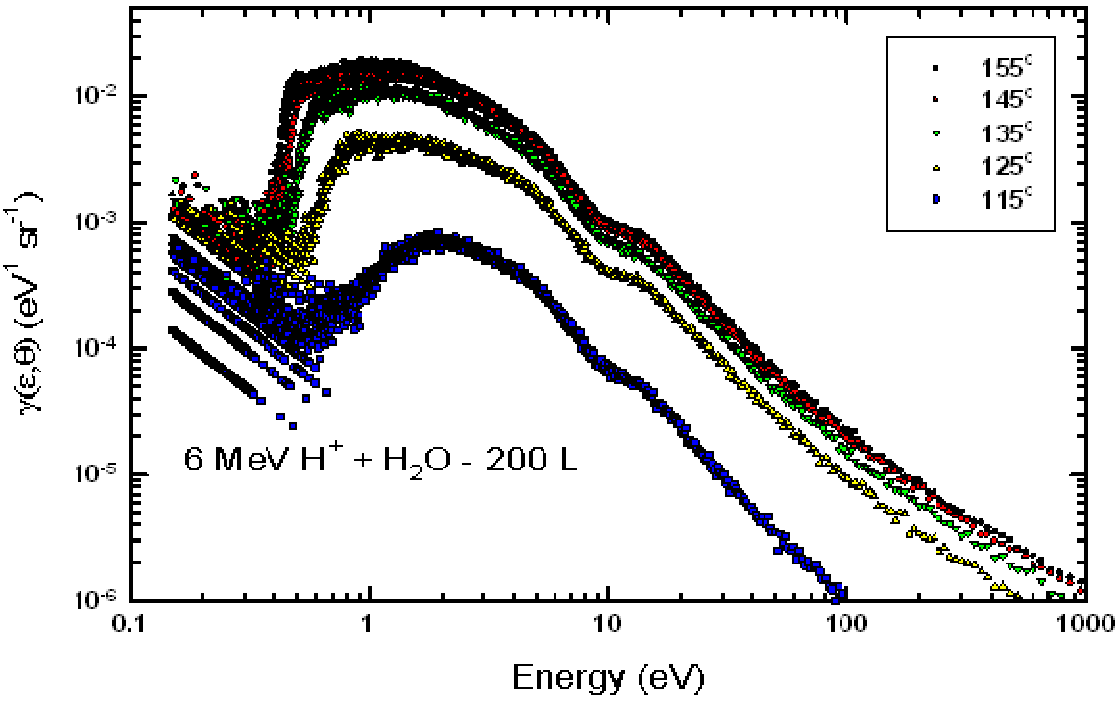

Figure 4.21. Electron emission yields for backward angles of 6 MeV H^+ on 200 L thick ASW target.

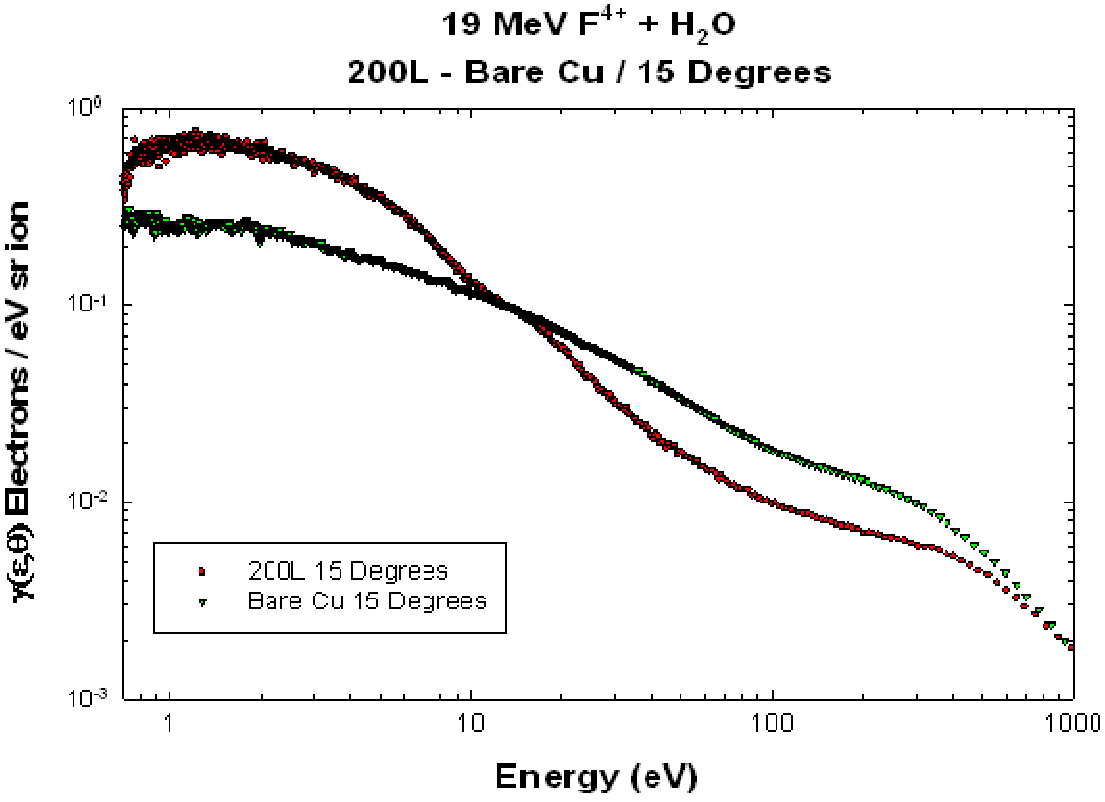

Figure 4.22. Electron emission yields at 15º for 19 MeV F^{+4} on 200 L thick ASW target along with emission yield from bare Cu foil at 15º.

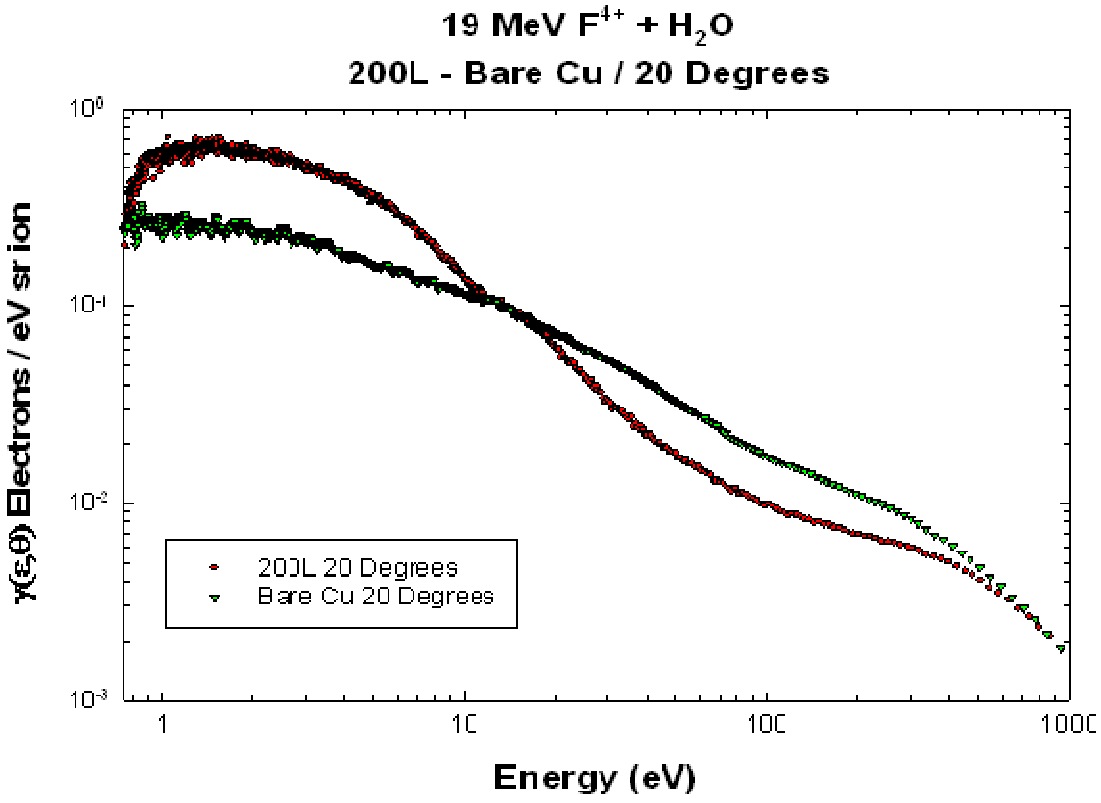

Figure 4.23. Electron emission yields at 20º for 19 MeV F^{+4} on 200 L thick ASW target along with emission yield from bare Cu foil at 20º.

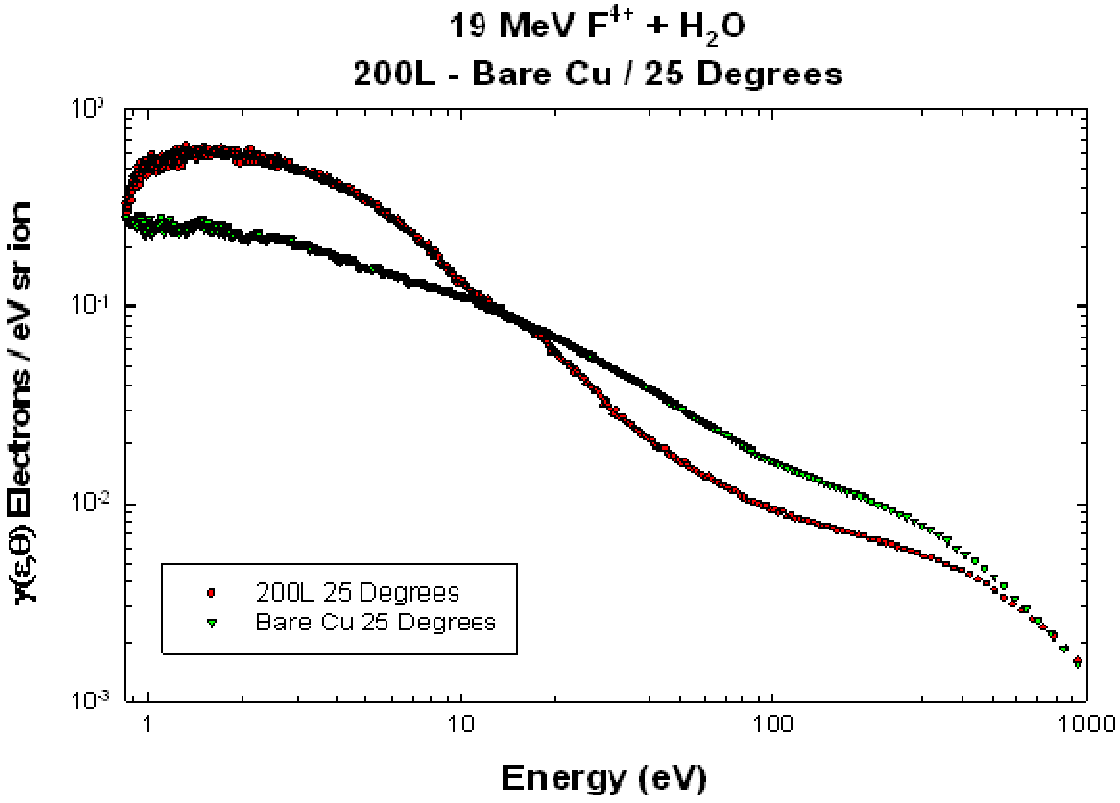

Figure 4.24. Electron emission yields at 25º for 19 MeV F^{+4} on 200 L thick ASW target along with emission yield from bare Cu foil at 25º.

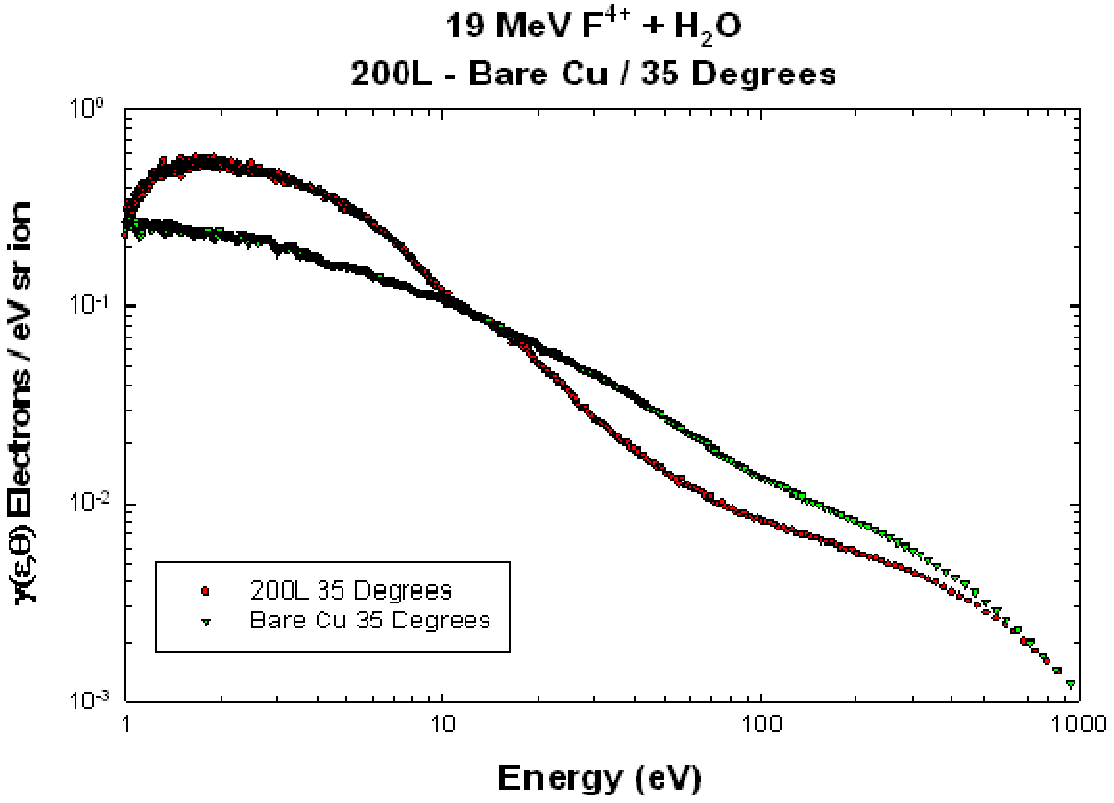

Figure 4.25. Electron emission yields at 35º for 19 MeV F^{+4} on 200 L thick ASW target along with emission yield from bare Cu foil at 35º.

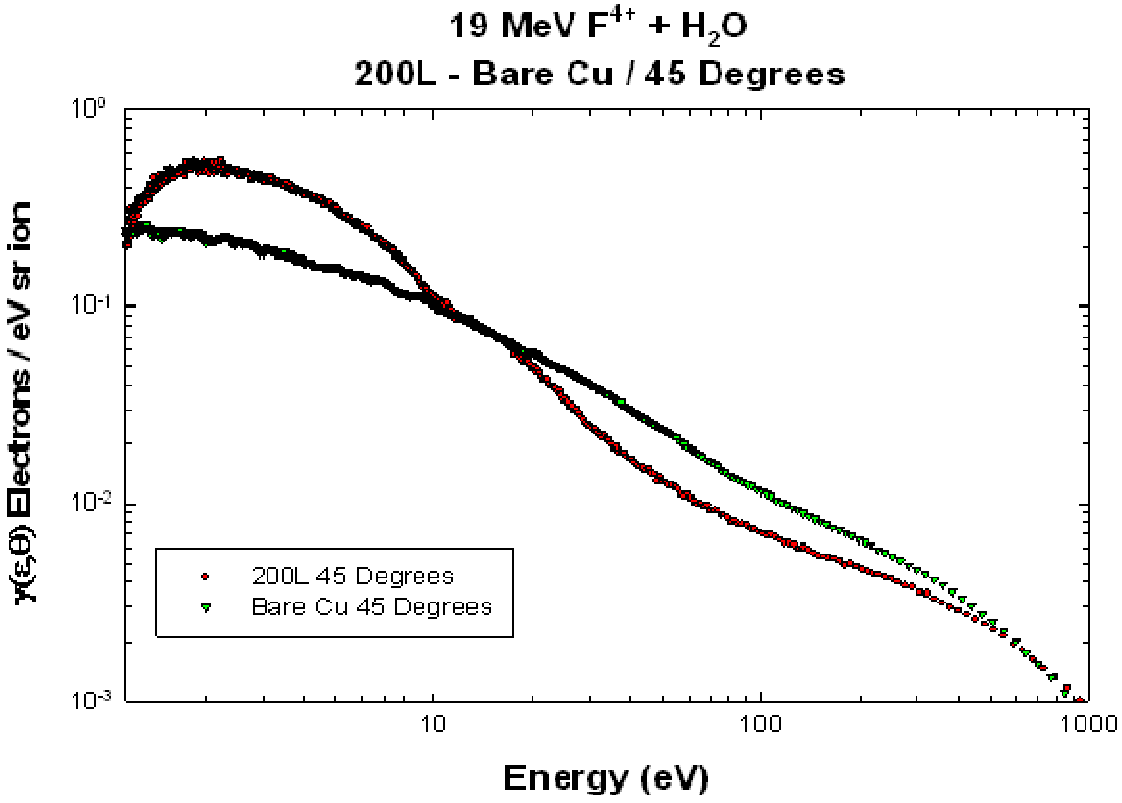

Figure 4.26. Electron emission yields at 45º for 19 MeV F^{+4} on 200 L thick ASW target along with emission yield from bare Cu foil at 45º.

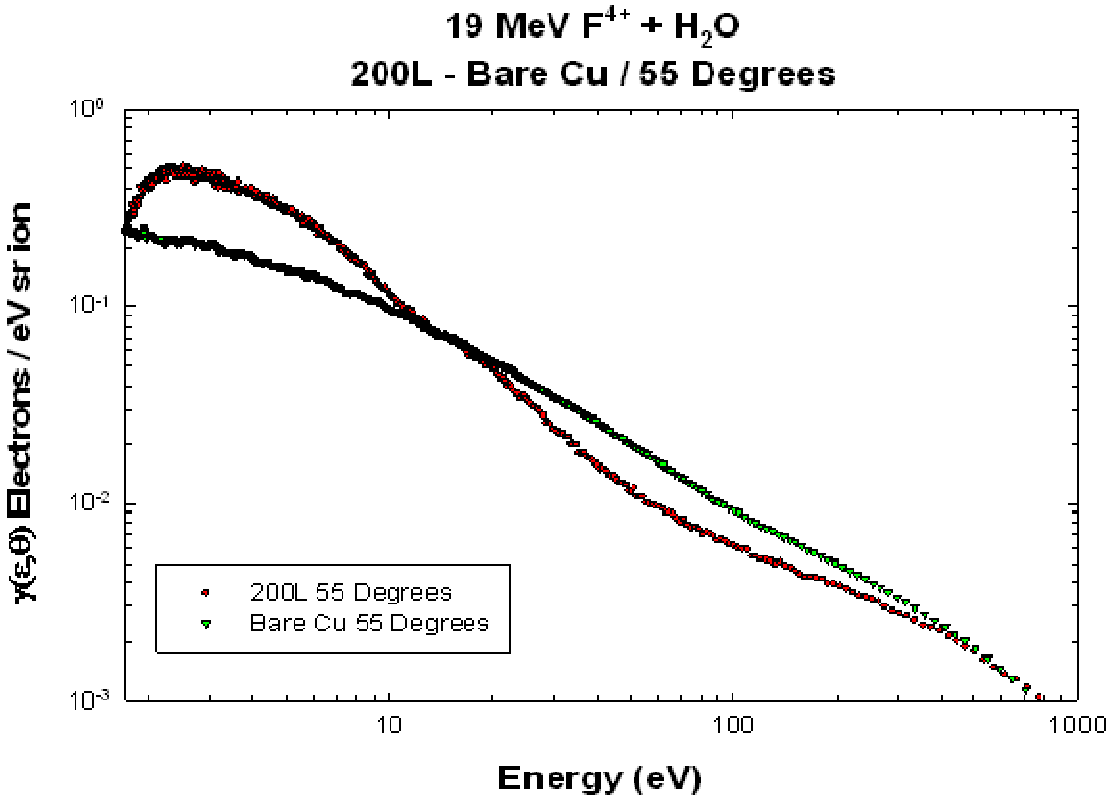

Figure 4.27. Electron emission yields at 55º for 19 MeV F^{+4} on 200 L thick ASW target along with emission yield from bare Cu foil at 55º.

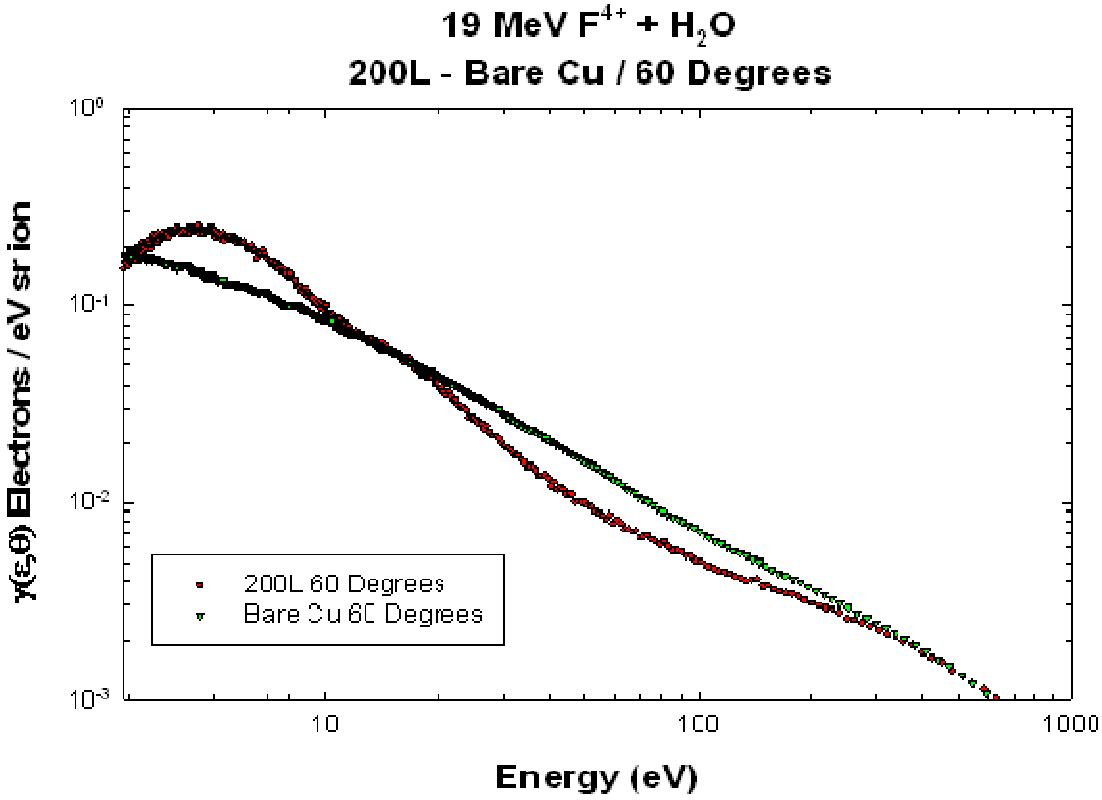

Figure 4.28. Electron emission yields at 60º for 19 MeV F^{+4} on 200 L thick ASW target along with emission yield from bare Cu foil at 60º.

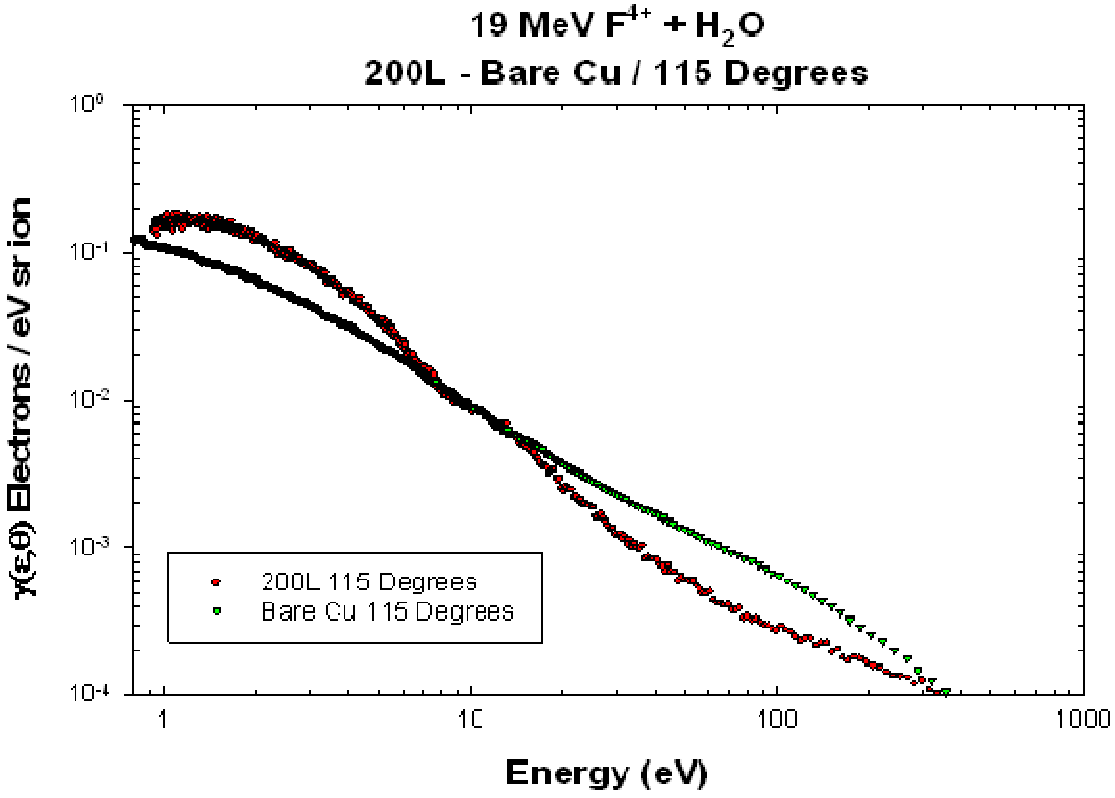

Figure 4.29. Electron emission yields at 115º for 19 MeV F^{+4} on 200 L thick ASW target along with emission yield from bare Cu foil at 115º.

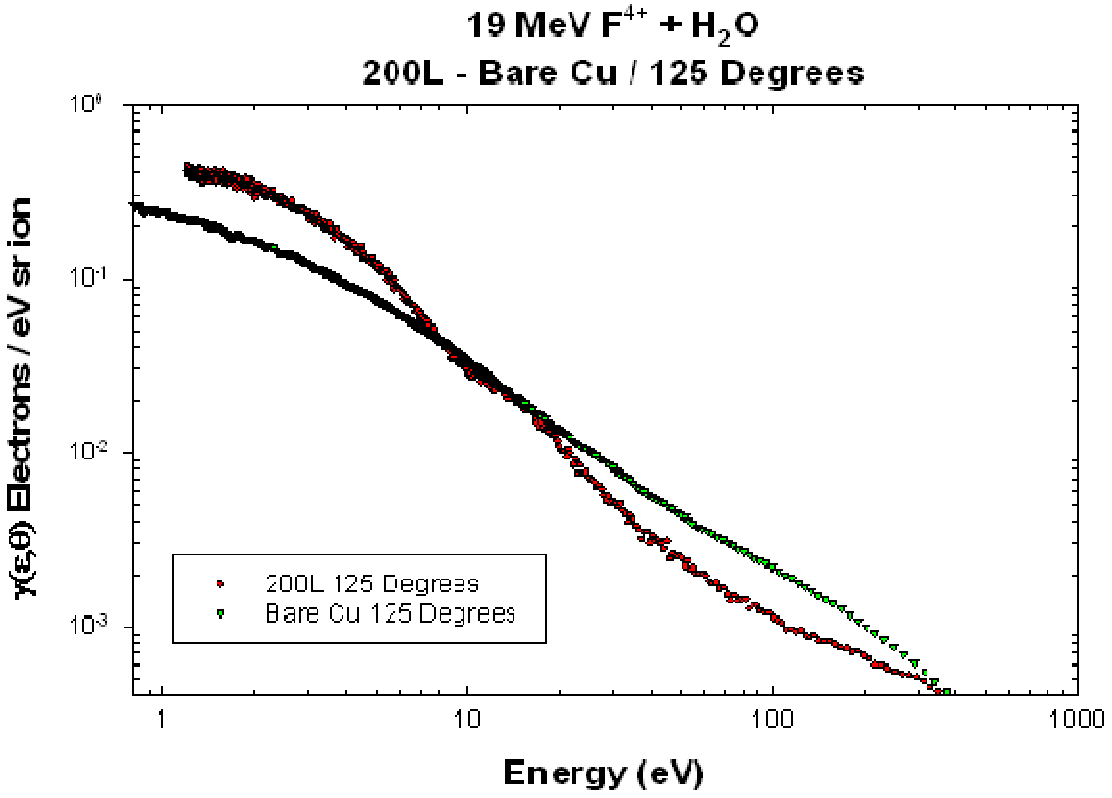

Figure 4.30. Electron emission yields at 125º for 19 MeV F^{+4} on 200 L thick ASW target along with emission yield from bare Cu foil at 125º.

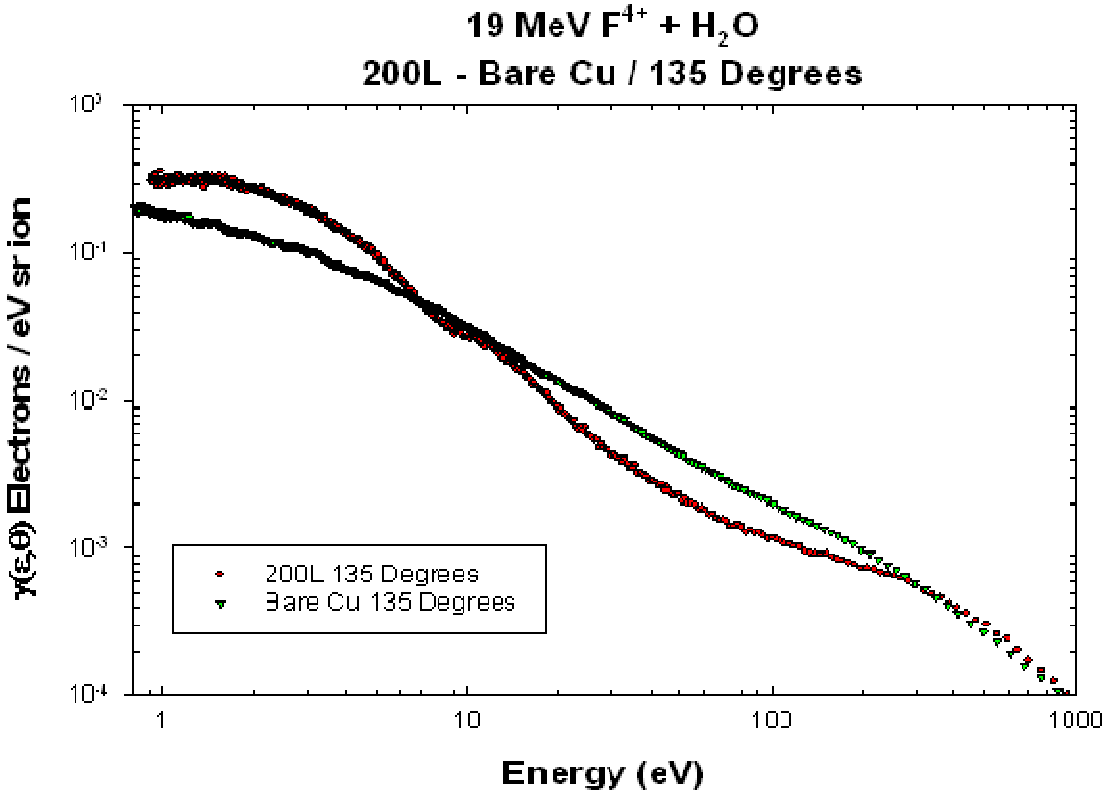

Figure 4.31. Electron emission yields at 135º for 19 MeV F^{+4} on 200 L thick ASW target along with emission yield from bare Cu foil at 135º.

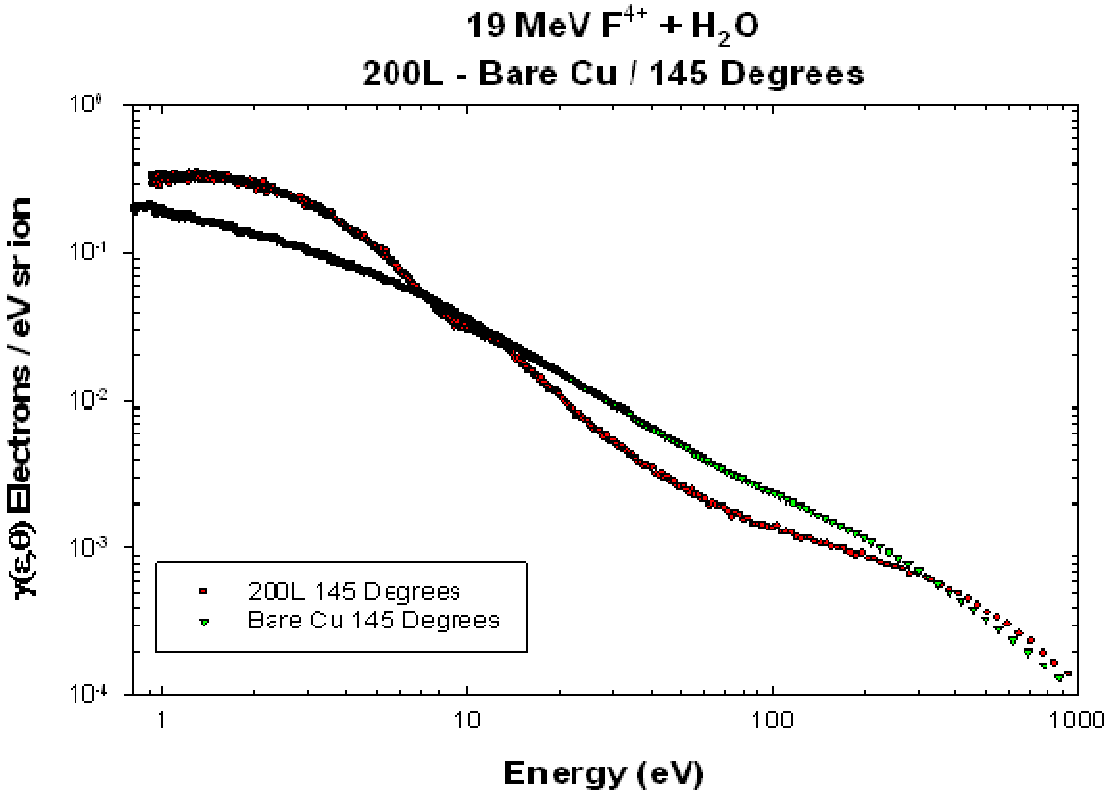

Figure 4.32. Electron emission yields at 145º for 19 MeV F^{+4} on 200 L thick ASW target along with emission yield from bare Cu foil at 145º.

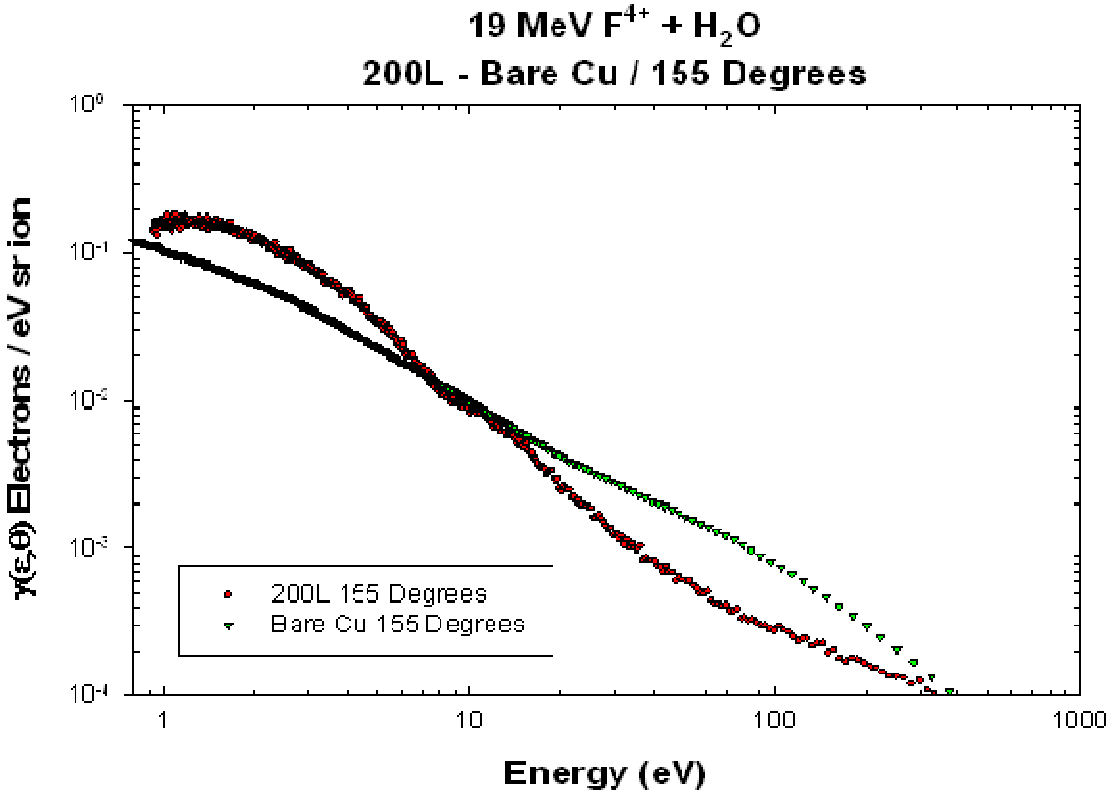

Figure 4.33. Electron emission yields at 155º for 19 MeV F^{+4} on 200 L thick ASW target along with emission yield from bare Cu foil at 155º.

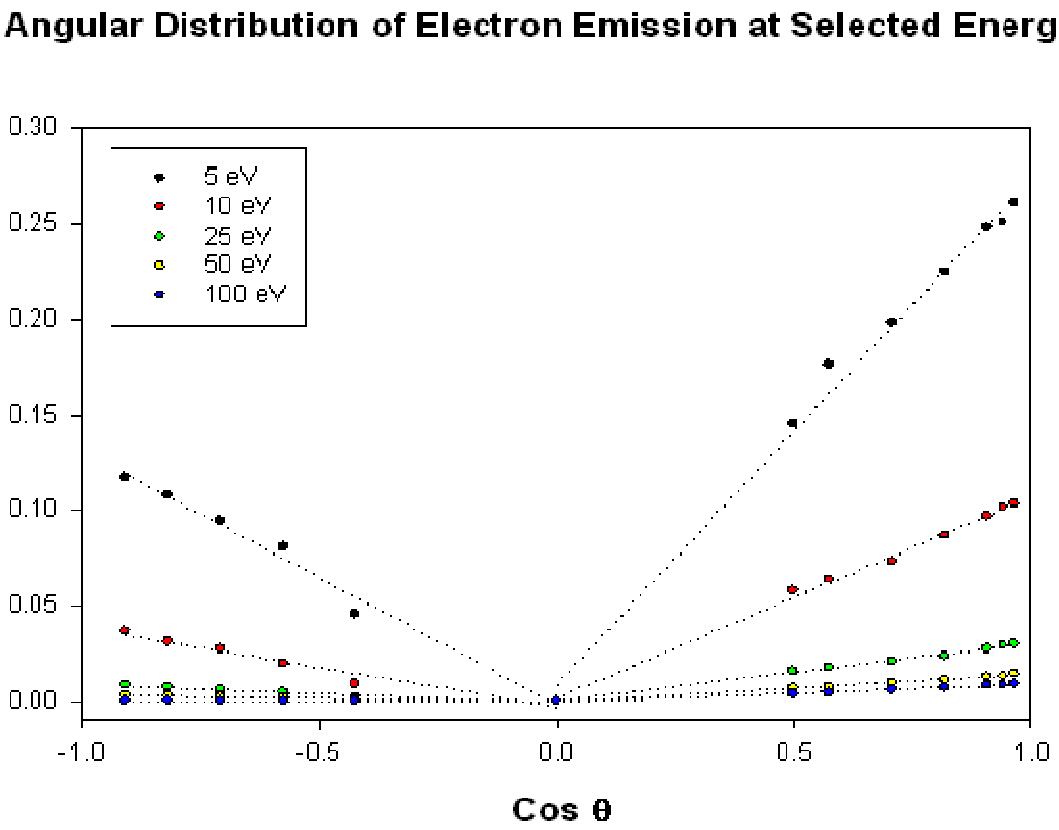

Figure 4.34. Angular differential electron emission yields for 19 MeV F^{+4} on 200 L thick ASW target plotted versus cosine of angle.

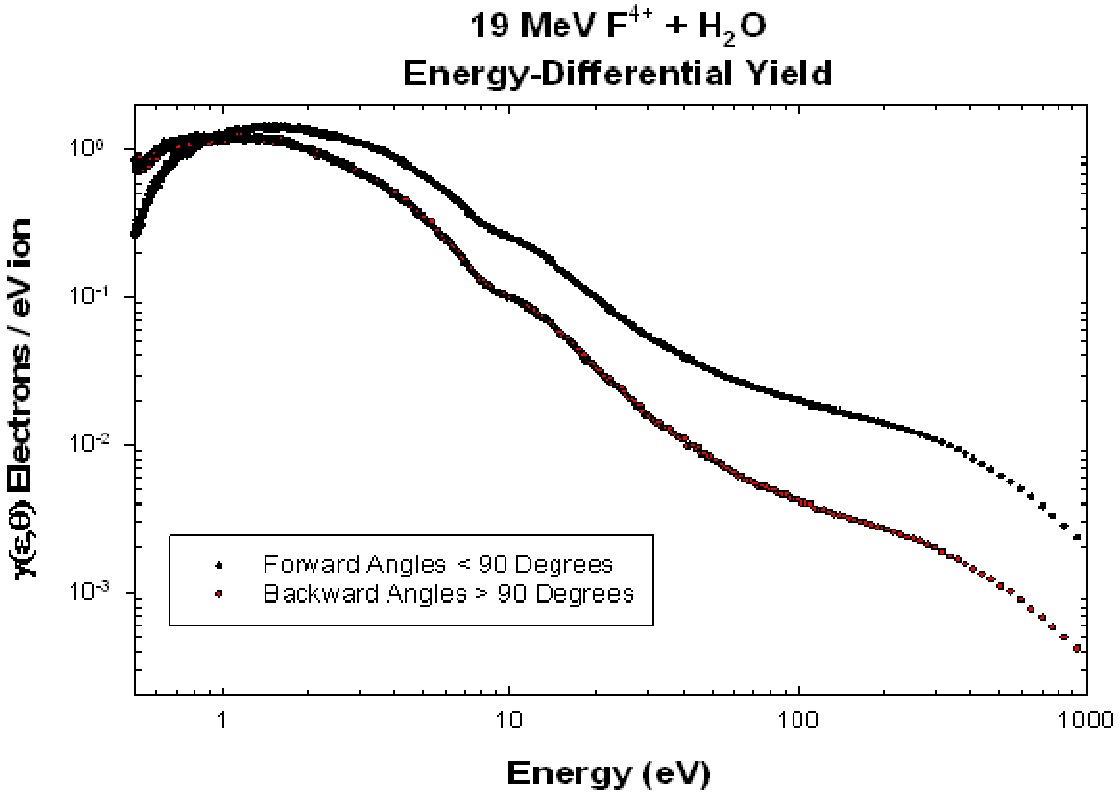

Figure 4.35. Single-differential electron emission yields for 19 MeV F^{+4} on 200 L thick ASW target integrated over angle for forward and backward angles.

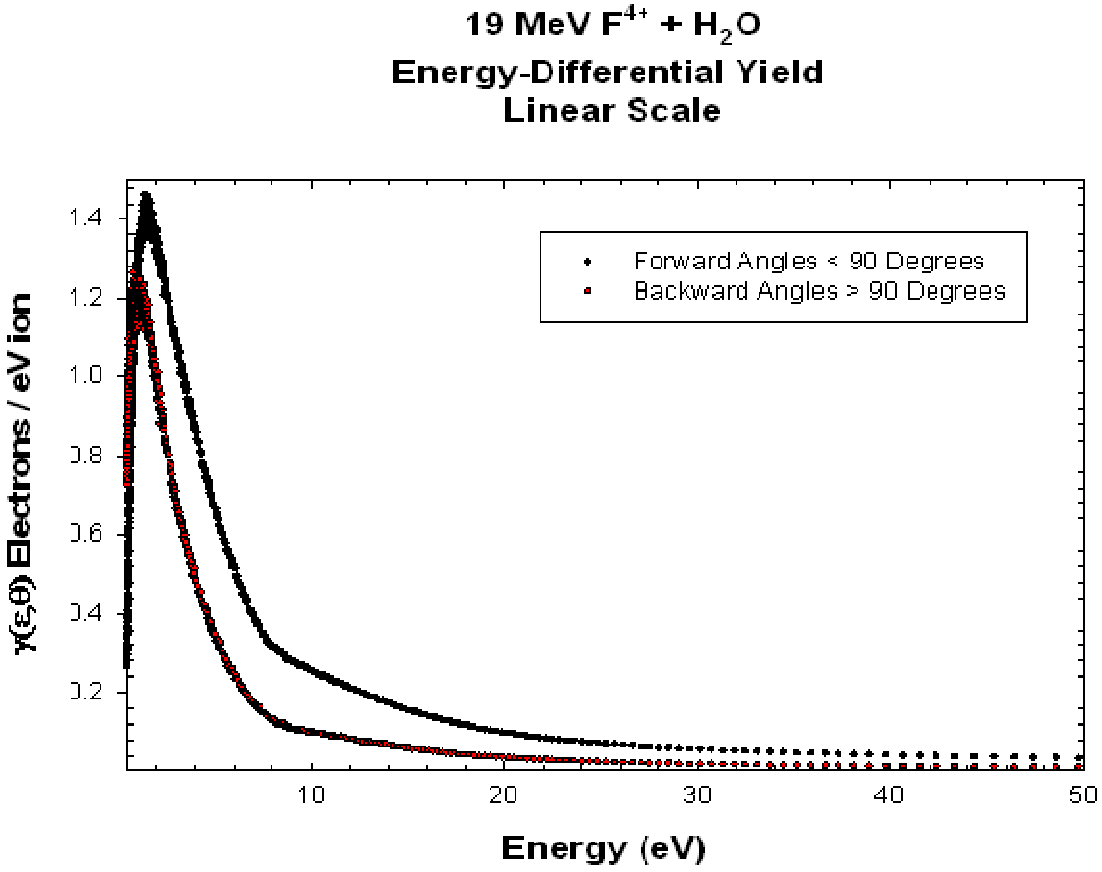

Figure 4.36. Single-differential electron emission yields for 19 MeV F^{+4} on 200 L thick ASW target integrated over angle for forward and backward angles plotted on linear scale.

Chapter 5: Summary

The aim of these experiments was to measure double-differential electron emission yields $\gamma(\varepsilon,\theta)$ from 19 MeV F^{4+} on thin copper foils and amorphous solid water targets. The measurements were intended to create a database from which benchmark comparisons with computational models can be made in the future. The measurements of the emission spectra from copper and amorphous solid water have been successfully performed.

Doubly differential electron emission yields as a result of 19 MeV F^{4+} and 6 MeV H^{+} projectiles incident on Cu foils were compared. The yield of electrons decreased as the emission angle increased, as measured normal to the surface of the target. This decrease followed the cosine relationship described in chapter 2. The position of the low-energy peak progressively shifted to higher energies with increasing emission angle. This also followed the expected trend described in chapter 2. Beyond the low-energy peak, the yield of electrons decreases rapidly as the electron energy increases. This results in a decrease of several orders of magnitude in the yield of electrons from approximately 1 eV to 1000 eV. This rapid decrease in the yield is also expected since the ionization cross section for the incident particle is lower for higher electron energies. The spectra for fluorine between 100 eV and 1000 eV were enhanced relative to protons by a higher probability for ionization and a broad region around 545 eV owing to convoy electrons.

Single-differential and total electron emission yields were determined from the doubly differential electron emission yields. In this case the angular dependent data were nearly linear when plotted against the cosine of the angle and the single-differential yields were as expected. The total yield was found to be $\gamma = 34 \pm 3$.

Spectra from 19 MeV F^{4+} incident on ASW targets of various thicknesses were presented. These spectra exhibited several effects with increasing ASW thickness. First, as ASW thickness increases the low-energy peak shifts to higher emission energies. This is from about 1 eV to 1.7 eV in the forward direction from 50 L to 800 L thicknesses, and from about 0.8 eV to 1.2 eV in the backward direction from 50 L to 600 L. Second, as ASW thickness increases the cutoff energy increases. In the forward direction the cutoff energy shifts from approximately 0.8 eV to 1.2 eV between 50 L and 800L, and in the backward direction from approximately 0.7 eV to 1.0 eV between 50L and 600L. Third, as the ASW thickness increase the electron emission yield increases. In the forward direction the low energy yield (<10eV) increases by 75% between 50L and 800 L, and in the backward direction low energy yields increase by about 50% between 50L and 600 L. Finally, as ASW thickness increases charging effects become more pronounced. This effect is worst in the backwards direction where the charging peak is enhanced by 300% between 50 L and 600 L.

Double-differential electron emission spectra from both 19 MeV F^{4+} and 6 MeV H^{+} projectiles on amorphous solid water were presented and compared. These spectra

followed the same trends as the bare foil spectra. The yields from 19 MeV F^{4+} were about an order of magnitude larger than for protons. The yields of both data sets were dominated by the low energy peak. Like the copper foil data the 19 MeV F^{4+} exhibited enhancement from 100 eV to 1000 eV from a higher probability for ionization by a slow moving highly charged particle and convoy electrons. Both fluorine and proton data displayed the H_2O auto-ionization peak between 13 and 14 eV.

The energy and angular distributions of electrons from amorphous solid water also exhibit the expected trend. The angular distributions were nearly linear when plotted against the cosine of the angle with minor discrepancies related to charging effects. The single-differential yields were as expected, and the total yields were found to be $\gamma_f = 21 \pm 4$ electrons and $\gamma_b = 8 \pm 2$ electrons.

Future studies are planned to measure the electron emission spectra from thin tissue sections. These targets are a logical extension of the data from amorphous solid water to more biologically relevant materials. The emission spectra from thin tissue sections are expected to be similar to those from amorphous solid water or those of the hydrocarbons measured by R.A McLawhorn [19]. Differences in the position of the low-energy peak from that of amorphous solid water are expected since the surface conditions greatly influence the emission spectra. Structures seen in the emission spectra, such as the auto-ionization peak seen at 13 eV, might also be seen. Measurements of the electron

emission spectra from tissue would be extremely useful in understanding the production and transport of electrons in biological materials.

References

1. H. Nikjoo, P. O'Neill, D.T. Goodhead and M. Terrissol, Computational modeling of low-energy electron-induced DNA damage by early physical and chemical events, I. Radiat. Biol. **71**: 467-483 (1997).
2. S.M. Pimblott, J.A. LaVerne, and A. Mozumder, Monte Carlo simulation of range and energy deposition by electrons in gaseous and liquid water, J. Phys. Chem. **100**: 8595-8606 (1996).
3. V. Cobut, Y. Frongillo, J.P. Patau, T. Goulet, M.-J. Fraser, and J.-P. Jay-Gerin, Monte Carlo simulation of fast electron and proton tracks in liquid water – I. Physical and Physicochemical aspects, Radiat. Phys. Chem. **51**: 229-243 (1998)
4. Y. Frongillo, T. Goulet, M.-J. Fraser, V. Cobut, J.P. Patau, and J.-P. Jay-Gerin, Monte Carlo simulation of fast electron and proton tracks in liquid water – II. Non-homogeneous chemistry, Radiat. Phys. Chem. **51**: 245-254 (1998).
5. W.E. Wilson and H. Nikjoo, A Monte Carlo code for positive ion track simulation, Radiat. Environ. Biophys. **38**: 97-104(1999).
6. D. Emfietzoglou, G. Papamichael, and M. Moscovitch, An event-by-event computer simulation of interactions of energetic charged particles and all their secondary electrons in water, J. Phys. D. Appl. Phys. 33, 932-944 (2000).
7. D. Emfietzoglou, G. Papamichael, K. Kostarelos, and M. Moscovitch, A Monte Carlo track structure code for electrons (~10eV-10keV) and protons (0.3-10MeV in water: partitioning of energy and collision events, Phys. Med. Biol. **45**: 3171-3194 (2000).
8. S. Uehara, L.H. Toburen, and H. Nikjoo, Development of a Monte Carlo track structure code fore low-energy protons in water, Int. J. Radiat. Biol. 77, 139-154 (2001).
9. H. Nikjoo, S. Uehara, D. Emfietzoglou, and F.A. Cucinotta, Track-structure codes in radiation research, Radiation Measurements **41** 1052 – 1074 (2006).
10. M. Dingfelder, R.H. Ritchie, J.E. Turner, W. Friedland, H.G. Paretzke, and R.N. Hamm, Comparisons of calculations with PARTRAC and NOREC: transport of electrons in liquid water, Radiat. Res. **169**: 584-594 (2008).
11. A. Travia and M. Dingfelder, Simulation of secondary electron emission spectra from thin metal foils after proton impact. J. Phys.: Conf. Ser. 194 (2009) 132025
12. J. A. Travia and M. Dingfelder, Simulation of secondary electron yields from thin metal foils after proton impact. Radiat. Prot. Dosim. 143 (2011) 139-144; doi: 10.1093 / rpd / ncq472

13. C.G. Drexler and R.D. DuBois, Energy- and angle-differential yields of electron emission from thin carbon foils after fast proton impact, Phys. Rev. A **53**, 1630-1637 (1996).

14. M. Dingfelder, D. Hantke, M. Inokuti, and H.G. Paretzke, Electron inelastic-scattering cross sections in liquid water, Radiat. Phys. Chem. **53**, 1-18, (1998).

15. M. Dingfelder, M. Inokuti, and H.G. Paretzke, Inelastic-collision cross sections of liquid water for interactions of energetic protons, Radiat. Phys. and Chem. **59**, 255-275 (2000).

16. F. Salvat, Optical model potential for electron and positron scattering by atoms. Phys Rev A **68**, 012708 (2003).

17. See for example, S.T. Manson, L.H. Toburen, D.H. Madison and N Stolterfoht, Energy and angular distributions of electrons ejected by fast protons and electrons, Phys. Rev. A **12, 60-79** (1975); L.H. Toburen, Atomic and molecular physics in the gas phase, In *Physical and Chemical Mechanisms in Molecular Radiation Biology* (Wa Glass and M.N. Varma, Eds.)pp. 51-97. Olenum Press, New York, 1991 C.G. Drexler, R.D. DuBois, H.G. Paretzke, and K.-O. Groeneveld Electron emission from condensed phase organic materials, Abstract: In *Congress Proceedings, Radiation Research 1895-1995* (Hagen U, Jung H, and Streffer C. Eds.) Tenth International Congress of Radiation Research, Würzberg, Germany. (1995). Pp 110.

18. C.G. Drexler, R.D. DuBois, H.G. Paretzke, and K.-O. Groeneveld Electron emission from condensed phase organic materials, Abstract: In *Congress Proceedings, Radiation Research 1895-1995* (Hagen U, Jung H, and Streffer C. Eds.) Tenth International Congress of Radiation Research, Würzberg, Germany. (1995). Pp 110.

19. R.A McLawhorn, *Electron Emission from Condensed-Phase Targets Induced by Fast Protons*, PhD Dissertation, Department of Physics, East Carolina University, Greenville, NC (2008).

20. R.D. DuBois and C.G. Drexler, Differential Electron Emission from solids and frozen gases. In *Proceeding of the 17th Werner Brandt Workshop on the Penetration of Charged Particles in Matter* (R Baragiola, ed.) Univesity of Virginia, Charlottesville, VA (1997). Pp95-104.

21. K.P. Stevenson, G.A. Kimmel, Z. Dohnálek, R.S. Smith, and B.D. Kay, Controlling the Morphology of Amorphous Solid Water, Science **283**, 1505 (1999).

22. C.I. Christou, *Electron emission from condensed targets by 2 MeV proton impact*, PhD Dissertation, Department of Physics, East Carolina University, Greenville NC (2004).

23. M. Dingfelder, A. Travia, R.A McLawhorn, J.L. Shinpaugh, and L.H. Toburen, Electron emission from foils and biological materials after proton impact, Radiat. Phys. Chem. **77**, 1213-1217 (2008).

24. S. L. McLawhorn, R. A. McLawhorn, K. D. Carnes, P. Richard, M. Dingfelder, L. H. Toburen, and J. L. Shinpaugh, Doubly differential electron yields from thin copper foils induced by fast ion impact, In Application of Accelerators in Research and Industry: Proceedings of the Twentieth International Conference (F.D. McDaniel and B.L. Doyle, Eds.), pp. 176-179, American Institute of Physics Conference Proceedings **1099**, AIP Press, New York 2009.

25. G.A. Kimmel, K.P. Stevenson, Z. Dohnálek, R.S. Smith, and B.D. Kay, Control of amorphous solid water morphology using molecular beams. I. Experimental results, J. Chem. Phys. **114**, 5284-5294 (2001)

26. ICRU55, *Secondary electron spectra from charged particle interactions*, Report 55, International Commission on Radiation Units and Measurements, Bethesda, MD, 1995.

27. D. Hasselkamp, H. Rothard, K. O Groeneveld, J. Kemmler, P. Varga, and H. Winter. Particle Induced Electron Emission II, edited by G. Hohler (Springer-Verlag, Berlin, 1992).

28. J. Schou, Secondary electron emission from solids by electron and proton bombardment. *Scanning Microscopy* **2**, 607-632 (1988).

29. H. Rothard, K. Kroneberger, M. Schosnig, P. Lorenzen, E. Veje, N. Keller, R. mailer, J. Kemmler, C. Biedermann, A. Albert, O. Heil, and K. O. Groeneveld, Secondary-electron velocity spectra and angular distributions from ions penetrating solids. *Nucl. Instr. and Meth. B* **48**, 616-620 (1990).

30. C. D. Denton, T. Jalowy, H. Luna, J. Fiol, D. Fregenal, S. Suarez, G. Bernardi, A. Gonzalez, N. R. Arista, and K. O. Groeneveld, Minimum in the distribution of electrons emitted from solids in the backward direction. *Nucl. Instr. and Meth. B* **164/165**, 927-932 (2000).

31. H. J. Frischkorn, K. O. Groenveld, D. Hofmann, P. Koschar, R. Latz, and J. Schader, Ion induced electron ejection from solids. *Nucl. Instrum. Methods* **214**, 123-128 (1983).

32. R. A. Baragiola, E. V. Alonso, J. Ferron, and A. Oliva-Florio, Ion-induced electron emission from clean metals. *Surf. Sci.* **90**, 240-255 (1979).

33. R. A. Baragiola, E. V. Alonso, and A. Olivia Florio, Electron emission from clean metal surfaces induced by low-energy light ions. *Phys. Rev. B* **19**, 121-129 (1979).

34. D. Hasselkamp, S. Hippler, and S. Scharmann, Ion-induced electron spectra from clean metal surfaces. *Nucl. Instr. and Meth. B* **18**, 561-565 (1987).

35. J. Ferron, E. V. Alonso, R. A. Baragiola, and A. Oliva-Florio, Ion-electron emission: The effect of oxidation. *Surf. Sci.* **120**, 427-434 (1982).

36. O. Benka, J. Purstinger, and A. Koyama, Kinetic electron emission from Al, Cu, and Au surfaces exposed to oxygen. *Phys. Rev. A* **58**, 2978-2984 (1998).

37. W. Soszka and J. Lipiec, The energy distribution of secondary ion-electron emission. *Surf. Sci.* **36**, 714-724 (1972).

38. W. Soszka, Studies of the bombarded surface of solids by methods of secondary ion-electron emission. *Surf. Sci.* **36**, 48-52 (1973).

39. D. Hasselkamp and A. Scharmann, Molecular effects in ion-induced secondary electron spectra. *Phys. Lett.* **96A**, 259-260 (1983).

40. D. Hasselkamp, S. Hippler, and A. Scharmann, Molecular effects in the energy spectra of ion-induced secondary electrons from gold. *Nucl. Instr. and Meth. B* **2**, 475-478 (1984).

41. W. Soszka, Ion-induced electron emission from cold metal targets covered by rare gases. *Nucl. Instr. and Meth. B* **48**, 630-634 (1990).

42. O. Benka, M. Pfaffenlehner, and A. Schinner, Electron emission yield of Al, Cu and Au targets induced by fast hydrogen and helium ions. *Nucl. Instr. and Meth. B* **117**, 350-356 (1996).

43. E. F. Da Silveira and J. M. F Jeronymo, Secondary electron emission from the entrance and exit surfaces of thin aluminum foils under fast light ion bombardment. *Nucl. Instr. and Meth. B* **24/25**, 534-537 (1987).

44. W. Meckbach, G. Braunstein, and N. Arista, Secondary-electron emission in the backward and forward directions from thin carbon foils traversed by 25-250 keV proton beams. *J. Phys. B* **8**, 344-349 (1975).

45. A. Clouvas, C. Potiriadis, H. Rothard, D. Hofmann, R. Wunsch, K. O Groeneveld, A. Katsanos, and A. C. Xenoulis, Role of projectile electrons in secondary electron emission from solid surfaces under fast-ion bombardment. *Phys. Rev. B* **55**, 12086-12098 (1997).

46. O. Benka, A. Schinner, T. Fink, and M. Pfaffenlehner, Electron-emission yield of Al, Cu, and Au for the impact of swift bare light ions. *Phys. Rev. A* **52**, 3959-3965 (1995).

47. D. Hasselkamp, K. G. Lang, A. Scharmann, and N. Stiller, Ion induced electron emission from metal surfaces. *Nucl. Instrum. Methods* **180**, 349-356 (1981).

48. O. Benka, E. Steinbauer, and P. Bauer, Kinetic electron emission yield induced by H^+ and He^{2+} ions versus stopping power for Al, Cu, Ag and Au. *Nucl. Instr. and Meth. B* **90**, 64-66 (1994).

49. H. Rothard, K. Kroneberger, A. Clouvas, E. Veje, P. Lorenzen, N. Keller, J. Kemmler, W. Meckbach, and K. O. Groeneveld, Secondary-electron yields from foils: A possible probe for the electronic stopping power of heavy ions. *Phys. Rev. A* **41**, 2521-2535 (1990).

50. Y. Sato, A. Higashi, D. Ohsawa, Y. Fujita, Y. Hashimoto, and S. Muto, Projectile charge dependence of electron emission from foils. *Phys. Rev. A* **61**, 052901 (2000).

51. R. Middleton, A versatile high intensity negative ion source. *Nucl. Instrum. Methods Phys. Res.* **220**, 105-106 (1984).

52. E.D. Wells, *Charge Transfer in very slow H^+ + $D(1_s)$ half collisions*, PhD Dissertation. Manhattan, KS. Kansas State University, (2000).

53. R.J. Van de Graaff, Tandem electrostatic accelerators. *Nucl. Instrum. And Methods*, **8**, 195-202 (1960).

54. R.I. Masel. Principles of Adsorption and Reaction on Solid Surfaces, (Wiley, New York, 1996), p.378.

55. P.H. Poole, U. Essmann, F. Sciortino, and H.E. Stanley. Phase diagram for amorphous solid water. *Phys. Rev.* E **48**, 4605-4610 (1993).

56. L. H. Toburen and W. E. Wilson, *Rev. Sci. Instrum.* **46**, 851 (1975).

57. L. Wiza, Microchannel plate detectors. *Nucl. Instr. And Meth.* **162**, 587-601 (1979).

58. A. Koyama, T. Takashi, and H. Sakair, *Jpn. J. Appl. Phys.* **20**, 65-70 (1981).

59. N.V. Neelavathi, R.H. Richie and W. Brandt, Bound electron states in the wake of swift ions in solids. *Phys. Rev. Lett.* **33**, 302-305 (1974).

60. L.H. Toburen, R.D. DuBois, C.O. Reinhold, D.R. Schultz and R.E. Olson, Experimental and theoretical study of the electron spectra in 66.7-350keV/u C^+ + He collisions. *Phys. Rev. A* **42**, 5338-5347 (1990).

61. L.H. Toburen, R.A. McLawhorn, S.L. McLawhorn. K.D. Carnes, M. Dingfelder, A. Travia, and J.L. Shinpaugh, Electron transport in condensed phase material, Radiat. Prot. Dosim. 143 (2011) 135-138; doi: 10.1093 / rpd / ncq529.

62. R.A. McLawhorn, S.L. McLawhorn, K.D. Carnes, M. Dingfelder, L.H. Toburen, J.L. Shinpaugh, Electron emission from amorphous solid water induced by fast ions. J. Phys.: Conf. Ser. 194 (2009) 132039

63. L.H. Toburen, S.L. McLawhorn, R.A. McLawhorn, K.D. Carnes, M. Dingfelder, and J.L. Shinpaugh, Electron emission from amorphous solid water induced by the passage of energetic protons and fluorine ions. Radiat. Res. 174 (2010) 107-118.